

UNIVERSIDADE DE LISBOA
INSTITUTO SUPERIOR TÉCNICO

Ultrastructure, mechanical behaviour and pre-therapeutic X-ray tomography of sialoliths: towards a deeper understanding of the response to lithotripsy

Pedro de Almeida Nolasco

Supervisor: Doctor Patrícia Maria Cristovam Cipriano Almeida de Carvalho

Co-Supervisor: Doctor Raul Carneiro Martins

Thesis approved in public session to obtain the PhD degree in
Biomedical Engineering

Jury final classification: Pass with distinction

UNIVERSIDADE DE LISBOA
INSTITUTO SUPERIOR TÉCNICO

Ultrastructure, mechanical behaviour and pre-therapeutic X-ray tomography of sialoliths: towards a deeper understanding of the response to lithotripsy

Pedro de Almeida Nolasco

Supervisor: Doctor Patrícia Maria Cristovam Cipriano Almeida de Carvalho
Co-Supervisor: Doctor Raul Carneiro Martins

Thesis approved in public session to obtain the PhD degree in
Biomedical Engineering

Jury final classification: Pass with distinction

Jury

Chairperson: Doctor João Pedro Estrela Rodrigues Conde, Instituto Superior Técnico da Universidade de Lisboa

Members of the Committee:

Doctor Jorge Galvão Martins Leitão, Faculdade de Medicina Dentária da Universidade de Lisboa
Doctor Albano Augusto Cavaleiro Rodrigues de Carvalho, Faculdade de Ciências e Tecnologia da Universidade de Coimbra
Doctor Rogério Anacleto Cordeiro Colaço, Instituto Superior Técnico da Universidade de Lisboa
Doctor João Paulo Miranda Ribeiro Borges, Faculdade de Ciências e Tecnologia da Universidade Nova de Lisboa
Doctor Patrícia Maria Cristovam Cipriano Almeida de Carvalho, Instituto Superior Técnico da Universidade de Lisboa
Doctor Manuel Francisco Costa Pereira, Instituto Superior Técnico da Universidade de Lisboa

Funding institutions: Fundação para a Ciência e Tecnologia (PTDC/SAU-ENB/111941/2009)

Resumo

Os métodos de litotripsia apresentam menor eficiência na fragmentação de cálculos salivares (sialólitos) em comparação com as taxas de sucesso conseguidas em cálculos renais. A tenacidade à fractura dos sialólitos não é bem compreendida, existindo pouca informação sobre a sua ultraestrutura e a sua composição, bem como sobre a influência destas características intrínsecas na resposta à litotripsia.

Os sialólitos apresentam, tipicamente, um núcleo principal rodeado por regiões de crescimento concêntrico ou irregular compostas, a menor escala, por estruturas lamelares e/ou globulares com grau de mineralização variável. O estudo destas configurações por microscopia electrónica revelou que as estruturas lamelares resultam de um fenómeno quasi-periódico de precipitação mineral (precipitação de Liesegang-Ostwald), enquanto as estruturas globulares têm origem num efeito de tensão superficial entre dois fluidos orgânicos imiscíveis.

Análise por espectroscopia de infravermelho demonstrou que a matéria orgânica presente nos sialólitos corresponde essencialmente a saliva desidratada. Por outro lado, a difracção de raios-X mostrou que a matéria mineral consiste numa mistura de hidroxiapatite deficiente em cálcio (89 % vol.) e whitlockite (11 % vol.). A densidade média da matéria mineral é de 2,8 g/cm³ e, em condições hidratadas, a matéria orgânica, com uma densidade de 1,2 g/cm³, ocupa cerca de 65 % do volume dos sialólitos. A relação entre a densidade mineral dos sialólitos e a atenuação de raios-X foi determinada por microtomografia computadorizada, em condições *ex vivo*, e validada para tomografia computadorizada helicoidal em condições *in vivo*.

Indentação mecânica a escalas nano e micrométricas permitiu estabelecer uma relação entre ultraestrutura/composição e propriedades mecânicas locais, usada para justificar o comportamento mecânico das estruturas compósitas de matéria orgânica/mineralizada à escala macro. O estudo dos efeitos induzidos por litotripsia mecânica mostrou que as reverberações transmitidas por sondas ultra-sónicas ou pneumobalísticas afectaram preferencialmente as regiões mineralizadas, não danificando as zonas orgânicas circundantes. Em contraste, as ondas de choque lixiviaram os componentes orgânicos, causando erosão de toda a estrutura. Ablação por laser de Ho:YAG destruiu homogeneamente as zonas irradiadas, porém, não se observou propagação de fissuras ou outro tipo de dano, sendo o seu efeito localizado.

Em suma, a estrutura e a composição dos sialolitos são factores determinantes no seu comportamento à fractura e a presença de matéria orgânica contribui para reduzir a eficiência dos métodos de litotripsia. O conhecimento das características destas calcificações em contexto pré-terapêutico é, portanto, essencial para uma optimização dos parâmetros de litotripsia.

Palavras-chave: Sialolitos, propriedades mecânicas, litotripsia, tomografia computadorizada.

Abstract

Lithotripsy methods show lower efficiency in the fragmentation of salivary calculi (sialoliths) compared to the success rates achieved with renal calculi. Their apparently tougher response is not fully understood, while limited information is available on the ultrastructure and composition of sialoliths and their role on lithotripsy efficiency.

Sialoliths show typically a major core surrounded by regions of concentric or irregular growth that consist of banded and globular structures with variable degree of mineralization. The mineralization of the banded structures is compatible with a quasi-periodic mineral precipitation process (Liesegang–Ostwald precipitation), whereas the globular structures arise from surface tension effects between two immiscible fluids.

Infrared spectra showed that the organic fraction was consisted of dehydrated saliva, whereas X-ray diffraction revealed that the mineral matter is composed of a mixture of calcium-deficient hydroxyapatite (89 % vol.) and whitlockite (11 % vol.), with an average density of 2.8 g/cm³. In hydrated conditions, the organic matter has a density of 1.2 g/cm³ and occupies most of the sialoliths' volume (~ 65 % vol.). The relation between sialoliths mineral density and X-ray attenuation was established by *ex vivo* computed microtomography and validated for *in vivo* helical computed tomography.

A clear correlation between the local mechanical properties and ultrastructure/chemistry was established by mechanical indentation tests at nano and microscale. These results were used to understand the mechanical behaviour of the organic/mineral composite structure at macroscale. Ultrasonic and pneumoballistic reverberations damage preferentially highly mineralized regions, leaving relatively unaffected the surrounding organic matter. In contrast, shock waves leach the organic component and lead to erosion of the overall structure. Laser ablation destroys homogeneously the irradiated zones, although the damage is less extensive than with mechanical methods.

Overall, the present results show that the composition and internal morphology are key features behind sialoliths' comminution behaviour and that the presence of organic matter reduces the therapeutic efficiency of lithotripsy methods.

Key words: Sialolith, mechanical properties, lithotripsy methods, computed tomography.

Agradecimentos

Não teria sido possível a realização desta dissertação sem a ajuda de várias pessoas a quem gostaria de agradecer:

À minha orientadora a Doutora Patrícia Carvalho, por todo o apoio pessoal e científico, inesgotável paciência, dedicação e disponibilidade

Ao meu co-orientador o Doutor Raul Carneiro Martins, ao Doutor António Alves de Matos e ao Doutor Manuel Francisco Costa Pereira pela ajuda e sugestões durante todo este trabalho

Ao Doutor António Maurício do Departamento de Engenharia Civil Arquitectura e Georrecursos do Instituto Superior Técnico, pelo acompanhamento e ajuda durante as aquisições por micrografia computacional de raio-X

À Doutora Daniela Nunes e à Engenheira Isabel Nogueira pela disponibilidade e ajuda a operar microscópio electrónico de varrimento e o microscópio electrónico de transmissão

Ao Doutor Manuel Evaristo do Departamento de Engenharia Mecânica da Universidade de Coimbra, pela sua ajuda nos ensaios mecânicos

À Engenheira Carla Rocha do Departamento de Engenharia Civil Arquitectura e Georrecursos do Instituto Superior Técnico, pelo acompanhamento e ajuda durante os ensaios de espectroscopia de infravermelho e difracção de raio-X

Ao Departamento de Anatomia Patológica do Hospital Curry Cabral, pela ajuda na preparação das amostras observadas por microscopia electrónica de transmissão

Ao Técnico Nuno Vital do departamento de Radiologia do Hospital de São José pela ajuda prestada nas aquisições *ex vivo* por tomografia computadorizada helicoidal

À Enfermeira Filomena Caeiro do Bloco Operatório do Hospital de São José, pela ajuda prestada nos ensaios com as técnicas de litotripsia

À Fundação para a Ciência e Tecnologia pelo apoio financeiro (Projecto PTDC/SAU-ENB/111941/2009).

Acknowledgements

It would not have been possible to produce this thesis without the help of several people who I would like to thank:

My supervisor Doctor Patrícia Carvalho for her personal and scientific support, endless patience, dedication and availability

My co-supervisor Doctor Raul Carneiro Martins, Doctor António Alves de Matos and Doctor Manuel Francisco Costa Pereira, for their help and suggestions throughout this work

Doctor António Maurício from the Department of Civil Engineering Architecture and Geologic Resources from Instituto Superior Técnico, for his help during the X-ray computed microtomography acquisitions

Doctor Daniela Nunes and Engineer Isabel Nogueira, for their help with the scanning electron microscope and the transmission electron microscope operation

Doctor Manuel Evaristo from the Department of Mechanical Engineering from University of Coimbra, for his help with the mechanical characterization experiments

Engineer Carla Rocha from the Department of Civil Engineering architecture and Geologic Resources from Instituto Superior Técnico, for her help and support during the Fourier transform infrared spectroscopy and X-ray diffraction experiments

The Anatomic Pathology Department of Curry Cabral Hospital, for their help in sample preparation for the transmission electron microscope

Technician Nuno Vital from the Department of Radiology of Hospital de São José, for his help with the *ex vivo* helical computed tomography acquisitions

Nurse Filomena Caeiro from the Operatory block of Hospital de São José, for her help with the lithotripsy experiments

The Foundation for Science and Technology for the financial support (grant PTDC/SAU-ENB/111941/2009).

Table of contents

Chapter 1. Introduction	1
1.1. Motivation.....	3
1.2. State of the art	3
1.2.1. Sialolithiasis.....	3
1.2.2. Diagnosis.....	5
1.2.3. Therapeutic approaches	6
1.3. Work summary.....	12
1.4. References.....	13
Chapter 2. Experimental	21
2.1. Materials and methods	23
2.1.1. Samples	23
2.1.2. Petrographic sample preparation.....	23
2.1.3. TEM sample preparation.....	24
2.1.2 Microscopy observations.....	25
2.1.3 Chemical characterization	26
2.1.4 Computed microtomography.....	26
2.1.5 Helical computed tomography	29
2.1.6 Mechanical characterization.....	30
2.1.7 Lithotripsy experiments.....	31

2.2	References.....	32
Chapter 3. Chapter 3. Sialoliths ultrastructure.....		35
3.1.	Results.....	37
3.1.1.	General configuration	37
3.1.2.	Local structure	40
3.2.	Discussion	49
3.3.	Summary	53
3.4.	References.....	54
Chapter 4. X-ray computed tomography of sialoliths.....		57
4.1.	Results.....	59
4.1.1.	Chemical and structural characterization.....	59
4.1.2.	Ultrastructure	66
4.1.3.	Computed microtomography	67
4.1.4.	Helical computed tomography	71
4.2.	Discussion	73
4.3.	Summary	77
4.4.	References.....	78
Chapter 5. Local response of sialoliths to lithotripsy		83
5.1.	Results.....	85
5.1.1.	Local and average mechanical behaviour	85
5.1.2.	Local and extended damage patterns	91

5.2. Discussion	97
5.2.1. Local and average mechanical behaviour	97
5.2.2. Local and extended damage	99
5.3. Summary	102
5.4. References	104
Chapter 6. Concluding remarks and future work	107

Figure index

Figure 1.1 - Lithotripsy working principles. Adapted from [63].....	7
Figure 1.2 - Interaction of mechanical waves with the calculus structure. Adapted from [77] and [69].....	10
Figure 1.3 – In laser ablation photothermal effects are responsible for central melting while photomechanical interactions affect mostly the surrounding regions. Adapted from [83].....	11
Figure 2.1. Part of the sialolith was embedded in epoxy resin (a) and subsequently ground and polished for scanning electron microscopy observation and mechanical testing (b), whereas the non-embedded part (c) was subsequently prepared for spectroscopy experiments.....	24
Figure 2.2 – Schematic representation of the method used to determine the warped coordinates of each voxel in the μ CT datasets. The goal was to conform the external shape of the sialolith to a sphere in order to obtain radial profiles reflecting the internal convolutions.....	29
Figure 3.1 - Median longitudinal cross-sections of submandibular (S_n) and parotid (P_n) sialoliths obtained from μ CT data. Brighter regions represent higher mineralization and dark regions represent essentially organic matter. Horizontal attenuation profiles crossing the specimens' core are shown for S_{12} and S_{25} . The vertical dashed lines indicate the major axis, which in the case of quasi-equiaxed sialoliths has been established taking into account the internal structure. Scale bar is 2 mm.....	38

- Figure 3.2 - Array of SEM (backscattered electron (BSE)) images showing representative growth patterns: left, concentric; right, irregular; top, high mineralization; and bottom, low mineralization. The magnified details show the local features of each pattern. Scale bar is 1 mm.39
- Figure 3.3 – (a) TEM image of alternating mineralized/organic bands. The magnified detail reveals the difference in precipitate density. (b)–(d) SEM images (BSE) of banded structures threaded with organic globules of variable size and mineralization. (e) SEM (secondary electron (SE)) image of mineralized nodules in an internal void. (f) SEM (BSE) image of mineralized nodules in banded layers. (g) Convolved organic structures at the periphery of a sialolith.41
- Figure 3.4 – (a) SEM (BSE) image of a globular region in a submandibular sialolith with corresponding X-ray maps for (b) Ca, (c) S, (d) P, (e) C, and (f) O. Spectra resulting from point analyses of a heavily mineralized region ((g) from region 1 in (a)) and of an organic globule ((h) from region 2 in (a)) The two spectra have been normalized for a constant background level.42
- Figure 3.5 - SEM (BSE) images of organic globules dispersed in mineralized regions. (a) Organic matter with relatively low sulfur content in a submandibular sialolith. (b) Sulfur-rich globules in a parotid sialolith. The spectra have been normalized using the background level.43
- Figure 3.6 - TEM images and electron diffraction patterns of crystals. (a) Coexisting crystals of different structures: A, colonies of filamentary crystals; B, needlelike crystals; C, large single crystals. (b) Filamentary crystals. (c) Agglomerate of parallelepiped crystals. (d) Ring electron diffraction pattern obtained from a region of filamentary crystals showing the radial integrated intensity together with

a simulation for hydroxyapatite. (e) Microdiffraction pattern of a single crystal indexed for hydroxyapatite.44

Figure 3.7 – (a) TEM image of globular structures showing that the onset of mineralization/crystallization is associated with peripheral organic substances weakly stained by OsO_4 (arrows). (b) SEM (BSE) image of internal mineralization occurring through heterogeneous nucleation at the globule wall. (c) TEM image of filamentary crystals extending inward from the globule wall. (d) SEM (BSE) image of organic globules with internal mineralization through homogeneous nucleation. (e) TEM image of homogeneously nucleated particles displaying diffraction contrast. (f) TEM image of needlelike crystals extending from the mineralized periphery to the internal region of a globule.46

Figure 3.8 – (a)–(c) SEM (BSE) images at increasing magnifications of fingerlike globular structures with self-similarity. Arrow indicates same location. (d) TEM image showing globular structures with self-similarity. (e) SEM (SE) image showing extruded globules at a void. (f) SEM (BSE) image of mineralized extruded globules enclosed by an external mineralized layer (arrow).47

Figure 3.9 – (a), (d) BSE (SEM) images showing fingerlike globular structures. (b), (e) Binarized images where unwanted detail has been masked prior to fractal analysis. (c), (f) Results obtained for randomly generated $k = 1, \dots, 12$ positions of grids oriented as the image. The side length ε was defined as a fraction of the original image. One of the 12 regressions is shown for each image with the respective fractal dimension $D_f(k)$ and correlation coefficient r to attest for the self-similarity of the globular structures. The legends also show the mean fractal dimension and standard deviation (σ) of the 12 different positions $D_f(1, \dots, 12)$48

- Figure 3.10 – (a) Median section of S₃. (b) Bacterial colony found at the periphery of S₃. (c) Comparison of globular structures and bacterial colony. (d) Bacteria mineralized with filamentary crystals. (e) Bacteria mineralized with needlelike crystals. (f) Non-mineralized bacteria undergoing cell division.49
- Figure 4.1 - XRD patterns of prototypical sialoliths with simulated diffractograms for HA [3] and Whi [4]. The red arrows indicate major Whi peaks. HA and Whi volume fractions are indicated as a ratio above each experimental diffractogram.60
- Figure 4.2 – FTIR spectra of a sialolith, a large organic region in a sialolith, saliva and hydroxyapatite. Characteristic bands [6-10] are indicated.61
- Figure 4.3 - (a) Volume fraction of Whi in HA+Whi mixtures, as determined by XRD, as a function of Mg concentration in hydrated specimens. The line represents the expected Mg variation for stoichiometric HA+Whi mixtures. HA: $\text{Ca}_{10-x}(\text{PO}_4)_6-x(\text{CO}_3)_y(\text{HPO}_4)_{x-y}\text{OH}_{2-x}$, with $x = 2$ and $y = 0.72$ and Whi: $\text{Ca}_{18}\text{Mg}_2(\text{PO}_4)_{14}$. (b) P concentration vs Ca+Mg concentration with nominal positions for stoichiometric HA and Whi (open circles) and proportional guidelines. (c) Measured sialolith density vs mineral volume fraction estimated from the experimental Ca+Mg concentration (see (d)). The green region represents the 95 % confidence interval of the linear regression. (d) Mineral volume fraction (line and points) and mineral density (only line for clarity) estimated from the measured density and vs Ca+Mg concentration. Colour code for the solid points in all plots: blue – solely HA and blue/red – mixture of HA and Whi as inferred from XRD, gray – undetermined mineral HA vs Whi proportion. The lines in (a), (b) and (d) represent expected variations, while in (c) a rule of mixtures (equation in legend) was fitted to the blue/red points.65

- Figure 4.4 – Calcium phosphate clusters and typical hydroxyapatite crystals in sialolith ultrastructure. (a), (b) SEM (BSE) image of globules of organic matter partially mineralized. (c) TEM magnified view of interfacial region. (d) SEM (BSE) image of mineralization clusters inside a globule. (e) TEM image of hydroxyapatite crystals in a region around globules.....67
- Figure 4.5 – Median longitudinal μ CT cross-sections of a subset of specimens. Brighter regions indicate higher mineralization and dark regions represent essentially organic matter. Scale bar is 2 mm68
- Figure 4.6 – Radial attenuation profiles of sialoliths normalized to enamel's attenuation, obtained from warped and radially integrated μ CT data. The red dotted curve represents the average profile of the studied population. The arrow indicates a maximum at $R = 1.2 \times 10^{-3}$ m.68
- Figure 4.7 – (a) Attenuation as a function of density. (b) Attenuation as a function of mineral density. Blue – solely HA and blue/red – mixture of HA and Whi as inferred from XRD, gray – undetermined mineral proportion, open circles – literature values [26-28]. The error bars correspond to the standard deviation of the attenuation distribution in each specimen and the green region corresponds to the 95 % confidence interval of the linear regression.70
- Figure 4.8 – (a) Deviations of volume and attenuation between HTC and μ CT data as a function of specimen average radius. The ● and ★ data points correspond, respectively, to *ex vivo* and *in vivo* acquisitions performed using the Light Speed GE VCT instrument. (b) Deviation of HCT attenuation relative to the μ CT data as a function of the ratio between specimen radius and in-plane HCT resolution (0.19-0.76) and of the ratio between specimen radius and HCT collimation width (0.63).72

- Figure 4.9 - Comparison between μ CT and HCT sections of three specimens obtained *in vivo* and *ex vivo*: (a), (b), (d), (e), (f) Light Speed GE VCT, (c) Philips Brilliance 16 and (g), (h), (i) SkyScan 1172. Spatial resolution of (a) in plane: 0.56 mm and z-axis: 0.63 mm, (b) in-plane: 0.54 mm and z-axis: 0.63 mm. (c) in-plane: 0.28 mm and z-axis: 0.75 mm. (d) and (e) in-plane: 0.19 mm and z-axis: 0.19 mm. (f) in-plane: 0.51 mm and z-axis: 0.51 mm. (g) and (h) voxel size: 0.01 mm. (i) voxel size: 0.02 mm. Scale bar is 4 mm.....73
- Figure 5.1 – (a) to (c) SEM (BSE) images showing the sialolith typologies in terms of morphology and local mineralization with corresponding EDS spectra. Berkovich nanoindentations are marked: \bullet - accepted, \boxtimes - excluded. (d) to (f) Young’s modulus vs hardness distributions obtained from nanoindentations where the lines represent constant values of the fitted Gaussian models. In (f) the fitted model was a summation of two 2D Gaussians.....86
- Figure 5.2 - (a) SEM (BSE) image of a Vickers microindentation (1 N) performed on a dry sialolith. Microindentations in hydrated specimens could not be clearly discerned by SEM. (b) and (c) Young’s modulus vs hardness distributions obtained from, respectively, dry and hydrated sialoliths, where the lines represent constant values of the fitted 2D Gaussian models.88
- Figure 5.3 - Effect of loss of hydration water during microindentation experiments. Each set of experiments was carried out for about 2 h with a relative humidity of 70 %. The linear correlation factor with time (r) was 0.10 for E and 0.16 for H.....89
- Figure 5.4 - (a) Young’s modulus vs hardness where the domains enclose mean \pm standard deviation ($\mu \pm \sigma$). Data: [1, 2] for renal calculi, [3, 4, 5] for enamel, [6, 7] for hydroxyapatite, and present work for sialoliths. (b) Magnified detail for renal calculi with $\mu \pm \sigma$ values from literature. As standard deviations for E were not

reported, the domain encloses $\mu \pm \sigma$ for H but only μ for E and is represented by a dashed line. (c) Magnified detail for dry composite sialoliths for the 5 specimens tested. (d) Magnified detail for hydrated composite sialoliths for the 5 specimens tested.	90
Figure 5.5 - (a) Crack pattern resulting from microindentation. (b) Magnified detail of (a) showing debonding at globule interfaces, crack deflection, branching and meandering. (c) Dimple fracture surface exhibiting textbook features of a ductile material containing rigid inclusions	92
Figure 5.6 - (a) Damage caused by ultrasonic vibrations. (b) Magnified detail of (a) showing preferential extraction of mineralized matter (bright regions). (c) Damage caused by pneumoballistic impacts. (d) Magnified detail of (c) showing preferential removal of mineralized material.	93
Figure 5.7 - Damage caused by shock waves. (a) Damaged sialolith's rendered volume. (b) to (d) Structures resulting from preferential removal of organic matter. (e) Flow of highly mineralized matter.	94
Figure 5.8 - (a) Damage caused by the Ho:YAG laser. (b) Detail of the wall around the irradiated area evidencing melting. (c) Detail of the wall around the irradiated area showing globules.	95
Figure 5.9 - μ CT sagittal and axial sections showing extended damage resulting from (a) to (d) macroindentation, (e) and (f) pneumoballistic impacts, and (g) and (h) shock waves. Indentation data is given in the corresponding legends. The dashed line on the sagittal section indicates the position of the axial section.	96
Figure 5.10 - (a) Toughening mechanisms in a brittle matrix containing dispersions of ductile inclusions. (b) Classical dimple fracture in a ductile material containing rigid inclusions. Adapted from [22]	99

Table index

Table 4.1 – Average concentrations determined by AES for 40 sialoliths in hydrated and dry states.	62
Table 4.2 – Mineralized and organic fractions (in weight and volume) of 33 sialoliths in dry and hydrated states, calculated from Ca+Mg wt. %.....	66
Table 4.3 – Geometrical parameters obtained from μ CT data from 23 sialoliths.	69
Table 5.1 - Standardless quantification of the spectra shown in Figure 5.1.	87
Table 5.2 – Young’s modulus and hardness estimated from nano, micro and macroindentation.....	89

Acronyms

SEM	– Scanning electron microscopy
SE	– Secondary electron signal in SEM
BSE	– Backscattered electron signal in SEM
TEM	– Transmission electron microscopy
EDS	– Energy dispersive spectroscopy
XRD	– X-ray powder diffraction
FTIR	– Fourier transform infrared spectroscopy
ICP-AES	– Inductive coupled plasma atomic emission spectroscopy
μCT	– Cone-beam computed micro-tomography
CBCT	– Cone-beam computed tomography
HCT	– Helical computed tomography
HA	– Hydroxyapatite
Whi	– Whitlockite
ACP	– Amorphous calcium phosphates
ESWL	– External shock wave lithotripsy
Ho:YAG	– Holmium:Yttrium-aluminum-garnet (YAG)

Symbols

S_n	– Submandibular specimens
P_n	– Parotid specimens
D_f	– Fractal dimension
N	– Number of boxes used in the box counting method to determine the fractal dimension
ε	– Box's linear size in the box counting method
V	– Volume
$C_{geometric}$	– Geometric center
Ar	– Aspect ratio
Ecc	– Eccentricity
R	– Radius
\bar{R}	– Average radius
ϕ	– Azimuthal angle
θ	– Polar angle
V_{HA}^{XRD}	– Hydroxyapatite volume determined by X-ray diffraction
V_{Whi}^{XRD}	– Whitlockite volume determined by X-ray diffraction
f_{Whi}^{XRD}	– Whitlockite volume fraction determined by X-ray diffraction
$f_{mineral}$	– Mineralized fraction
V_{HA}	– Hydroxyapatite volume
V_{Whi}	– Whitlockite volume
m_{HA}	– Hydroxyapatite mass
m_{Whi}	– Whitlockite mass
$\rho_{sialolith}$	– Specimens' density

- ρ_{mineral} – Mineral density
- $\mu_{\text{specimen}}^{\mu\text{CT}}$ – Specimens' attenuation determined from computed microtomography
- $\mu(r)_{\text{specimen}}^{\mu\text{CT}}$ – Specimens' radial attenuation determined from computed microtomography
- $\mu_{\text{enamel}}^{\mu\text{CT}}$ – Enamel's attenuation determined from computed microtomography
- $\mu_{\text{relative}}^{\mu\text{CT}}$ – Ratio between the specimens' and enamel's attenuation determined from computed microtomography
- $\mu_{\text{specimen}}^{\text{HCT}}$ – Specimens' attenuation determined from helical computed tomography
- $\mu_{\text{agar}}^{\text{HCT}}$ – Agar-agar's attenuation determined from helical computed tomography
- $\mu_{\text{tissue}}^{\text{HCT}}$ – Human soft tissue attenuation determined from helical computed tomography
- $V_{\text{specimen}}^{\mu\text{CT}}$ – Specimens' volume determined from computed microtomography
- $V_{\text{specimen}}^{\text{HCT}}$ – Specimens' volume determined from helical computed tomography
- H – Hardness
- F_{max} – Maximum force applied during the microindentation experiments
- F – Force applied during the indentation experiments
- h_{eff} – Effective indentation depth
- E – Specimen's Young's modulus
- E_{r} – Measured Young's modulus
- E_0 – Indenter's Young's modulus
- ν_0 – Indenter's Poisson ratio
- ν – Specimen's Poisson ratio
- h_{p} – Plastic indentation depth
- d – Indentation diameter

- n_{specimen} – Number of indented specimens
- $n_{\text{indentation}}$ – Number of indentions performed
- λ – Wave length
- Z – Atomic number
- μ – Average value
- σ – Standard deviation
- r – Correlation factor

List of publications related to this thesis:*Papers:*

1. Nolasco P, Coelho PV, Coelho C, Angelo DF, Dias JR, Alves NM, Maurício A, Pereira MFC, Alves de Matos AP, Martins RC, Carvalho PA, Mineral density of sialoliths determined from *ex vivo* and *in vivo* x-ray computed tomography (accepted for publication in *Microscopy and Microanalysis*)
2. Nolasco P, Anjos AJ, Dias J, Coelho PV, Coelho C, Evaristo M, Cavaleiro A, Maurício A, Pereira MFC, Infante V, Alves de Matos AP, Martins RC, Carvalho PA, Local response of sialoliths to lithotripsy: Cues on fragmentation outcome, *Microscopy and Microanalysis*, 23:584-598, 2017
3. Nolasco P, Anjos AJ, Aquino Marques JM, Cabrita F, Carreiro Da Costa E, Maurício A, Pereira MFC, Alves De Matos AP, Carvalho PA, Structure and growth of sialoliths: Computed microtomography and electron microscopy investigation of 30 specimens, *Microscopy and Microanalysis*, 19, 1190-1203, 2013

Conference proceedings:

1. Lopes M, Nolasco P, Coelho C, Coelho PV, Pereira MFC, Alves de Matos AP, Carvalho PA, Oliveira M, Salivary calculi morphology: SEM and μ CT correlative observation, *International Journal Oral Maxillofacial Surgery*, 44: e271, 2015
2. Lopes M, Nolasco P, Coelho C, Coelho PV, Pereira MFC, Alves de Matos AP, Carvalho PA, Oliveira M, Structural analysis of salivary calculi, *International Journal Oral Maxillofacial Surgery*, 44: e271, 2015
3. Nolasco P, Coelho PV, Alves de Matos AP, Maurício A, Pereira MFC, Sanches JMR, Carvalho PA, Mean X-ray Attenuation of salivary calculi computed from microtomography data, *Microscopy and Microanalysis*, 21: 62-63, 2015

4. Anjos AJ, Nolasco P, Aquino Marques JM, Cabrita F, Pereira MFC, Alves de Matos AP, Carvalho PA, On oral calcifications: Tartar and pulp stones, *Microscopy and Microanalysis*, 21: 66 – 67, 2015
5. Anjos AJ, Nolasco P, Aquino Marques JM, Cabrita F, Pereira MFC, Alves de Matos AP, Carvalho PA, On oral calcifications: Sialoliths, dental calculi and tonsilloliths, *Microscopy and Microanalysis*, 19: 23 – 24, 2015
6. Nolasco P, Anjos AJ, Aquino Marques JM, Cabrita F, Pereira MFC, Alves de Matos AP, Carvalho PA, Structural typologies of salivary calculi, *Microscopy and Microanalysis*, 19: 29-30, 2013
7. Nolasco P, Anjos AJ, Almeida A, Aquino Marques JM, Cabrita F, Carreira da Costa E, Mendes JR, Alves de Matos AP, Carvalho PA, Characterization of salivary calculi, *Microscopy and Microanalysis*, 18: 13-14, 2012
8. Nolasco P, Anjos AJ, Almeida A, Aquino Marques JM, Cabrita F, Carreira da Costa E, Mendes JR, Alves de Matos AP, Carvalho PA, Structural characterization of salivary calculi, 2012 IEEE 2nd Portuguese Meeting, Coimbra, Portugal, 1-5, 2012

Chapter 1. Introduction

1.1. Motivation

Lithotripsy methods show a less than desirable success rate in sialolith fragmentation compared to the success rates achieved in urology: 34-69 % for parotid and 32-42 % for submandibular calculi [1-5] vs. typically higher than 80 % for renal calculi [6]. Combination of lithotripsy techniques has been proposed to increase the efficiency of sialolith comminution [7]. However, the therapeutic decisions are compromised by the limited information available on the composition, internal structure and mechanical behaviour of sialoliths, and advanced characterization is necessary to increase the fundamental knowledge on these calcified structures. In addition, the field lacks suitable methodologies of extracting quantitative information from X-ray computed tomography, currently used in sialolithiasis diagnosis [8, 9]. The present work employs a correlative approach to characterize the structure of sialoliths through *in vivo* and *ex vivo* observations and investigates fundamental aspects of their response to mechanical fragmentation and laser ablation.

1.2. State of the art

1.2.1. Sialolithiasis

Sialolithiasis is the presence of calculi (sialoliths) in the parenchyma or ducts of salivary glands [10]. The condition presents a lifetime clinical prevalence of about 0.5 % in the general population [11] occurring predominantly in the submandibular and parotid glands (respectively, 80-90 % and 5-20 %), while sublingual and the minor salivary glands are seldom affected [12, 13]. Sialolithiasis causes pain and swelling of the glandular system by obstruction of the food-related surge of salivary secretions [14], which induces stasis of the saliva and facilitates bacterial ascent [15]. Long-term obstruction, even in the absence of

bacterial infection, leads to atrophy of the involved salivary gland, with concomitant ceasing of the secretory function and, ultimately, fibrosis [16].

Sialoliths' lithogenesis reflects a disorder in the natural occurrence of intracellular and luminal sialomicrooliths [17]. Duct obstruction and/or secretory inactivity lead to stagnant Ca-rich secretory material, which in the presence of cellular debris and phospholipids exposed on damaged cell membranes promote nucleation and growth of calculi [16, 17]. However, these mechanisms and their specific contributions are not well understood.

Sialoliths consist of saliva-based fluids condensed into gel-like networks that act as matrices for deposition of mineral substances [17]. The proportion, distribution and morphology of weakly and highly mineralized regions are variable [18]. Nonetheless, the chemical composition of the mineral and organic components is rather uniform across specimens and patients [19]. The organic matter contains proteins, glycoproteins, mucopolysaccharides and lipids [20-23], while the mineral matter consists of calcium and magnesium phosphates crystallized as hydroxyapatite (HA), whitlockite (Whi) and occasionally brushite or octacalcium [20, 24, 25].

Sialoliths show variable size, with typical diameters between 2 and 10 mm [26], density in the 1.1 - 1.4 g/cm³ range [9, 27], and diversity in the configurations of organic and mineralized regions [16, 17, 28, 29]. In general, their internal structure comprehends one single and well-defined core of organic or mineralized nature, surrounded by approximately concentric layers [30, 31] that, at fine scales, display diverse patterns, ranging from bands of alternating organic/mineral matter to organic globules surrounded by highly mineralized regions [18].

Globules of organic matter have been found on external surfaces [32, 33] as well as on fracture surfaces and polished cross-sections of sialoliths [18]. When dispersed through highly mineralized regions, these organic globules present interfaces evidencing

self-similarity at different scales [28]. The invariant scaling concept of fractal analysis can be empirically used to describe features that are self-similar over extended, but finite, scales, with applications ranging from metallic microstructures [34] to pharmacokinetics [35]. The change in detail of the pattern with the change in scale is defined by the fractal dimension, D_f , as given by the scaling rule [36]: $N \propto \varepsilon^{-D_f}$, where N is the number of boxes of linear size ε required to cover the regions of interest. The fractal dimension is thus a quantitative parameter of the physical phenomenon governing the pattern-forming process [36], and a deeper understanding of the mechanisms behind the formation of sialoliths can be obtained from the growth patterns and local morphology, including the globular self-similar structures.

1.2.2. Diagnosis

Sialoliths are usually diagnosed by X-ray imaging, X-ray sialography, X-ray computed tomography, ultrasonography or magnetic resonance imaging [37]. In addition to size and location of the calculi, these techniques can provide valuable information on the composition and internal structure of sialoliths, which control the response to lithotripsy and are thus relevant for treatment decisions [38, 39].

X-ray helical computed tomography (HCT) is becoming the mainstay imaging method for sialolithiasis diagnosis [40, 41]. Single and dual energy HCT, in *in vivo* and *ex vivo* conditions, have been used to determine the composition and predict the outcome of shock wave lithotripsy of renal calculi [42-49]. However, in the case of sialoliths, fewer tomographic studies have been carried out [8, 9].

The composition of renal calculi is diverse and often two or more distinctive mineral phases can be found in the same specimen [50]. This leads to uncertainty in establishing the composition from *in vivo* HCT due to volume averaging resulting from the relatively poor spatial resolution [46, 51, 52]. In sialoliths, the mineral component is essentially calcium

phosphate, which greatly simplifies the analysis of HCT data and allows inferring the mineralization degree directly from attenuation. Nevertheless, the spatial resolution is still a limiting factor in assessing the fine morphology and dispersion of the mineralized regions in sialoliths.

In HCT, the distance of the object to the source controls the in-plane resolution, while the collimator width, that defines the slice thickness of the scanned region, governs the spatial resolution along the z-axis [53]. These parameters are set by the operator as a function of the level of detail required. However, instrumental characteristics, such as number of detector elements and signal-to-noise ratio typically limit the point resolution to 100-200 micrometers in conventional medical HCT scanners [54].

Cone-beam computed tomography (CBCT) is also available for oral and maxillofacial imaging [55]. These relatively small and inexpensive clinical instruments scan volumes in a single rotation with spatial resolutions similar to HCT [56], while laboratory cone-beam computed microtomography (μ CT) instruments are able to resolve (sub)micrometer details [57]. In CBCT the voxels are typically cubic, and the resulting isotropic spatial resolution is set by the magnification used for the acquisition and is limited by device features such as focal spot size of the source and pixel size of the detector [58]. μ CT has been employed to analyse the composition [59] and validate *in vivo* HCT data of renal calculi [49]. However, *in vivo* X-ray attenuation has not yet been proposed for evaluation of sialoliths' composition to the best of the author's knowledge.

1.2.3. Therapeutic approaches

Depending on the calculus size and location, sialolithiasis management involves different approaches from surgical intervention to minimally invasive or non-invasive methods [60, 61]. The latter reduce local morbidity and promote gland regeneration [62] and include

endoscopic extraction of small sialoliths and endoscopic/extracorporeal lithotripsy of larger sialoliths. Endoscopic lithotripsy relies usually on ultrasonic vibrations [63], ballistic impacts [7] or laser ablation [64], while extracorporeal lithotripsy is performed with focused shock waves [1, 7]. The working principles of these methods are summarized in Figure 1.1 and reviewed below.

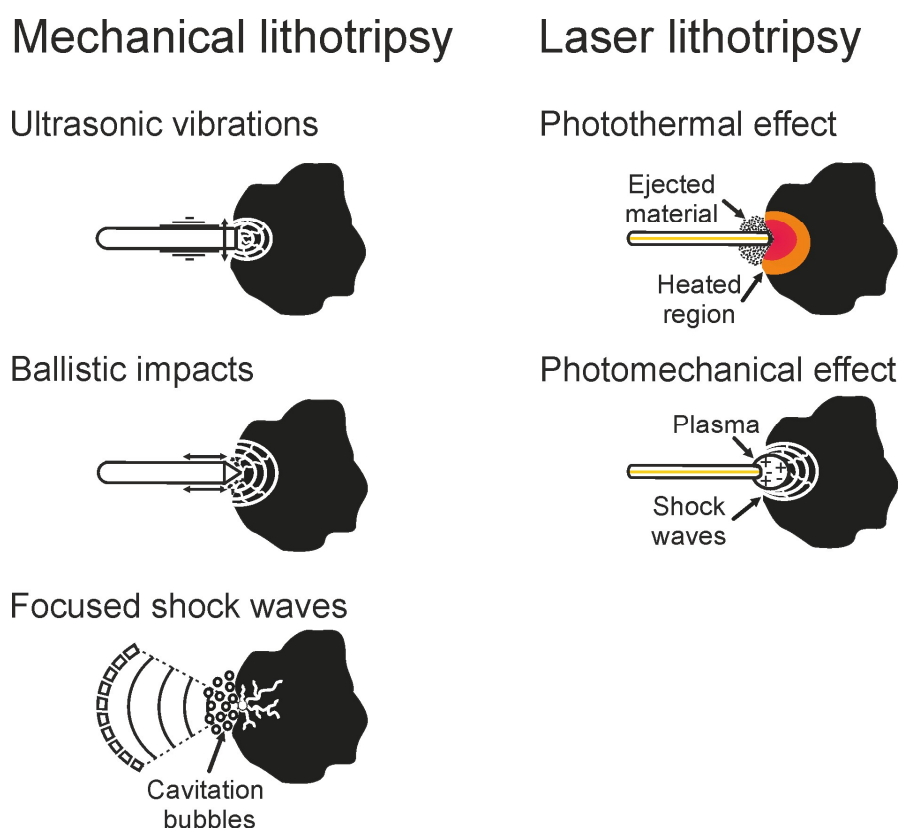


Figure 1.1 - Lithotripsy working principles. Adapted from [63].

Mechanical lithotripsy

The mechanically induced fracture is generally a fatigue process, associated with cavitation, spalling and/or shear stresses:

- Cavitation is the formation of vapour cavities in a liquid subjected to rapid pressure variations [65]. Negative pressures produce bubbles that collapse under positive pressures [66] producing high-speed microjets that induce spalling,

erosion, pitting, microcracking and propagation of compression/tensile waves in adjacent structures [67].

- Spalling refers to flakes breaking off from the calculus surface due to a variety of mechanisms including cavitation, direct impacts and interaction with longitudinal compression/tensile waves. Spalling due to direct impacts occurs at high-stress contact points. Spalling due to longitudinal mechanical waves occurs upon reflection or transmission at interfaces with impedance mismatch (i.e. interfaces that induce phase changes in the waves); the compressive component is reflected/transmitted as a tensile one and adds to the trailing tensile stress of the incident wave. The local amplification of the tensile component leads to spalling. The phenomenon often involves the separation of a spherical cap at the posterior end of the calculus [68]. Layer separation and cleavage of crystals observed in concentric laminated renal calculi have been described as internal spalling [69].
- Fracture induced by shear stresses occurs due to a combination of both shear and compressive stresses that develop as mechanical waves travel through the calculus [70]. These stress fields induce crack nucleation, growth and coalescence at pre-existing defects (such as cavities, inclusions and micro-cracks) leading ultimately to structural failure. In addition, large shear stresses tend to be generated at interfaces, contributing to fragmentation [70, 71].

(I) Ultrasonic vibrations

In ultrasonic lithotripsy, vibrations with 23-25 kHz generated by mechanical, thermal, electrostatic or piezoelectric devices [63] are transmitted directly to the calculus by a rigid probe, which induces local oscillatory stress fields causing a drilling effect at the contact point [72].

(II) *Ballistic impacts*

In ballistic lithotripsy, an endoscopic oscillating projectile (probe) actuated by a pneumatic or electromagnetic device collides with the calculi surface like a jackhammer [63]. Part of the probe's momentum is transferred to the calculus at the contact point from where it propagates divergently. Each pulse is composed of a single wave that induces damage into the calculus structure, mostly by acoustic impedance mismatch across defects/interfaces [73]. The propagation speed of these waves is lower than the speed of sound in the medium, therefore these so-called 'ballistic shocks' cannot be considered shock waves.

(III) *Shock waves*

Shock waves are large-amplitude waves formed by sudden compression of the fluid through which they propagate. Explosions or objects moving at a speed greater than the speed of sound in the medium are able to induce shock waves. Shock wave pulses are generally composed of a single supersonic wave, with a compressive front (shock) of 30 MPa to 110 MPa decaying to a trailing negative pressure of -10 to -15 MPa [74, 75]. The shock wave entering the calculus is divided into pressure (longitudinal) and shear (transversal) components (Figure 1.2) that induce, respectively, compressive/tensile and shear stress fields in the calculus structure, producing cavitation, spalling and/or shear induced fracture [76]. External shock wave lithotripsy (ESWL) relies on electrohydraulic, electromagnetic or piezoelectric devices to produce shock waves that are focused by means of acoustic lenses into the focal zone, where the energy flux reaches a maximum [76]. Dedicated external devices with associated imaging systems are required to target the calculus with minimal injury to the surrounding tissues.

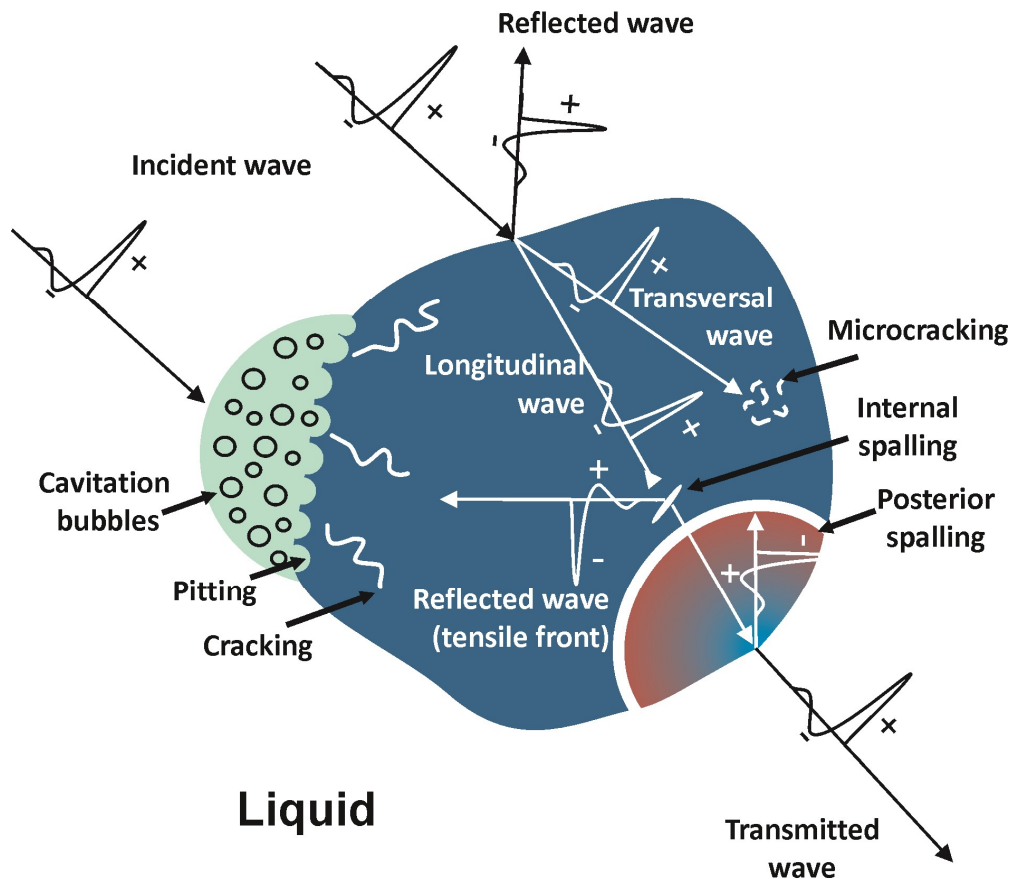


Figure 1.2 - Interaction of mechanical waves with the calculus structure. Adapted from [69] and [77].

Laser lithotripsy

Laser ablation is induced by photothermal and/or photomechanical interactions depending on the laser parameters (wavelength, power density, pulse frequency and pulse duration) and on the physical properties of the calculus [78, 79]:

- Photothermal interactions are typical of long-pulsed lasers, i.e., lasers with pulse durations between 250 μs and 750 μs [80]. The energy transmitted to the calculus structure causes a confined heat accumulation that produces local phase changes and ejection of the melted/vaporized material from the irradiated area [78] (Figure 1.3).

- Photomechanical interactions result from expansions induced by microexplosions and/or thermoelastic phenomena that depend on the local thermal absorption coefficient [78, 79]. Vaporization of hydration water can produce a sudden increase in pressure and ensuing microexplosions that lead to rupture of the surrounding structure [81]. The absorbed energy also causes an elastic expansion that can directly induce local fracture by spalling [82]. In addition, photomechanical interactions with the surrounding media (saliva) may generate explosions and plasma expansion/collapse phenomena [78] resulting in shock waves that propagate through and beyond the irradiated volume (Figure 1.3).

The predominance of each of these damage mechanisms is governed by the laser parameters and the chemical/structural characteristics of the irradiated system [79].

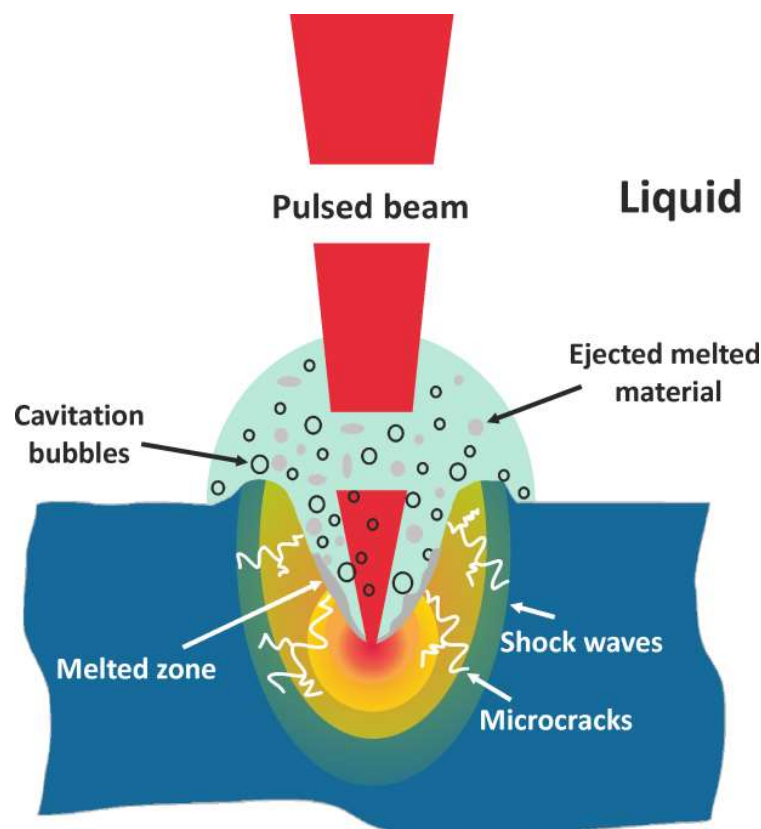


Figure 1.3 – In laser ablation photothermal effects are responsible for central melting while photomechanical interactions affect mostly the surrounding regions. Adapted from [83].

The extension of damage caused by ultrasonic vibrations, ballistic impacts, shock waves and photo-induced microexplosions or thermoelastic phenomena is expected to be critically dependent on the sialoliths' mechanical properties [69, 81]. Specifically:

- In the short timescales involved, the calculus resistance to deformation is essentially determined by the Young's modulus.
- The resistance to cavitation-microjet impact is governed by the local hardness.
- The resistance to spalling and crack propagation is ruled by fracture toughness.

1.3. Work summary

In this thesis, an interdisciplinary approach and correlative methodologies are used to investigate the chemistry, internal structure, growth patterns and mechanical behaviour of sialoliths, as well as the local response to laser and shock wave lithotripsy.

Chapter 2 presents the experimental details and techniques employed in the characterization of sialoliths, namely, field-emission scanning electron microscopy (SEM) and transmission electron microscopy (TEM), combined with energy-dispersive spectroscopy (EDS); X-ray diffraction (XRD); Fourier transform infrared spectroscopy (FTIR) and atomic emission spectroscopy (AES); nano and micro indentation; X-ray computed microtomography (μ CT) and X-ray helical computed tomography (HCT); laser lithotripsy and mechanical lithotripsy.

In Chapter 3, μ CT, SEM, TEM and EDS are used to investigate the local structure and growth patterns of submandibular and parotid sialoliths. An interdisciplinary approach and innovative methodologies have been employed, namely: petrographic methods for SEM sample preparation, as well μ CT versus SEM versus TEM correlative evaluation together

with fractal analysis of cross-sectional SEM images. The results have been used to elucidate lithogenesis mechanisms.

In Chapter 4, relations between calculi composition/density and average μ CT attenuation are established, and the characterization scheme implemented is validated for HCT following a correlative strategy between *in vivo* and *ex vivo* scans.

In Chapter 5, the hardness and Young's modulus of sialoliths are determined at different scales by indentation techniques. Specific damage induced in the structure of sialoliths by the lithotripsy methods are investigated by SEM and μ CT. The fundamental aspects of the response of sialoliths to mechanical fragmentation and laser ablation are discussed.

Finally, in Chapter 6, the conclusions and directions for future work are laid out.

1.4. References

1. Iro H, *et al.*, Outcome of minimally invasive management of salivary calculi in 4,691 patients, *Laryngoscope*, 119:263-268, 2009
2. Escudier MP, *et al.*, Extracorporeal shockwave lithotripsy in the management of salivary calculi, *Br J Surg*, 90:482-485, 2003
3. Capaccio P, *et al.*, Extracorporeal lithotripsy for salivary calculi: a long-term clinical experience, *Laryngoscope*, 114:1069-1073, 2004
4. Zenk J, *et al.*, Extracorporeal shock wave lithotripsy of submandibular stones: evaluation after 10 years, *Ann Otol Rhinol Laryngol*, 113:378-383, 2004
5. Schmitz S, *et al.*, Long-term evaluation of extracorporeal shock wave lithotripsy in the treatment of salivary stones, *J Laryngol Otol*, 122:65-71, 2008
6. Abe T, *et al.*, Outcomes of shockwave lithotripsy for upper urinary-tract stones: a large-scale study at a single institution, *J Endourol*, 19:768-773, 2005

7. Capaccio P, *et al.*, Modern management of obstructive salivary diseases, *Acta Otorhinolaryngol Ital*, 27:161-172, 2007
8. Escudier MP, *et al.*, Factors influencing the outcome of extracorporeal shock wave lithotripsy in the management of salivary calculi, *Laryngoscope*, 120:1545-1549, 2010
9. Schrotzlmaier F, *et al.*, Laser lithotripsy of salivary stones: Correlation with physical and radiological parameters, *Lasers Surg Med*, 47:342-349, 2015
10. Harrison JD, Histology and pathology of sialolithiasis, In *Salivary Gland Diseases: Surgical And Medical Management*, Witt RL (ed), New York, Stuttgart, Thieme, pp.71-78, 2006
11. Escudier MP, Epidemiology and aetiology of salivary calculi, In *Controversies in the Management of Salivary Gland Disease*, McGurk M, Combes JG (eds), Oxford, Oxford University Press, pp.251-259, 2001
12. Bodner L, Salivary gland calculi: diagnostic imaging and surgical management, *Compendium*, 14:572-578 1993
13. Szalma J, *et al.*, [Diagnostic value of radiographic and ultrasonic examinations in patients with sialoadenitis and sialolithiasis], *Fogorv Sz*, 100:53-58, 2007
14. Siddiqui SJ, Sialolithiasis: an unusually large submandibular salivary stone, *Br Dent J*, 193:89-91, 2002
15. Seifert G, Oralpathologie I: Pathologie der Speicheldrüsen, (ed. 1st), Berlin, Springer Berlin Heidelberg, 1996
16. Harrison JD, Causes, natural history, and incidence of salivary stones and obstructions, *Otolaryngol Clin North Am*, 42:927-947, 2009
17. Harrison JD, Natural history of chronic sialadenitis and sialolithiasis, In *Modern Management Preserving the Salivary Glands*, Nahlieli O, McGurk M, Iro H, Zenk J (eds), Herzeliya, Isradon Publishing House, pp.93–135, 2007
18. Alves de Matos AP, *et al.*, On the structural diversity of sialoliths, *Microsc Microanal*, 13:390-396, 2007

19. Chaudhary M, Chaudhary SD, Essentials of pediatric oral pathology, (ed. 1st), New Dheli, JP Medical Ltd, 2012
20. Sabot JF, *et al.*, Analytical investigation of salivary calculi, by mid-infrared spectroscopy, *Analyst*, 137:2095-2100, 2012
21. Boskey AL, *et al.*, Lipids associated with mineralization of human submandibular gland sialoliths, *Arch Oral Biol*, 26:779-785, 1981
22. Slomiany BL, *et al.*, Lipid composition of the matrix of human submandibular salivary gland stones, *Arch Oral Biol*, 27:673-677, 1982
23. Kinoshita H, *et al.*, Phosphate and amide III mapping in sialoliths with Raman microspectroscopy, *J Raman Spectrosc*, 39:349-353, 2008
24. Sakae T, *et al.*, Mode of occurrence of brushite and whitlockite in a sialolith, *J Dent Res*, 60:842-844, 1981
25. Teymoortash A, *et al.*, Sialolith crystals localized intraglandularly and in the Wharton's duct of the human submandibular gland: an X-ray diffraction analysis, *Arch Oral Biol*, 48:233-236, 2003
26. Kraaij S, *et al.*, Salivary stones: symptoms, aetiology, biochemical composition and treatment, *Br Dent J*, 217:E23, 2014
27. Ho SP, *et al.*, Kidney stones compared to Dental calculi and Salivary stones: Comparative analyses of mineral density and ultrastructure, *J Urol*, 195:e778-e779, 2016
28. Alves de Matos AP, *et al.*, Ultrastructural and EDS study of sialoliths of the salivary glands, *Microsc Microanal*, 11:152-153, 2005
29. Tanaka N, *et al.*, Ultrastructural analysis of salivary calculus in combination with X-ray microanalysis, *Med Electron Microsc*, 36:120-126, 2003
30. Kasaboğlu O, *et al.*, Micromorphology of sialoliths in submandibular salivary gland: A scanning electron microscope and X-ray diffraction analysis, *J Oral Maxillofac Surg*, 62:1253-1258, 2004

31. Szalma J, *et al.*, Proteomic and scanning electron microscopic analysis of submandibular sialoliths, *Clin Oral Investig*, 17:1709-1717, 2013
32. Lustmann J, Shteyer A, Salivary calculi: ultrastructural morphology and bacterial etiology, *J Dent Res*, 60:1386-1395, 1981
33. Giray CB, *et al.*, Sialolith characterization by scanning electron microscopy and X-ray photoelectron spectroscopy, *Scanning*, 29:206-210, 2007
34. Hornbogen E, Fractals in microstructure of metals, *Int Mater Rev*, 34:277-296, 1989
35. Pereira LM, Fractal pharmacokinetics, *Comput Math Methods Med*, 11:161-184, 2010
36. Mandelbrot BB, *The Fractal Geometry of Nature*, (ed. 1st), San Francisco, W.H Freeman and Co., 1982
37. Rzymska-Grala I, *et al.*, Salivary gland calculi - contemporary methods of imaging, *Pol J Radiol*, 75:25-37, 2010
38. Zhong P, *et al.*, Characterization of fracture toughness of renal calculi using a microindentation technique, *J Mater Sci Lett*, 12:1460-1462, 1993
39. Chuong CJ, *et al.*, Acoustic and mechanical properties of renal calculi: implications in shock wave lithotripsy, *J Endourol*, 7:437-444, 1993
40. Kalia V, *et al.*, CT Scan as an Essential Tool in Diagnosis of Non-radiopaque Sialoliths, *J Maxillofac Oral Surg*, 14:240-244, 2015
41. Yousem DM, *et al.*, Major salivary gland imaging, *Radiol*, 216:19-29, 2000
42. Joseph P, *et al.*, Computerized tomography attenuation value of renal calculus: can it predict successful fragmentation of the calculus by extracorporeal shock wave lithotripsy? A preliminary study, *J Urol*, 167:1968-1971, 2002
43. Pareek G, *et al.*, Hounsfield units on computerized tomography predict stone-free rates after extracorporeal shock wave lithotripsy, *J Urol*, 169:1679-1681, 2003

44. Gupta NP, *et al.*, Role of computed tomography with no contrast medium enhancement in predicting the outcome of extracorporeal shock wave lithotripsy for urinary calculi, *BJU Int*, 95:1285-1288, 2005
45. Wang LJ, *et al.*, Predictions of outcomes of renal stones after extracorporeal shock wave lithotripsy from stone characteristics determined by unenhanced helical computed tomography: a multivariate analysis, *Eur Radiol*, 15:2238-2243, 2005
46. Saw KC, *et al.*, Helical CT of urinary calculi: effect of stone composition, stone size, and scan collimation, *AJR Am J Roentgenol*, 175:329-332, 2000
47. Sheir KZ, *et al.*, Determination of the chemical composition of urinary calculi by noncontrast spiral computerized tomography, *Urol Res*, 33:99-104, 2005
48. Nakada SY, *et al.*, Determination of stone composition by noncontrast spiral computed tomography in the clinical setting, *Urology*, 55:816-819, 2000
49. Zarse CA, *et al.*, Helical computed tomography accurately reports urinary stone composition using attenuation values: in vitro verification using high-resolution micro-computed tomography calibrated to fourier transform infrared microspectroscopy, *Urology*, 63:828-833, 2004
50. Daudon M, *et al.*, Sex- and age-related composition of 10 617 calculi analyzed by infrared spectroscopy, *Urol Res*, 23:319-326, 1995
51. Mostafavi MR, *et al.*, Accurate determination of chemical composition of urinary calculi by spiral computerized tomography, *J Urol*, 159:673-675, 1998
52. Williams JC, Jr., *et al.*, Progress in the use of helical CT for imaging urinary calculi, *J Endourol*, 18:937-941, 2004
53. Webb A, Introduction to biomedical imaging, Wiley-IEEE Press, 2003
54. Ketcham RA, Carlson WD, Acquisition, optimization and interpretation of X-ray computed tomographic imagery: Applications to the geosciences, *Computers & Geosciences*, 27:381-400, 2001

55. Nemeth B, *et al.*, Unusual form of sialolithiasis: case report with 3-dimensional imaging, *Br J Oral Maxillofac Surg*, 54:e17, 2016
56. Abdel-Wahed N, *et al.*, Assessment of the role of cone beam computed sialography in diagnosing salivary gland lesions, *Imaging Sci Dent*, 43:17-23, 2013
57. SkyScan NV, SkyScan 1172 Desktop X-ray microtomography Instruction manual, Aartselaar, N.V SkyScan 2005
58. Staude A, Goebbels J, Determining the Spatial Resolution in Computed Tomography – Comparison of MTF and Line-Pair Structures In *International Symposium on Digital Industrial Radiology and Computed Tomography*, Berlin, Germany, 2011
59. Tatón G, *et al.*, Renal calculi composition studies with the use of microtomography, *Cent European J Urol*, 6:87-90, 2010
60. Baumash HD, Submandibular salivary stones: current management modalities, *J Oral Maxillofac Surg*, 62:369-378, 2004
61. McGurk M, *et al.*, Modern management of salivary calculi, *Br J Surg*, 92:107-112, 2005
62. Nishi M, *et al.*, Evaluation of submandibular gland function by sialo-scintigraphy following sialolithectomy, *J Oral Maxillofac Surg*, 45:567-571, 1987
63. Zheng W, Denstedt JD, Intracorporeal lithotripsy. Update on technology, *Urol Clin North Am*, 27:301-313, 2000
64. Phillips J, Withrow K, Outcomes of Holmium Laser-Assisted Lithotripsy with Sialendoscopy in Treatment of Sialolithiasis, *Otolaryngol Head Neck Surg*, 150:962-967, 2014
65. Coleman AJ, Saunders JE, A review of the physical properties and biological effects of the high amplitude acoustic field used in extracorporeal lithotripsy, *Ultrason*, 31:75-89, 1993
66. Blake JR, Gibson DC, Cavitation Bubbles Near Boundaries, *Annu Rev Fluid Mech*, 19:99-123, 1987

67. Chuong CJ, *et al.*, Stone Damage Modes During Piezoelectric Shock Wave Delivery, In *Shock Wave Lithotripsy 2: Urinary and Biliary Lithotripsy*, Lingeman JE, Newman DM (eds), Boston, MA, Springer US, pp.103-106, 1989
68. Sass W, *et al.*, The mechanisms of stone disintegration by shock waves, *Ultrasound Med Biol*, 17:239-243, 1991
69. Zhong P, Preminger GM, Mechanisms of differing stone fragility in extracorporeal shockwave lithotripsy, *J Endourol*, 8:263-268, 1994
70. Cleveland RO, Sapozhnikov OA, Modeling elastic wave propagation in kidney stones with application to shock wave lithotripsy, *J Acoust Soc Am*, 118:2667-2676, 2005
71. Xi X, Zhong P, Dynamic photoelastic study of the transient stress field in solids during shock wave lithotripsy, *J Acoust Soc Am*, 109:1226-1239, 2001
72. Gur U, *et al.*, Ureteral ultrasonic lithotripsy revisited: a neglected tool?, *J Endourol*, 18:137-140, 2004
73. Wess O, Physics and technology of shock wave and pressure wave therapy, (ed. 1st), Tägerwilen Switzerland, Storz Medical AG, 2007
74. Lokhandwalla M, Sturtevant B, Fracture mechanics model of stone comminution in ESWL and implications for tissue damage, *Phys Med Biol*, 45:1923-1940, 2000
75. Caballero A, Molinari JF, Finite element simulations of kidney stones fragmentation by direct impact: Tool geometry and multiple impacts, *Int J Eng Sci*, 48:253-264, 2010
76. Cleveland RO, McAteer JA, The Physics of Shock Wave Lithotripsy, In *Extracorporeal Shock Wave Lithotripsy*, Smith AD, Gopal H, Preminger GM, Kavoussi LR (eds), pp.317-332, 2012
77. Thiel M, *et al.*, The use of shock waves in medicine--a tool of the modern OR: an overview of basic physical principles, history and research, *Minim Invasive Ther Allied Technol*, 9:247-253, 2000

-
78. Lee H, *et al.*, The Advent of Laser Therapies in Dermatology and Urology: Underlying Mechanisms, Recent Trends and Future Directions, *J. Opt. Soc. Korea*, 13:321-329, 2009
 79. Zezell DM, Aparecida AP, High power lasers and their interaction with biological tissues, In *Lasers in Dentistry*, John Wiley & Sons, Inc, pp.11-18, 2015
 80. Wang B, *et al.*, Laser Lithotripsy, In *Ureteroscopy: Indications, Instrumentation & Technique*, Monga M (ed), New York, USA, Springer, pp.321-329, 2013
 81. Majaron B, *et al.*, Thermo-mechanical laser ablation of soft biological tissue: modeling the micro-explosions, *Appl Phys B*, 69:71-80, 1999
 82. Itzkan I, *et al.*, The thermoelastic basis of short pulsed laser ablation of biological tissue, *Proc Natl Acad Sci U S A*, 92:1960-1964, 1995
 83. Muller D, Haupt O, Short-Pulse Lasers Enable Transparent Materials Processing, <http://www.photonics.com/Article.aspx?AID=56800>, (22-05-2015)

Chapter 2. Experimental

2.1. Materials and methods

2.1.1. Samples

Six parotid and sixty four submandibular sialoliths (respectively P_n with $n = 1, \dots, 6$ and S_n with $n = 1, \dots, 62$) were surgically removed from consenting patients at the Department of Maxillofacial Surgery of Hospital de São José (in Lisbon, Portugal), following procedures approved by the hospital ethical committee. After extraction, twenty-six submandibular and six parotid specimens were kept dry at room temperature, while thirty-eight submandibular specimens were immersed in thymol 0.1 % and stored at 4 °C to minimize chemical modification. Seven of the twenty-six submandibular dry specimens were rehydrated in thymol 0.1 % and stored at 4 °C. The mass of all sialoliths was monitored throughout the sample preparation steps. Saliva samples were collected from consenting patients, transferred into Petri dishes, dried in an oven at 45 °C for 48 h and subsequently analysed.

Sialoliths subsets were randomly selected for each characterization experiment. Only μ CT, SEM and TEM observations were performed on parotid sialoliths, given the small size and low prevalence of these specimens.

2.1.2. Petrographic sample preparation

Submandibular and parotid sialoliths were partially encapsulated in epoxy resin with high viscosity (Struers) to avoid sample impregnation, and sectioned through the core or through peripheral regions (Figure 2.1).

The test surfaces were grinded with 800 and 1000-grit SiC paper and polished with 6 μ m and 1 μ m diamond suspensions. Special care was taken to minimize smearing and dehydration of the organic structures during sample preparation, which would hinder clear observation and correct chemical evaluation of the specimens' cross-sections.

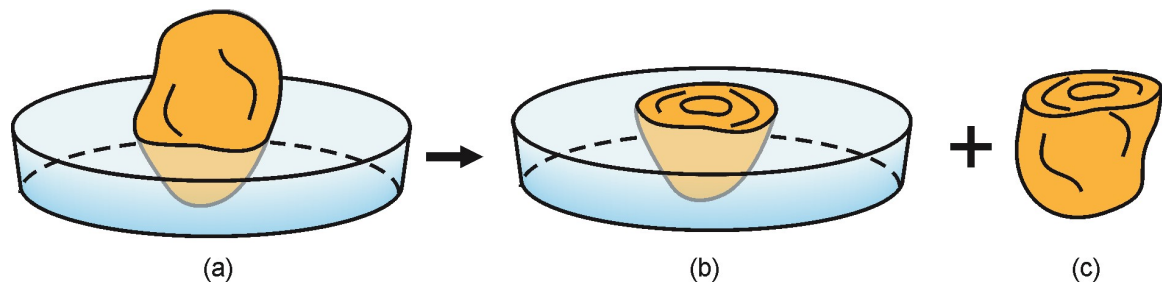


Figure 2.1. Part of the sialolith was embedded in epoxy resin (a) and subsequently ground and polished for scanning electron microscopy observation and mechanical testing (b), whereas the non-embedded part (c) was subsequently prepared for spectroscopy experiments.

The included/embedded samples (Figure 2.1 (b)) were subsequently used for scanning electron microscopy observations, indentation, ultrasonic, pneumoballistic and laser lithotripsy experiments.

2.1.3. TEM sample preparation

TEM sample preparation involved collecting selected pieces from the specimens, fixation in 3 % glutaraldehyde (pH 7.4) for 24 h, washing and further fixation in 1 % osmium tetroxide for 1 h. 0.1 M sodium cacodylate buffer was used in all these steps. Dehydration was subsequently carried out in ascending concentrations of ethanol, and propylene oxide was used as an intermediate solvent before embedding in an Epon-Araldite resin. Infiltration was carried out at 4 °C for one week with daily replacement of resin. Ensuing polymerization was performed at 60 °C for 3 days. The blocks were then sectioned with a Richert UM 2 ultra-microtome (Leica®) equipped with a diamond knife. Contrast was further enhanced with uranyl acetate and lead citrate staining. As the heavy elements introduced in the fixation and staining steps tended to interfere with the subsequent chemical analyses, some samples were analysed unstained. All consumables and reagents were purchased from VWR.

2.1.2 Microscopy observations

SEM images were obtained with secondary electrons (SE) and/or backscattered electrons (BSE) using a JSM 7001F instrument (JEOL) equipped for X-ray energy dispersive spectrometry (Oxford Instruments). X-ray energy dispersive spectroscopy (EDS) standardless quantification was performed using ZAF correction. Prior to microscopic observation the samples were coated with carbon (≈ 30 nm of thickness) using a Q150R sputter/carbon coater (Quorum Technologies).

The fractal dimension D_f of globular structures was calculated with the fractal box counting method using the FracLac plugin [1] of the ImageJ software package [2]. This involved binarization of the images, application of masks to remove unwanted details and counting the number of boxes (N) of a given side length (ε) needed to cover the relevant features. If the $N \propto \varepsilon^{-D_f}$ scaling rule is followed, on logarithmic scale the experimental (N, ε) points lie on a straight line whose slope approximates D_f . The mean fractal dimension was determined for each image using 250 grid sizes and 12 different grid positions generated randomly.

Structural details at higher resolution were investigated by TEM using a JEOL 100SX instrument operated at 80 KV and a Hitachi H8100 instrument equipped for EDS and operated at 200 KV. Selected area electron diffraction and electron microdiffraction experiments were carried out to investigate the crystalline phases present in the sialoliths. Powder (kinematical) diffraction patterns were simulated for comparison with the PowderCell software package [3] using the lattice parameters and atomic positions reported for hydroxyapatite [4]. Dynamical diffraction patterns were simulated for single crystals with the (dynamical) NCEMSS software package [5].

2.1.3 Chemical and structure characterization

Previous investigations by EDS showed that the mineralized regions in sialoliths are rich in Ca and P and may include Mg [6]. In the present work, the concentration of these elements has been determined by inductive coupled plasma atomic emission spectrometry (ICP-AES) with a PerkinElmer Optima 2000 DV instrument (PerkinElmer Inc.).

FTIR spectra of the calculi, saliva and pure hydroxyapatite (AgoraMat, Altakitin) were acquired with a PerkinElmer Spectrum 65 FTIR Spectrometer (PerkinElmer Inc.) using the KBr pellet method. The spectra have been interpreted through available literature [7-11].

X-ray powder diffraction was performed with an Xpert PANalytical Pro diffractometer (PANalytical) using Cu K α radiation ($\lambda = 0.15$ nm). The diffractograms were recorded between $10^\circ < 2\theta < 60^\circ$, with a step size of 0.005° at a rate of 0.001 step/s. Identification of mineral phases, determination of lattice parameters and quantification of volume fractions were performed using the PowderCell software package [3], with structural parameters retrieved from the literature [4, 12, 13].

Sample preparation for FTIR and XRD involved maceration to a fine powder and dehydration at 45 °C for 48 h, while for elemental analysis the powder was further calcined at 550 °C and dissolved in 1 % HCl and 1 % NH_3 (VWR) acidic solution at 50 °C.

2.1.4 Computed microtomography

The μ CT characterization of submandibular and parotid specimens was performed with SkyScan 1172 and 1174 instruments (Bruker) with constant source power of, respectively, 10 W and 40 W, while the voltage and current were tuned to maximize contrast. The specimens were covered rotated over 360° with 0.7° steps and the isotropic voxel size was selected in the 10-20 μm range to fit the acquisition's field of view to the specimen size. The X-ray radiation was filtered with a built-in 0.5 mm aluminium foil to mitigate beam hardening. The

analyses performed with μ CT throughout this work are indicated below:

- Tomographic characterization of the ultrastructure of dry submandibular and parotid sialoliths (15 acquisitions in SkyScan 1172).
- Tomographic characterization and evaluation of average X-ray attenuation of hydrated and rehydrated submandibular specimens (21 acquisitions in SkyScan 1172 and 4 acquisitions in SkyScan 1174), which have been wrapped in parafilm (Sigma-Aldrich) to minimized dehydration during the scans. These acquisitions were calibrated with customized phantoms scanned simultaneously with the specimens. Since commercially available μ CT phantoms have a density below that of sialoliths [14], enamel on a human tooth, extracted from a consenting patient, and orthodontic wax (Sunstar) were used instead. Tooth enamel was specifically selected to test the possible use of patient teeth for calibration of X-ray attenuation in clinical context.
- Tomographic evaluation of lithotripsy damage (4 acquisitions in SkyScan 1172) and macroindentation size in immobilized hydrated submandibular sialoliths (5 acquisitions in SkyScan 1172).

The NRecon 1.6.3 SkyScan software package (SkyScan, Bruker) was used for 3D reconstruction by a modified Feldkamp cone-beam algorithm [15]. The parameter of the built-in beam hardening correction was set to 40 % [16], while the parameter for reduction of ring artifacts was optimized individually for each data set. The reconstructed data was saved as 16 bits TIF files.

Binary masks of the calculi and phantoms were generated with the CT-analyser (CTan) SkyScan software package (SkyScan, Bruker), using the Otsu binarization method [17] followed by background noise removal. Subsequent data processing of the calibrated acquisitions was carried out in Matlab® environment as described below.

Offset and gain calibrations were performed by adjusting the average attenuation of the orthodontic wax and enamel to, respectively, 0 % and 40 % of the bit resolution. The latter avoided saturation of the regions with highest mineral density. Average X-ray attenuation for specimens and phantoms was defined as the mean of a Gaussian distribution estimated by maximum likelihood. Geometrical features such as volume (V), center ($C_{\text{geometric}}$) and aspect ratio (Ar) have been determined for each sialolith. The nucleation site, identified by visual inspection, was used to determine the nucleation eccentricity (Ecc) defined as the distance between the apparent nucleation center and the geometric center, normalized to the specimens' average radius \bar{R} .

The mineralization evolution was assessed through radial attenuation profiles, i.e., integrated attenuation around concentric spheres as a function of the distance to the nucleation center. Since the surface of the calculi reflected internal convolutions, linear warping was employed to conform the shape of each sialolith to a sphere of radius \bar{R} (Figure 2.2) before extracting radial data. The warped coordinates (R, ϕ, θ) for each cubic voxel were determined from the average difference between the specimen's surface and the sphere of radius \bar{R} (red arrows in Figure 2.2) for the solid angle defined by the voxel diameter and the distance R to the nucleation center (see projected cones in Figure 2.2). For most specimens, the profiles started at the center of the nucleation region, however, for sialoliths without an evident nucleus, the geometric center was used instead as initiation site for the profiles.

The density of each sialolith was determined from the measured mass and from the volume established from μ CT measurements, both in hydrated conditions.

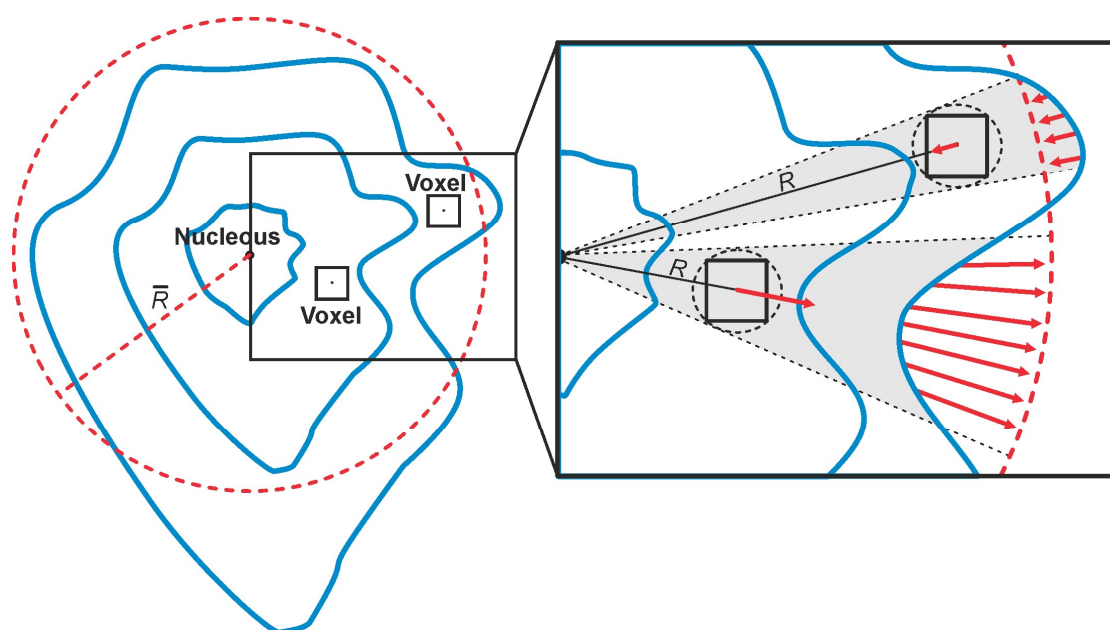


Figure 2.2 – Schematic representation of the method used to determine the warped coordinates of each voxel in the μ CT datasets. The goal was to conform the external shape of the sialolith to a sphere in order to obtain radial profiles reflecting the internal convolutions.

2.1.5 Helical computed tomography

Three *in vivo* HCT acquisitions were carried out using a Light Speed GE VCT 64 Medical Systems instrument (GE Healthcare) (2 submandibular specimens) at the Department of Radiology of the Hospital de São José (in Lisbon, Portugal) and a Brilliance 16 Philips instrument (Philips) (1 submandibular specimen) at the Department of Radiology of the Hospital de Santa Maria (in Lisbon, Portugal). The *in vivo* data were acquired using the standard cranial acquisition protocols employed at each clinical institution: scans using the GE instrument were performed at 120 kV, with the power automatically modulated between 6-19 kW to maximize contrast, a slice thickness of 0.63 mm, z-axis resolution of 0.63 mm and in-plane resolution ranging between 0.54 and 0.56 mm and a pitch of 0.97; the scan with the Philips instrument was acquired at 120 kV, with constant power of 23 kW, slice thickness of 1.50 mm, pitch of 0.50, interpolated z-axis resolution of 0.75 mm and in-plane resolution of

0.28 mm.

Fourteen *ex vivo* HCT acquisitions were carried out using the GE instrument, with the hydrated specimens (7 submandibular sialoliths) and phantoms (enamel and orthodontic wax) included in a 2 % agar-agar matrix (VWR). The scans were performed at 120 kV, using constant power of 30 kW, a pitch of 0.97, a slice thickness of 0.63 mm, an in-plane resolution ranging between 0.19 - 0.76 mm and an interpolated z-axis resolution ranging between 0.19 - 0.63 mm.

Reconstruction of *in vivo* and *ex vivo* HCT datasets was performed with the instruments' built-in software and data were saved as 12 bits TIF files. Standard and type-B head convolution kernels [18] were used to reconstruct the data acquired, respectively, with the GE and Philips instruments. The binary masks for the sialoliths and phantoms were generated in Matlab® environment following the methodology employed for μ CT. The offset and gain of the *ex vivo* HCT datasets acquired with the GE instrument were established using orthodontic wax and enamel, as well as μ CT-calibrated sialoliths, as phantoms. These calibrations were also employed for *in vivo* HCT datasets acquired with the same machine.

2.1.6 Mechanical characterization

Sets of 100 nanoindentations have been performed at room temperature on polished surfaces of three dry submandibular sialoliths with different mineralization levels using a NanoTest Vantage instrument (Micro Materials) with a Berkovich indenter, a load of 3 mN and a dwell time of 30 s. Posterior SEM observation was used to exclude indentations laying in defective regions. The local hardness (H) and Young's modulus (E) were calculated employing the Oliver and Pharr method [19] using a polynomial fit.

Microindentations have been performed on polished surfaces of 5 dry and 5 hydrated

submandibular sialoliths using a H100 Fischerscope (Fischer Technology Inc.) at room temperature with a Vickers indenter, a load of 1 N and a dwell time of 10 s. The hardness and Young's modulus were calculated using equation (1) and (2) [20].

$$H = \frac{F_{max}}{24.5 h_{eff}^2} \quad (1)$$

$$E = \frac{E_r \frac{E_0}{(1-\nu_0^2)}}{(1-\nu^2)} \quad \text{with} \quad E_r = \frac{1}{2h_p} \sqrt{\frac{\pi}{24.5}} \frac{dP}{dh} \quad (2)$$

where F_{max} is the maximum load applied, h_{eff} and h_p are, respectively, the effective and the plastic depths, E_r is the measured Young's modulus while E_0 and E are, respectively, the indenter and sample Young's moduli, and ν_0 and ν are the indenter and the sample Poisson ratios, respectively.

Average mechanical properties have been determined from nano and microindentation data by fitting 2-D Gaussian distributions to the experimental values using maximum likelihood estimation.

Central and peripheral macroindentations have been performed at room temperature on polished surfaces of five hydrated submandibular sialoliths using an AVK-C2 Vickers hardness testing instrument (Mitutoyo) with a Vickers indenter, a load of 300 N and 500 N and a dwell time of 10 s.

2.1.7 Lithotripsy experiments

Ultrasonic and pneumoballistic fragmentation experiments were performed on hydrated submandibular specimens immobilized in epoxy resin and immersed in physiologic serum (B. Braun). Ultrasonic fragmentation was performed with a Satelec Suprasson PMax scaler (Acteon Group Ltd) with a round tip of 0.5 mm in diameter operated at 30 kHz in continuous

mode until surface erosion was evident. Pneumoballistic impacts were generated with a CH 1347 EMS Lithoclast instrument (Electro Medical Systems) using a probe of 0.8 mm in diameter, a pressure of 3 bar and a maximum of 3 pulses at 3 pulses/min.

Shock wave fragmentation was carried out on hydrated specimens immersed in physiologic serum and sealed inside a thin polyethylene bag (VWR) and embedded in a 2 % agar-agar matrix (VWR) to mimic the physical constraints inside the human body. Two sets of 4000 shock wave pulses were delivered through the agar-agar matrix using a PiezoLith 3000 plus ESWL system (Richard Wolf) operated with focal diameter of 4 mm, pressure of 80 MPa and pulse frequency of 2 Hz.

Laser lithotripsy was performed using a Medilas H20 Holmium laser ($\lambda = 2.1 \mu\text{m}$) (Dornier MedTech GmbH) with a 270 μm diameter optic fiber, a pulse energy of 800 mJ (6.4 W) and 8 Hz pulse frequency. The experiments were carried out on hydrated specimens immobilized in epoxy resin and immersed in physiologic serum. During ablation the energy density was varied between 2.8 and 22.4 kJ/m^2 .

2.2 References

1. Karperien A, FracLac for ImageJ, <http://rsb.info.nih.gov/ij/plugins/fraclac/FLHelp/Introduction.htm>, (1999-2013)
2. Schindelin J, *et al.*, Fiji: an open-source platform for biological-image analysis, *Nat Methods*, 9:676-682, 2012
3. Kraus W, Nolze G, POWDER CELL - a program for the representation and manipulation of crystal structures and calculation of the resulting X-ray powder patterns, *J Appl Crystallogr*, 29:301-303, 1996

4. Gomes S, *et al.*, Thorough analysis of silicon substitution in biphasic calcium phosphate bioceramics: a multi-technique study, *Acta Biomater*, 6:3264-3274, 2010
5. Kilaas R, Interactive simulation of high resolution electron micrographs, In *45th annual meeting of the Electron Microscopy Society of America*, Baltimore, MD, USA, Lawrence Berkeley Lab, CA (USA), pp. 66-69, 1987
6. Alves de Matos AP, *et al.*, On the structural diversity of sialoliths, *Microsc Microanal*, 13:390-396, 2007
7. Sabot JF, *et al.*, Analytical investigation of salivary calculi, by mid-infrared spectroscopy, *Analyst*, 137:2095-2100, 2012
8. Rehman I, Bonfield W, Characterization of hydroxyapatite and carbonated apatite by photo acoustic FTIR spectroscopy, *J Mater Sci Mater Med*, 8:1-4, 1997
9. Movasaghi Z, *et al.*, Fourier Transform Infrared (FTIR) Spectroscopy of Biological Tissues, *Appl Spectrosc Rev*, 43:134-179, 2008
10. Jayasree RS, *et al.*, Spectroscopic and thermal analysis of a submandibular sialolith of Wharton's duct resected using Nd:YAG laser, *Lasers Med Sci*, 23:125-131, 2008
11. Kong J, Yu S, Fourier transform infrared spectroscopic analysis of protein secondary structures, *Acta Biochim Biophys Sin (Shanghai)*, 39:549-559, 2007
12. Ivanova TI, *et al.*, Crystal Structure of Calcium-Deficient Carbonated Hydroxyapatite. Thermal Decomposition, *J Solid State Chem*, 160:340-349, 2001
13. Gopal R, *et al.*, Crystal Structure of Synthetic Mg-Whitlockite, $\text{Ca}_{18}\text{Mg}_2\text{H}_2(\text{PO}_4)_{14}$, *Can J Chem*, 52:1155-1164, 1974
14. SkyScan NV, SkyScan micro-CT support products, <https://www.microphotonics.com/wp-content/uploads/2016/01/SkyScanmicroCTsupportproductsDistributorsPLSno-price.pdf>, (29-09-2017)
15. Feldkamp LA, *et al.*, Practical cone-beam algorithm, *J. Opt. Soc. Am. A*, 1:612-619, 1984

16. Tarplee MFV, Corps N, Acquiring optimal quality X-ray μ CT scans, *Application note Queen Mary University of London*, 93-97, 2008
17. Otsu N, A Threshold Selection Method from Gray-Level Histograms, *EEE Trans Syst., Man, Cybern., Syst*, 9:62-66, 1979
18. Geyer LL, *et al.*, State of the Art: Iterative CT Reconstruction Techniques, *Radiol*, 276:339-357, 2015
19. Oliver WC, Pharr GM, Measurement of hardness and elastic modulus by instrumented indentation: Advances in understanding and refinements to methodology, *J Mater Res*, 19:3-20, 2004
20. Doerner MF, Nix WD, A method for interpreting the data from depth-sensing indentation instruments, *J Mater Res*, 1:601-609, 1986

Chapter 3. Sialoliths ultrastructure

Overview

In this chapter, X-ray computed microtomography (μ CT), field-emission scanning electron microscopy (SEM) and transmission electron microscopy (TEM), combined with energy dispersive spectroscopy (EDS), are used to investigate the ultrastructure and growth patterns of submandibular and parotid sialoliths. An interdisciplinary approach and innovative methodologies are employed, namely, μ CT vs SEM vs TEM correlative evaluation together with fractal analysis of cross-sectional SEM images, to obtain new insights into the mechanisms of nucleation and growth of salivary calculi.

3.1. Results

3.1.1. General configuration

Figure 3.1 shows examples of longitudinal sections of submandibular (S_n) and parotid (P_n) sialoliths selected from 3-D reconstructions so as to crosscut the core whenever such a predominant structure could be identified. Most sialoliths showed a single well-defined major core (S_{12} , S_{13} , S_{15} , S_{17} , S_{18} , S_{19} , S_{21} , S_{22} , S_{24} , S_{25}), some did not show such a core (S_{10} , S_{11} , S_{16} , P_5 , P_6), and one showed several (P_4). Major cores displayed either distinctively higher or lower mineralization than the surrounding regions as inferred from the brighter/darker contrast in the radiographic data (e.g., S_{21} , S_{22} , S_{24} or S_{25} vs S_{12} , S_{13} or S_{15}). Apart from the cores, there were concentric growth patterns (e.g. S_{12} and S_{15}) or irregular ones (e.g. S_{16} and P_6). Yet in many situations, a gradation between these two architectures was observed. The X-ray attenuation profiles varied in the studied set and even within the same specimen (see profiles for S_{12} and S_{25} included in Figure 3.1).

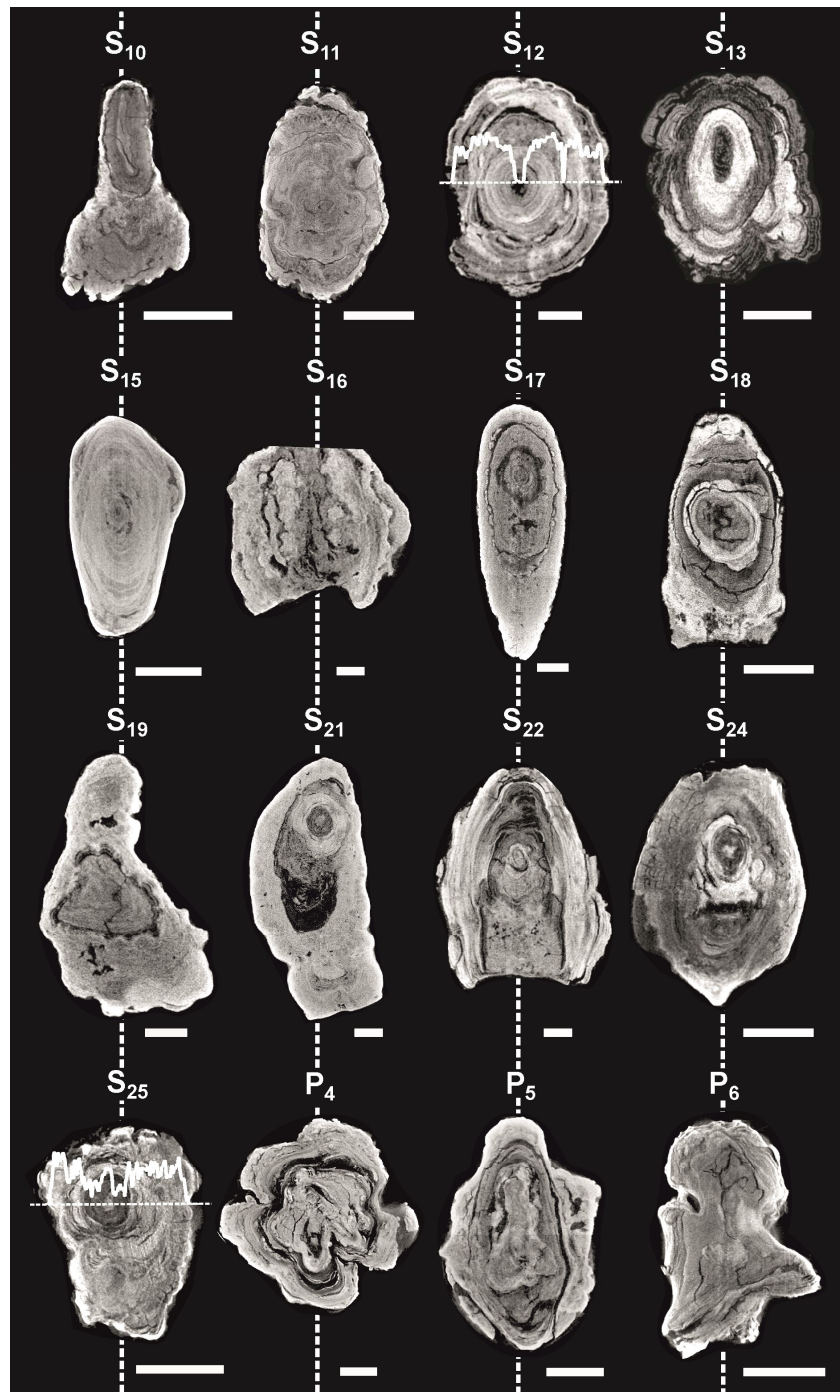


Figure 3.1 - Median longitudinal cross-sections of submandibular (S_n) and parotid (P_n) sialoliths obtained from μ CT data. Brighter regions represent higher mineralization and dark regions represent essentially organic matter. Horizontal attenuation profiles crossing the specimens' core are shown for S_{12} and S_{25} . The vertical dashed lines indicate the major axis, which in the case of quasi-equiaxed sialoliths has been established taking into account the internal structure. Scale bar is 2 mm.

SEM observation of the specimens revealed that, in general, the core lacked layering or any other distinctive features. The subsequent growth resulted in patterns that could be classified into four general types depending on their organization (concentric vs irregular) and mineralization (high vs low) as illustrated in Figure 3.2. Submandibular and parotid sialoliths showed similar features. Shrinkage cracks observed in Figures 3.1 and 3.2 resulted from the drying processes that occurred during sample preparation procedures for SEM.

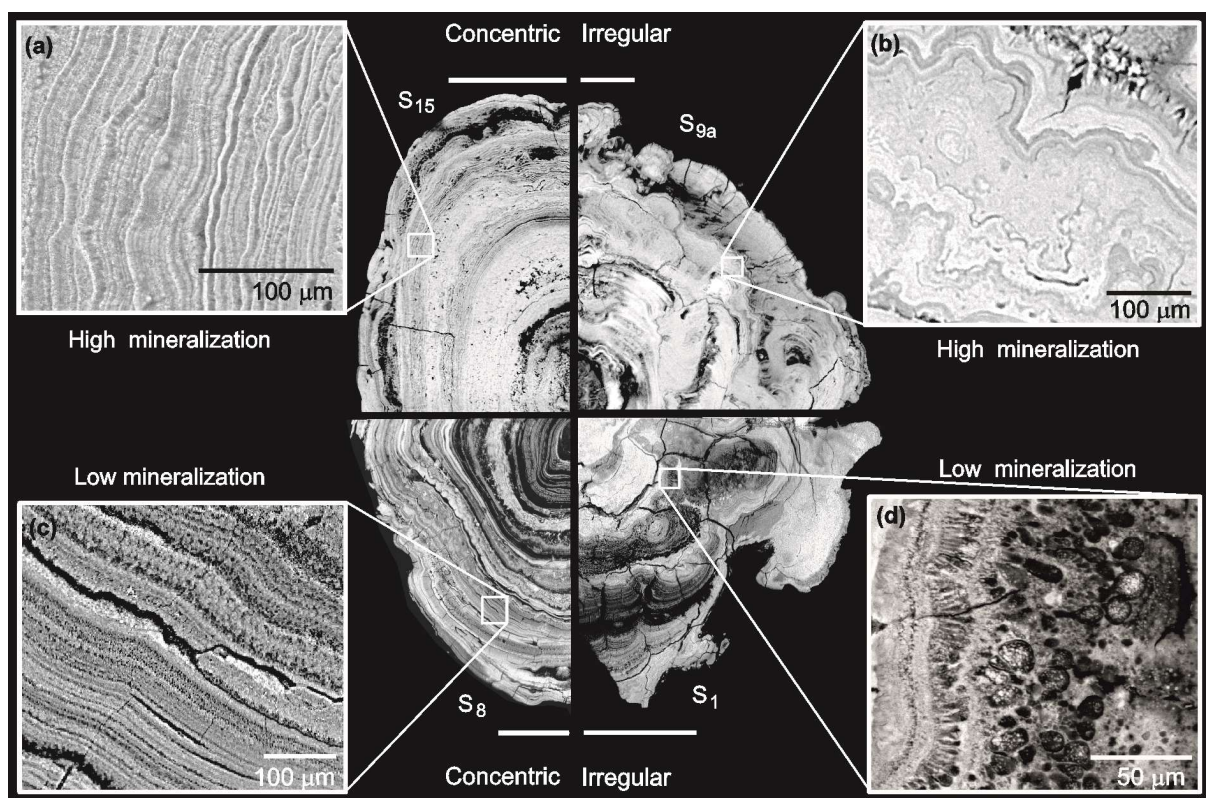


Figure 3.2 - Array of SEM (backscattered electron (BSE)) images showing representative growth patterns: left, concentric; right, irregular; top, high mineralization; and bottom, low mineralization. The magnified details show the local features of each pattern. Scale bar is 1 mm.

3.1.2. Local structure

At finer scales the sialoliths showed banded regions, globular regions or combinations of the two and various degrees of mineralization (Figure 3.3). Concentric patterns consisted essentially of highly mineralized bands alternating with bands of organic matter (Figure 3.3 (a)). The contrast differences in the alternating mineralized/organic bands are related to the density of crystalline nanoparticles dispersed in the organic matrix rather than on a clear segregation between organic and mineralized phases (magnified detail of Figure 3.3 (a)). Nevertheless, in most instances of either concentric or irregular growth patterns, the fine structure of the sialolith was threaded with globules of variable size and mineralization (Figure 3.3 (b) to (d)). Mineralized nodules were found on calculi external surfaces and internal voids (Figure 3.3 (e)) and also seen surrounded by layers of calcified material (Figure 3.3 (f)). Convolute lamellar structures of an apparently organic nature were seen at peripheral regions (Figure 3.3 (g)).

X-ray maps and EDS point analyses revealed a consistent chemistry: mineralized regions contain a high fraction of Ca, P and O and a minor presence of Mg, while the organic matter showed higher S and C content than the adjacent mineralized matrix (Figures 3.4 and 3.5).

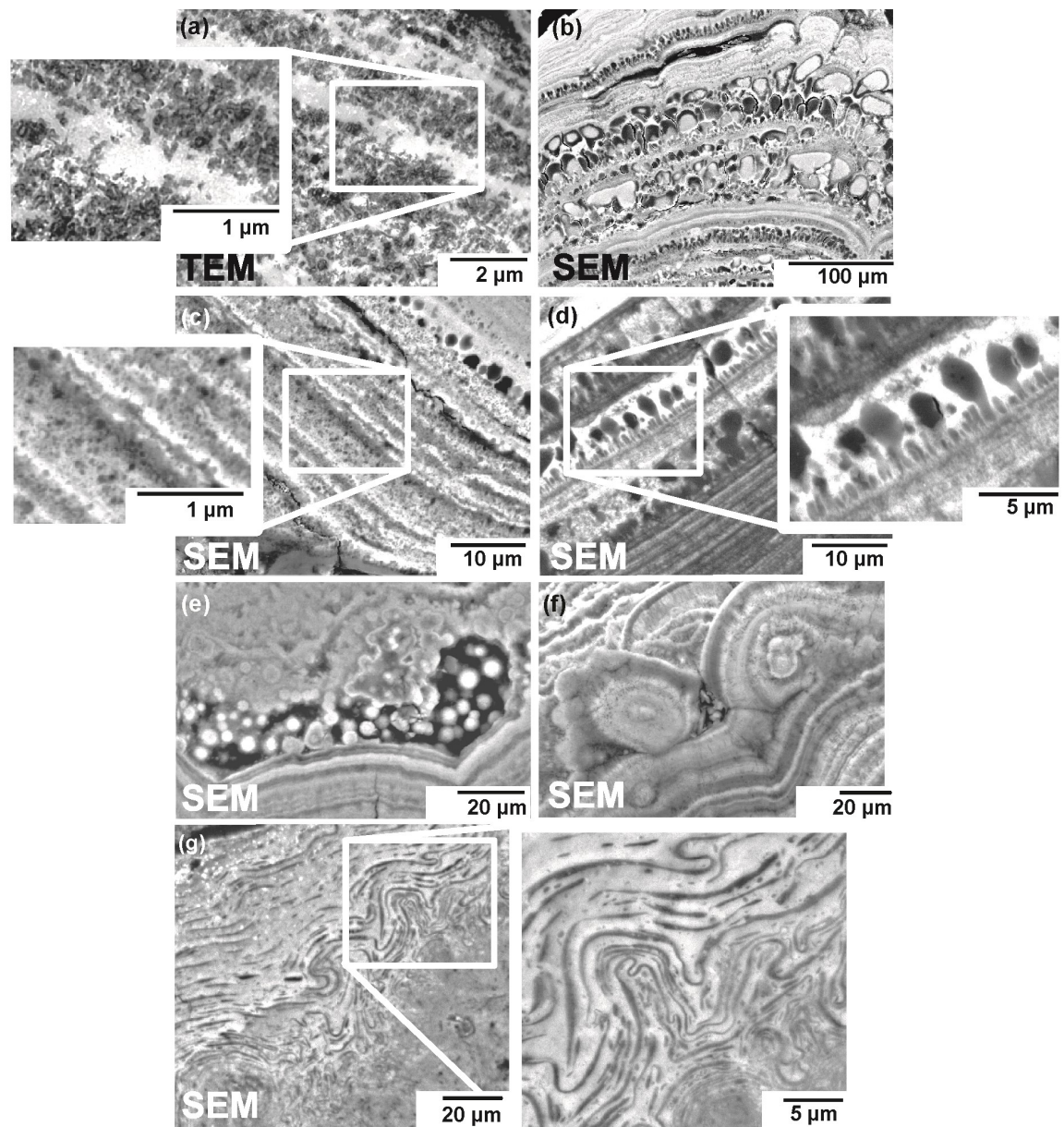


Figure 3.3 – (a) TEM image of alternating mineralized/organic bands. The magnified detail reveals the difference in precipitate density. (b)–(d) SEM images (BSE) of banded structures threaded with organic globules of variable size and mineralization. (e) SEM (secondary electron (SE)) image of mineralized nodules in an internal void. (f) SEM (BSE) image of mineralized nodules in banded layers. (g) Convoluted organic structures at the periphery of a sialolith.

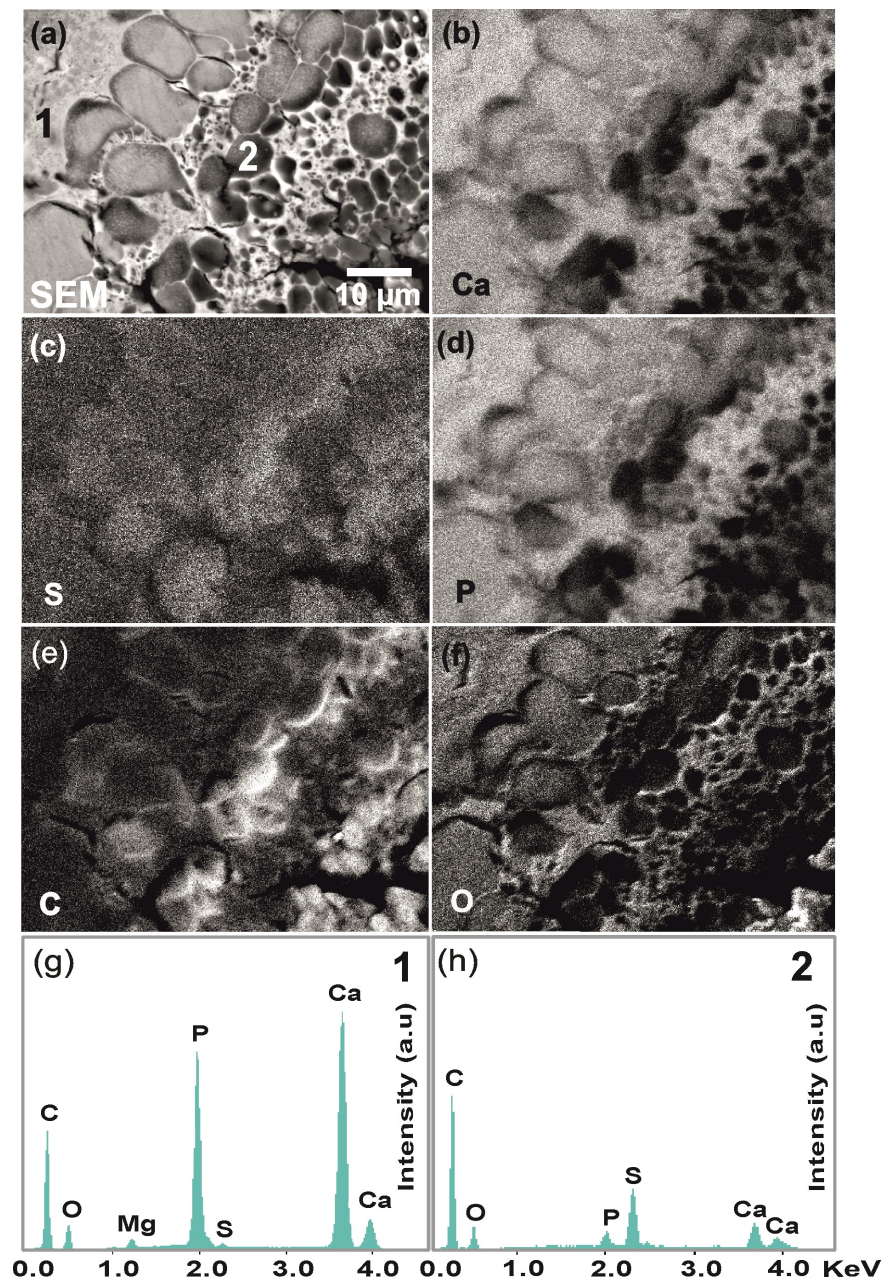


Figure 3.4 – (a) SEM (BSE) image of a globular region in a submandibular sialolith with corresponding X-ray maps for (b) Ca, (c) S, (d) P, (e) C, and (f) O. Spectra resulting from point analyses of a heavily mineralized region ((g) from region 1 in (a)) and of an organic globule ((h) from region 2 in (a)) The two spectra have been normalized for a constant background level.

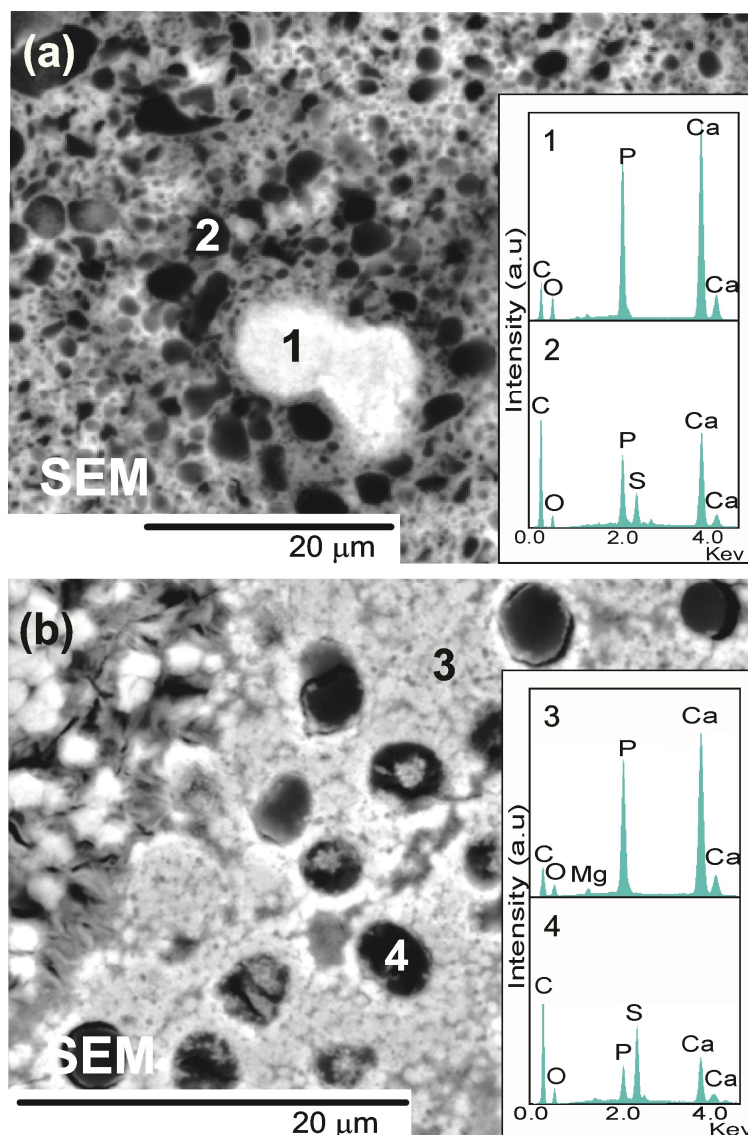


Figure 3.5 - SEM (BSE) images of organic globules dispersed in mineralized regions. (a) Organic matter with relatively low sulfur content in a submandibular sialolith. (b) Sulfur-rich globules in a parotid sialolith. The spectra have been normalized using the background level.

Some variability was detected in the sulfur content, as evaluated from the S/Ca peak ratio of spectra obtained in regions of organic matter large enough to minimize the influence of the adjacent mineralized regions (compare the spectrum 2 in Figure 3.5 (a) with Figure 3.4 (g)). At this level, the chemistry of submandibular and parotid sialoliths was similar (Figure 3.5 (b)). The low signal in the spectra of regions of organic matter (Figure 3.4 (h) and insets 2 and 4 in Figure 3.5) probably resulted from the high hydrogen content and absence of heavy elements, leading to an apparently disproportional presence of sulphur.

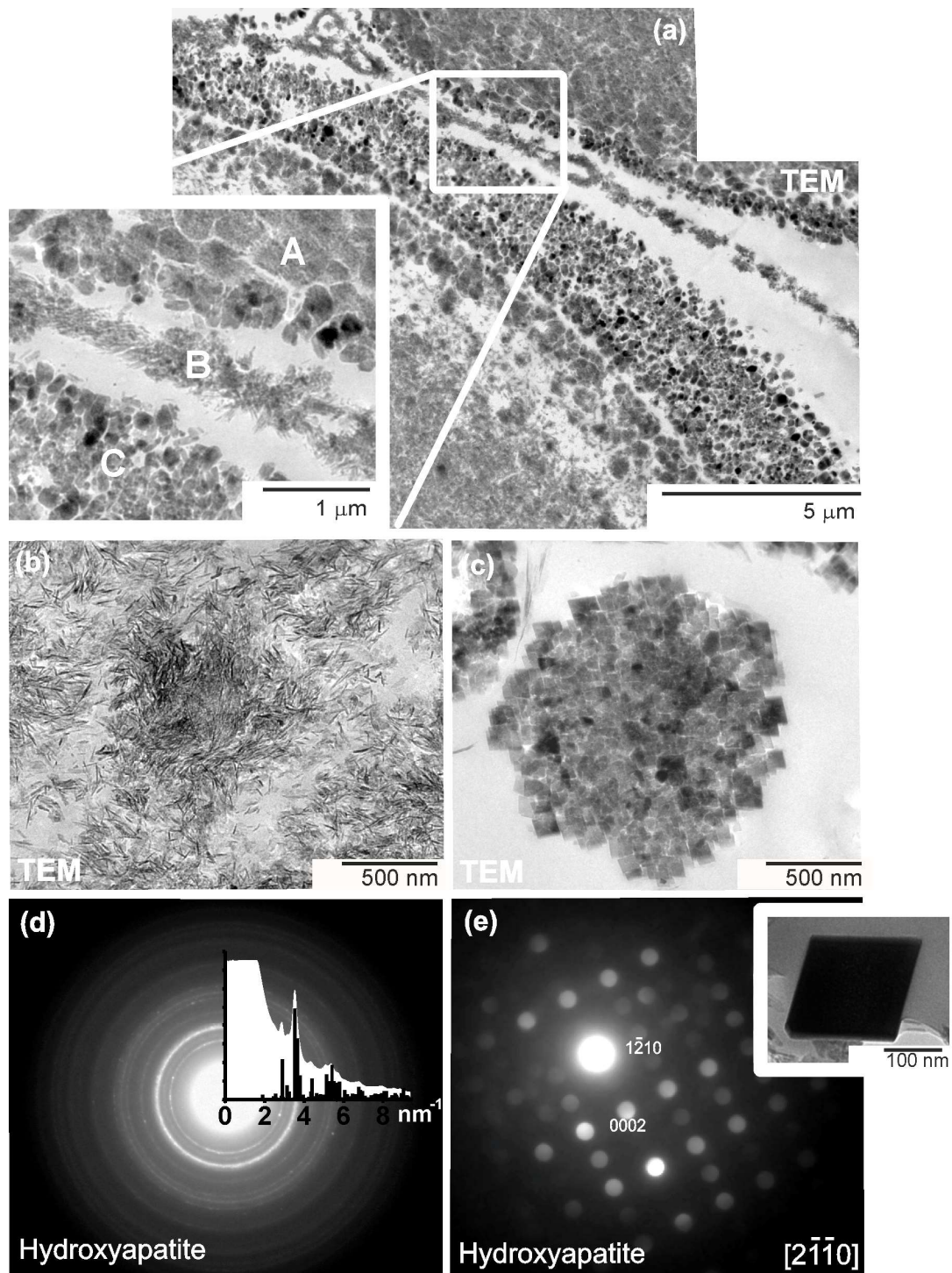


Figure 3.6 - TEM images and electron diffraction patterns of crystals. (a) Coexisting crystals of different structures: A, colonies of filamentary crystals; B, needlelike crystals; C, large single crystals. (b) Filamentary crystals. (c) Agglomerate of parallelepiped crystals. (d) Ring electron diffraction pattern obtained from a region of filamentary crystals showing the radial integrated intensity together with a simulation for hydroxyapatite. (e) Microdiffraction pattern of a single crystal indexed for hydroxyapatite.

Filamentary, needlelike and parallelepiped crystals were commonly found in the sialoliths (A, B and C, respectively, in Figure 3.6 (a), (b) and (c)). Selected area diffraction experiments carried out in regions of filamentary and needlelike crystals resulted in ring patterns that matched simulations for hydroxyapatite with lattice parameters: $a = 0.95$ nm and $c = 0.69$ nm (Figure 3.6 (d)). Microdiffraction experiments carried out with single crystals revealed a crystalline structure compatible with the hexagonal system and the structure of hydroxyapatite (Figure 3.6 (e)). Phases such as the trigonal whitlockite, the monoclinic brushite, the triclinic octacalcium phosphate and the tetragonal weddellite, which have been previously reported [1-3] could not be matched to any of the powder or single diffraction patterns obtained by TEM.

The globules showed a variable degree of mineralization (Figure 3.4) reflecting a non-uniform crystallization of the Ca- and P-based electrolytes (Figures 3.7). In general, the first evidence of mineralization/crystallization was seen at the periphery of the globules (magnified detail of Figure 3.7 (a)) in organic regions poorly stained by osmium tetroxide (arrows in Figure 3.7 (a)). The mineralization of the globules appears to occur via 3 distinct mechanisms:

- (i) Nucleation on the internal wall of the globule (heterogeneous nucleation) of filamentary crystals (Figure 3.7 (b) and (c)) with mineralization extending into the internal region through a discontinuous precipitation front.
- (ii) Precipitation throughout the internal region of relatively large particles, usually parallelepiped, displaying diffraction contrast characteristic of single crystals (Figure 3.7 (d) and (e)). In these cases, nucleation occurred in the organic matrix without the assistance of an existing interface (homogeneous nucleation).
- (iii) Precipitation of crystal colonies throughout the internal region of the globule. The colonies were constituted by filamentary crystals (Figure 3.6 (b) and A in magnified

detail of Figure 3.6 (a)), needlelike crystals (Figure 3.7 (f)) or parallelepiped ones (Figure 3.6 (c) and (e)).

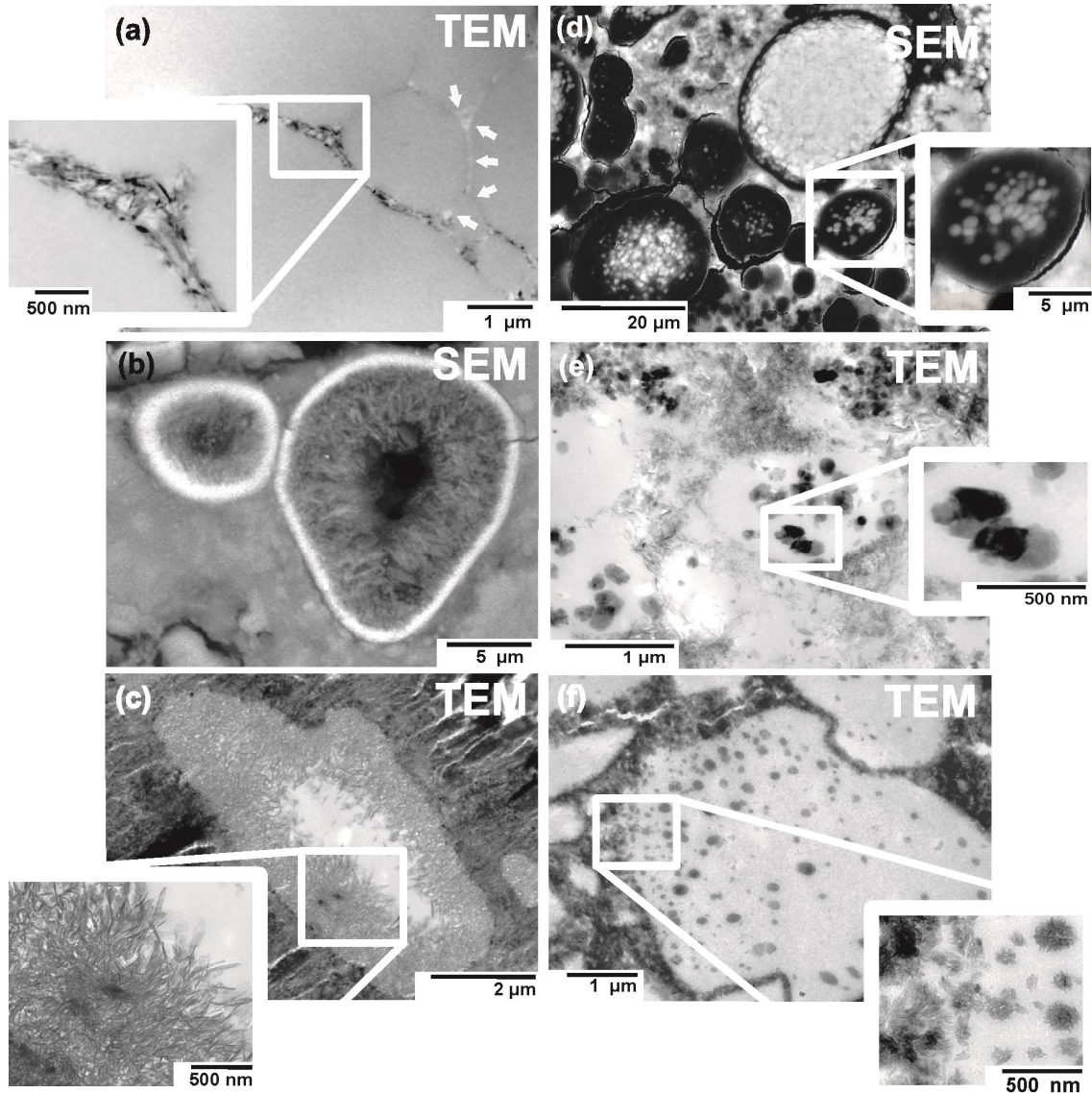


Figure 3.7 – (a) TEM image of globular structures showing that the onset of mineralization/crystallization is associated with peripheral organic substances weakly stained by OsO_4 (arrows). (b) SEM (BSE) image of internal mineralization occurring through heterogeneous nucleation at the globule wall. (c) TEM image of filamentary crystals extending inward from the globule wall. (d) SEM (BSE) image of organic globules with internal mineralization through homogeneous nucleation. (e) TEM image of homogeneously nucleated particles displaying diffraction contrast. (f) TEM image of needlelike crystals extending from the mineralized periphery to the internal region of a globule.

The correlative interpretation of SEM and TEM images should take into account the fact that in SEM images (BSE mode) the bright features correspond to mineralized regions (higher average atomic number), while in TEM images the mineralized/crystalline regions appear dark in bright-field imaging due to heavy element staining and/or diffraction.

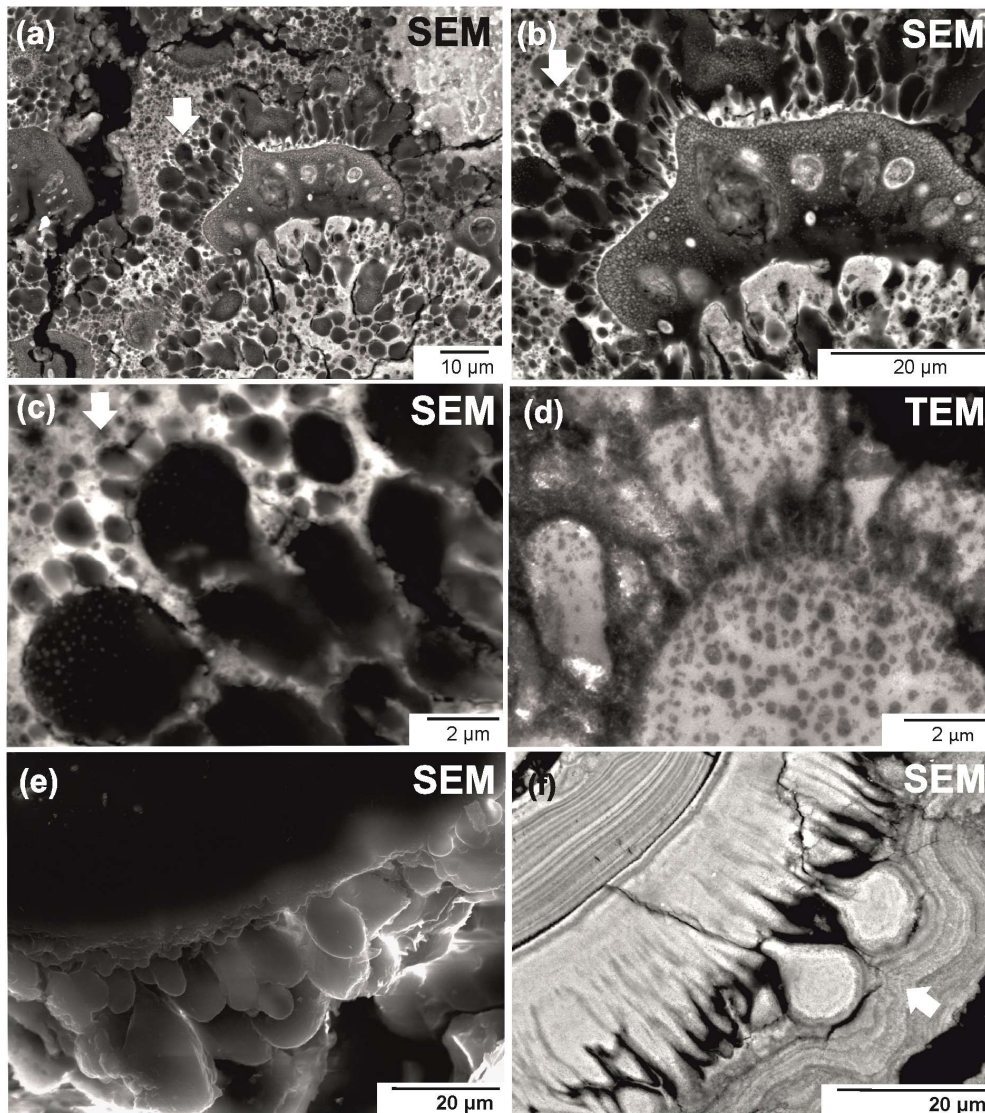


Figure 3.8 – (a)–(c) SEM (BSE) images at increasing magnifications of fingerlike globular structures with self-similarity. Arrow indicates same location. (d) TEM image showing globular structures with self-similarity. (e) SEM (SE) image showing extruded globules at a void. (f) SEM (BSE) image of mineralized extruded globules enclosed by an external mineralized layer (arrow).

The morphology of the organic globules is compatible with the injection of a low-viscosity fluid through another fluid of higher viscosity (magnified detail of Figure 3.4 (d)), and the self-similar globules are consistent with a successive occurrence of this process (arrows in Figure 3.8 (a) to (c)). The resulting globules are frequently fingerlike and usually less mineralized than the parent globule (Figure 3.8 (b) and (d)), which indicates that the pores in the adjacent mineralized matter tend to filter the largest precipitates during the process.

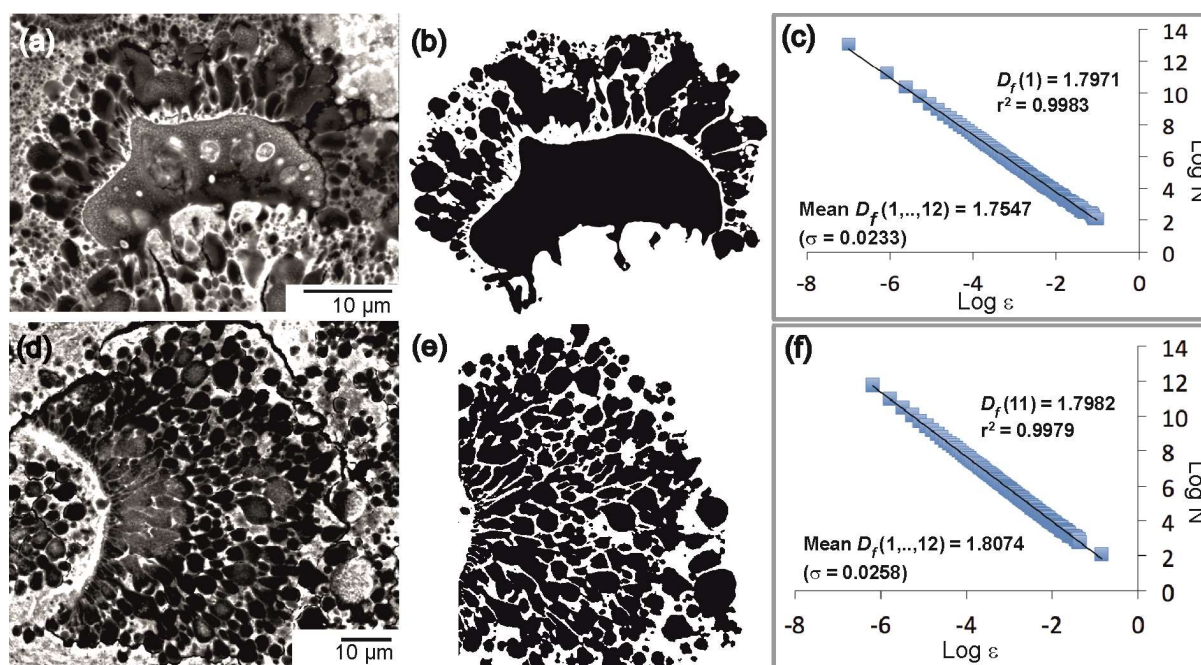


Figure 3.9 – (a), (d) BSE (SEM) images showing fingerlike globular structures. (b), (e) Binarized images where unwanted detail has been masked prior to fractal analysis. (c), (f) Results obtained for randomly generated $k = 1, \dots, 12$ positions of grids oriented as the image. The side length ε was defined as a fraction of the original image. One of the 12 regressions is shown for each image with the respective fractal dimension $D_f(k)$ and correlation coefficient r to attest for the self-similarity of the globular structures. The legends also show the mean fractal dimension and standard deviation (σ) of the 12 different positions $D_f(1, \dots, 12)$.

Analogous structures could be observed by SEM and TEM (compare Figure 3.8 (c) and (d)). In some instances, there was also evidence of an extrusion process with the formation of globules in voids (Figure 3.8 (e)), and extruded globules were also seen

enclosed by mineralized layers (Figure 3.8 (f)). A mean fractal dimension $D_f = 1.8$ was determined for the biphasic interpenetration by the box counting method for SEM images showing self-similar morphologies (Figure 3.9).

Bacteria with variable degrees of mineralization were present in the sialoliths with evidence of cell division (Figure 3.10). Some extensive colonies were detected although their presence was not universal (Figure 3.10 (a) and (b)). An association between these colonies and either heavily mineralized regions or globules of organic matter was not found (see Figure 3.10 (c)).

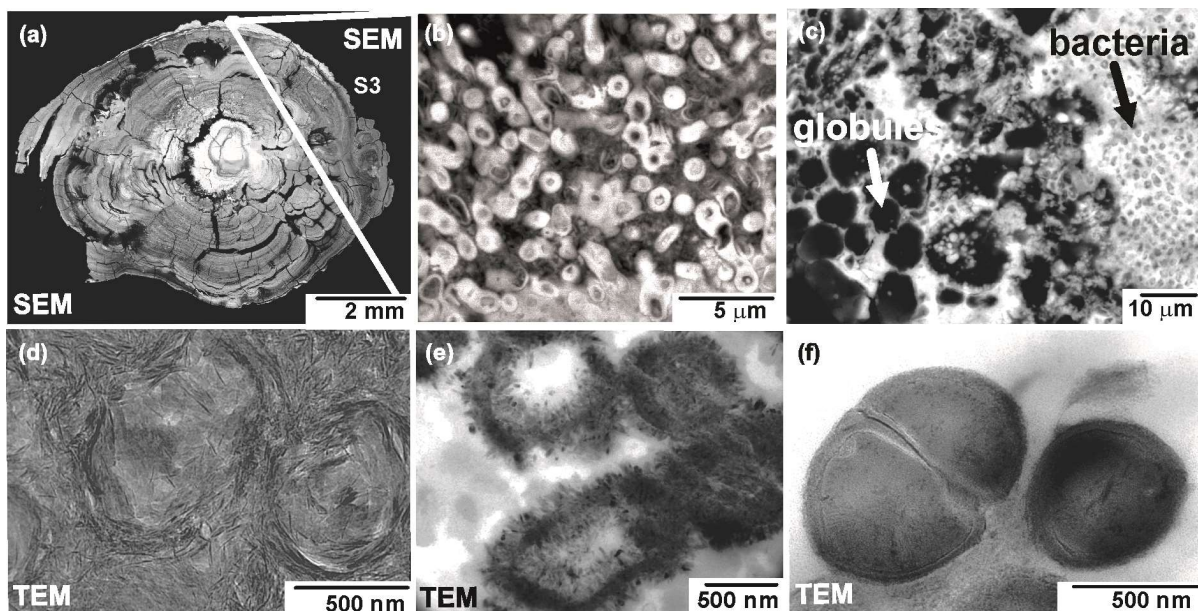


Figure 3.10 – (a) Median section of S_3 . (b) Bacterial colony found at the periphery of S_3 . (c) Comparison of globular structures and bacterial colony. (d) Bacteria mineralized with filamentary crystals. (e) Bacteria mineralized with needlelike crystals. (f) Non-mineralized bacteria undergoing cell division.

3.2. Discussion

Non-destructive μ CT imaging can be used to discriminate the major core of each sialolith from structures formed during the subsequent growth stages. Hence, the internal 3-D configuration inferred from the tomographic data enables to roughly establish a chronological

order for the development of the sialolith. Interpretation of the reconstructed μ CT images benefits from the complementary observations carried out at higher resolution by electron microscopy. In turn, direct observation of a sialolith section by SEM may result in misleading interpretations. For instance, if in the sectioning step of the sample preparation for SEM observation (see Figure 3.1), the weakly mineralized core of S₁₂ or S₁₃ were to be just missed, one would erroneously infer a highly mineralized center, and the opposite situation would occur for S₂₄ or S₂₅ (Figure 3.1). SEM coupled with focused ion beam and TEM tilting sequences can be used for high-resolution tomography. However, these techniques are unsuited for large specimens such as sialoliths. The present approach, relying on μ CT to obtain 3-D information from relatively large samples and on SEM and TEM to scrutinize local details at finer scales, can be effectively used to characterize the structure of sialoliths.

The existence of one major, or primary, core, as observed for S₁₂, S₁₃, S₁₅, S₁₇, S₁₈, S₁₉, S₂₁, S₂₂, S₂₄, S₂₅ in Figure 3.1, suggests a nucleation stage after which growth occurs through a different mechanism. The highly mineralized cores of S₂₁, S₂₂, S₂₄ and S₂₅ are compatible with a nucleation based on accretion of calcified sialomicroliths [4, 5], while the weakly mineralized cores of S₁₂, S₁₃ or S₁₅ are compatible with a nucleation process based on the accretion of degenerated and condensed stagnant secretory material poor in calcium [4, 5] or foreign bodies in the ducts, such as food debris [6]. Both highly mineralized and organic cores have been previously reported [1, 7-10], attesting for the representativeness of the configurations shown in Figure 3.1.

The contrast observed in the μ CT reconstructions does not increase monotonically from the periphery to the central regions (see the attenuation profiles shown for S₁₂ and S₂₅ in Figure 3.1). The fact that internal regions are able to remain poorly mineralized during subsequent growth stages indicate that long-range inward diffusion of the mineralizing agents is not occurring during sialolith growth. In addition, it points to a variable supply of

crystallizing electrolytes and to a calcification process occurring essentially at the periphery of the sialoliths. Therefore, the present results do not support the hypothesis of an increasing mineralization of the organic matrix during the chronological development of sialoliths [11].

Although the specimens often exhibited more than one type of growth pattern, the characteristic types illustrated in Figure 3.2 represent an attempt to deal with the structural diversity. Concentric patterns are proposed to correspond to (quasi) steady-state growth, whereas irregular patterns may be associated with recurrent inflammation/infection episodes likely to induce growth perturbations.

The predominant growth mechanism appears to involve deposition of organic matter that is subsequently mineralized (Figure 3.3 (a) to (d)). Accretion of mineralized nodules can occur during the growth stages (Figures 3.3 (e) and (f)), although this mechanism does not play a key role. Accretion of larger structures, which would result in multiple cores, is also not prevalent. The convoluted organic layers detected at peripheral regions (Figure 3.3 (g)) are compatible with the adherence to the surface of sialoliths of a ductal metaplastic stratified squamous epithelium, which was subsequently integrated into the calcifying structure [12].

The quasi-periodic spatial distribution of crystallites observed in Figure 3.3 (a) is in agreement with a precipitation reaction where two co-precipitating inorganic electrolytes diffuse through a gel to form the so-called Liesegang rings [13, 14]. Ostwald proposed a generally accepted mechanism for Liesegang ring formation [15]: an initial supersaturation of the diffusive species is followed, at a given threshold, by heavy precipitation of salt particles that deplete the surroundings of the diffusive species, lowering the saturation level of the gel such that the nucleation rate drops to produce an ensuing low mineralization band; the process resumes once the supersaturation threshold is exceeded in the subsequent layer of the gel. The rhythmic banding of precipitates in sialoliths (Figures 3.3 (a) and 3.6 (a) and 3.7 (f)) is proposed to originate from (continuous or intermittent) deposition of an organic gel in

which successive precipitation events occur due to Liesegang-Ostwald compositional gradients. Often, only one type of crystal morphology was found in any given region (see magnified inset of Figure 3.6 (a)), as a reflection of the local chemistry.

The powder and single crystal electron diffraction patterns demonstrated that the Ca- and P-based electrolytes tended to crystallize in a hexagonal crystal structure close to hydroxyapatite (Figure 3.6). The presence of Mg in the mineralized regions (Figure 3.4 (g)) suggests the formation of whitlockite [16], although the phase was not in electron diffraction experiments.

The globular structures originate from a surface tension effect between two immiscible organic fluids (Figure 3.7 (a)). Crystallization typically begun around the globules with filamentary hydroxyapatite crystals (see arrows in Figure 3.7 (a)). These regions seem to contain powerful agents inducing calcification, which existed in lower concentration inside the globules. Hydrophilic and hydrophobic lipids are major constituents of sialoliths [17-19] and a lipidic nature has been suggested for the globular structures [20]. The globules consistently showed higher sulfur content (Figure 3.4), which is compatible with the presence of sulfoglycolipids [19] and acidic highly sulfated mucins, secreted by the submandibular [4, 5] and parotid glands [21].

The activity of bacterial colonies has been previously associated with the presence of sulfur in sialoliths [22]. Bacterial infection may occur as a consequence of stagnant conditions in obstructed ducts [23] and genetic analysis has been used to identify several species of bacteria in sialoliths [24]. The present observations show that bacteria affect the local growth of the mineral crystals: filamentary crystals tended to wind around cell membranes (Figure 3.10 (d)), while platelets grew perpendicularly to the membranes (Figure 3.10 (e)).

The growth of viscous fingers represents a type of hydrodynamic instability that occurs upon injection of a low-viscosity fluid into a high-viscosity one [25]. Fractal patterns form when the interfacial energy between the two fluids is low, with successive branching limited by the capillarity forces. These conditions are fulfilled when injecting a solvent into a concentrated suspension of colloidal particles in the same solvent, such as when water flows through clay slurries [25] or, as in the present case, when a less mineralized organic gel flows through a mineralized zone (Figure 3.8 (c)). An increase in internal pressure is required for the injection/extrusion of the organic gel through the mineralized walls (Figure 3.8 (d)). The observation that the fingerlike globules were usually less mineralized than the parent globule (Figure 3.8 (b) and (d)) suggests that crystal formation may be responsible for the pressure increase. Fractal analysis offers a deeper insight into the mechanisms governing this type of patterning process [26] and theoretical models describing viscous fingering processes have shown that fractal dimensions of 1.8 correspond to viscosity ratios above 10 [27, 28], defining fundamental rheological characteristics of the system.

3.3. Summary

X-ray tomography data showed that sialoliths frequently exhibit a major core with either higher or lower mineralization than the surrounding material. The growth patterns have been classified into four types depending on their organization and mineralization level. Electron microscopy observations revealed that at fine scales the growth processes result in alternating mineralized/organic bands and in globular dispersions of organic matter in highly mineralized regions. High sulfur content indicates that the organic matter in the sialoliths corresponds essentially to degenerated and condensed secretory material. The precipitation patterns observed in banded structures are compatible with a Liesegang-Ostwald phenomenon, while globular structures result from a viscous fingering process where a

low-viscosity organic gel is filtered/injected through higher-viscosity mineralized regions. These globular structures are self-similar and their fractal dimension indicates that the low mineralized regions have low viscosity.

3.4. References

1. Sakae T, *et al.*, Mode of occurrence of brushite and whitlockite in a sialolith, *J Dent Res*, 60:842-844, 1981
2. Yamamoto H, *et al.*, Scanning electron microscopic and X-ray microdiffractometric studies on sialolith-crystals in human submandibular glands, *Acta Pathol Jpn*, 34:47-53, 1984
3. Grases F, *et al.*, Sialolithiasis: mechanism of calculi formation and etiologic factors, *Clin Chim Acta*, 334:131-136, 2003
4. Harrison JD, Natural history of chronic sialadenitis and sialolithiasis, In *Modern Management Preserving the Salivary Glands*, Nahlieli O, McGurk M, Iro H, Zenk J (eds), Herzeliya, Isradon Publishing House, pp.93–135, 2007
5. Harrison JD, Causes, natural history, and incidence of salivary stones and obstructions, *Otolaryngol Clin North Am*, 42:927-947, 2009
6. Marchal F, *et al.*, Retrograde theory in sialolithiasis formation, *Arch Otolaryngol Head Neck Surg*, 127:66-68, 2001
7. Kasaboğlu O, *et al.*, Micromorphology of sialoliths in submandibular salivary gland: A scanning electron microscope and X-ray diffraction analysis, *J Oral Maxillofac Surg*, 62:1253-1258, 2004
8. Giray CB, *et al.*, Sialolith characterization by scanning electron microscopy and X-ray photoelectron spectroscopy, *Scanning*, 29:206-210, 2007
9. Sabot JF, *et al.*, Analytical investigation of salivary calculi, by mid-infrared spectroscopy, *Analyst*, 137:2095-2100, 2012

10. Szalma J, *et al.*, Proteomic and scanning electron microscopic analysis of submandibular sialoliths, *Clin Oral Investig*, 17:1709-1717, 2013
11. Zenk J, *et al.*, Extracorporeal shock wave lithotripsy of submandibular stones: evaluation after 10 years, *Ann Otol Rhinol Laryngol*, 113:378-383, 2004
12. Isacson G, Hammarstrom L, An enzyme histochemical study of human salivary duct calculi, *J Oral Pathol*, 12:217-222, 1983
13. Liesegang RE, Ueber einige Eigenschaften von Gallerten, *Naturwiss Wochenschr*, 11:353-362, 1896
14. Henisch HK, Liesegang ring formation in gels, *J Cryst Growth*, 76:279-289, 1986
15. Ostwald W, Zur Theorie der Liesegang'schen Ringe, *Kolloid Z*, 36:380-390, 1925
16. Gopal R, *et al.*, Crystal Structure of Synthetic Mg-Whitlockite, $\text{Ca}_{18}\text{Mg}_2\text{H}_2(\text{PO}_4)_{14}$, *Can J Chem*, 52:1155-1164, 1974
17. Anneroth G, *et al.*, The relation of lipids to the mineral components in salivary calculi, *J Oral Pathol*, 6:373-381, 1977
18. Boskey AL, *et al.*, Lipids associated with mineralization of human submandibular gland sialoliths, *Arch Oral Biol*, 26:779-785, 1981
19. Slomiany BL, *et al.*, Lipid composition of the matrix of human submandibular salivary gland stones, *Arch Oral Biol*, 27:673-677, 1982
20. Tanaka N, *et al.*, Ultrastructural analysis of salivary calculus in combination with X-ray microanalysis, *Med Electron Microsc*, 36:120-126, 2003
21. Kutta H, *et al.*, Antimicrobial defence mechanisms of the human parotid duct, *J Anat*, 208:609-619, 2006
22. Washio J, *et al.*, Hydrogen sulfide-producing bacteria in tongue biofilm and their relationship with oral malodour, *J Med Microbiol*, 54:889-895, 2005
23. Lee LT, Wong YK, Pathogenesis and diverse histologic findings of sialolithiasis in minor salivary glands, *J Oral Maxillofac Surg*, 68:465-470, 2010

24. Teymoortash A, *et al.*, Bacteria and pathogenesis of human salivary calculus, *Acta Otolaryngol*, 122:210-214, 2002
25. Van Damme H, *et al.*, Fractal viscous fingering in clay slurries, *Nature*, 320:731-733, 1986
26. Sinha S, Tarafdar S, Viscous Fingering Patterns and Evolution of Their Fractal Dimension, *Ind Eng Chem Res*, 48:8837-8841, 2009
27. Zhang J-h, Liu Z-h, Study of the relationship between fractal dimension and viscosity ratio for viscous fingering with a modified DLA model, *J Pet Sci Eng*, 21:123-128, 1998
28. Stevenson K, *et al.*, 2-D network model simulations of miscible two-phase flow displacements in porous media: Effects of heterogeneity and viscosity, *Physica A*, 367:7-24, 2006

Chapter 4. X-ray computed tomography of sialoliths

Overview

In the present chapter, X-ray computed microtomography (μ CT), combined with atomic emission spectroscopy (AES), Fourier transform infrared spectroscopy (FTIR), X-ray diffraction (XRD), scanning electron microscopy (SEM) and transmission electron microscopy (TEM) are used to investigate the composition and mineralization degree of submandibular sialoliths. The relations between calculi mineralization/density and average μ CT attenuation are defined, and the method developed is validated for helical computed tomography (HCT), following a correlative strategy between in vivo and ex vivo scans.

4.1. Results

4.1.1. Chemical and structural characterization

Characteristic diffractograms of sialoliths are shown in Figure 4.1 ((a) and (b)) with simulations for hydroxyapatite and whitlockite (in (c) and (d), respectively). XRD analysis of 22 specimens revealed that the mineral components crystallized essentially as HA. Nevertheless, Whi was present in 52 % of the specimens investigated by XRD with an average volume proportion of HA:Whi = 89:11. No other mineral phases previously reported for sialoliths (such as brushite and octacalcium [1, 2]) have been detected. The wide peaks suggest nanometric crystals and/or some degree of structural disorder. In addition, the average unit cell dimensions ($a_{\text{HA}} = 9.41 \pm 0.02$ and $c_{\text{HA}} = 6.84 \pm 0.02$ and $a_{\text{Whi}} = 10.35 \pm 0.01$, $c_{\text{Whi}} = 37.06 \pm 0.08$) showed deviations from the lattice parameters used in the simulations ($a_{\text{HA}} = 9.42$ and $c_{\text{HA}} = 6.89$ [3] and $a_{\text{Whi}} = 10.35$, $c_{\text{Whi}} = 37.08$ [4]). Nevertheless, compliance to stoichiometry could not be easily accessed due to the known low sensitivity of powder XRD for group substitutions and compositional disorder in HA [5].

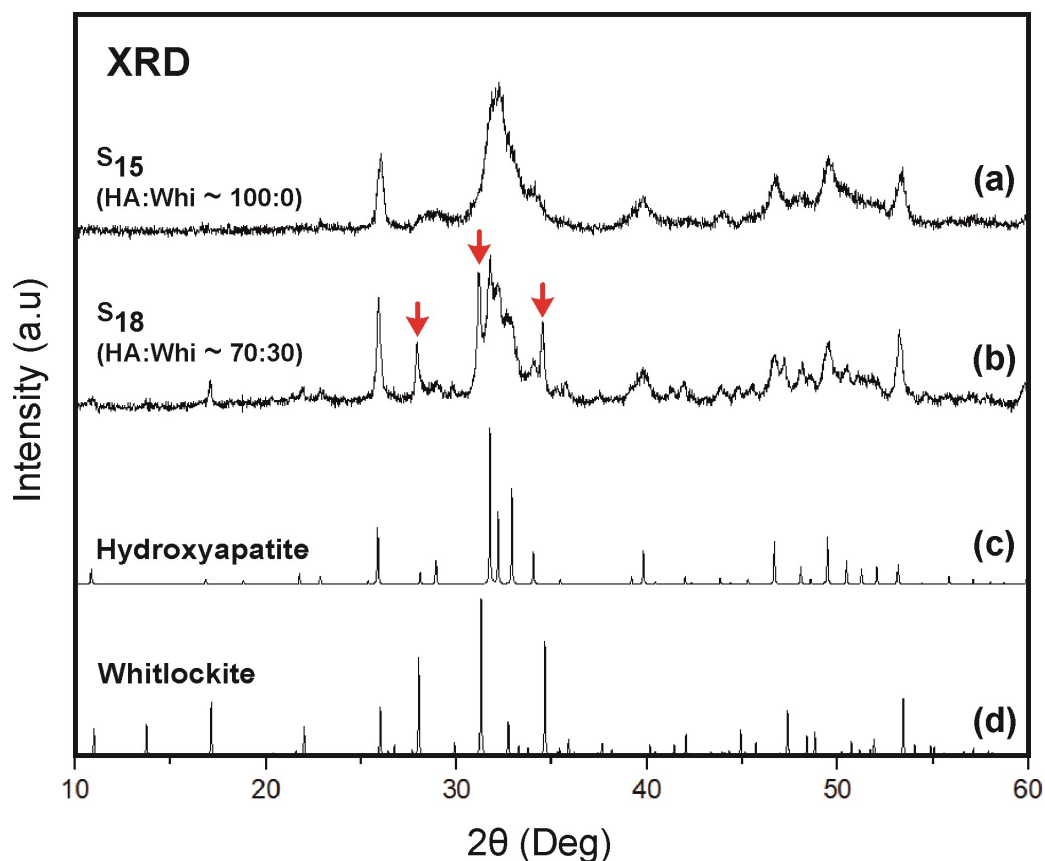


Figure 4.1 - XRD patterns of prototypical sialoliths with simulated diffractograms for HA [3] and Whi [4]. The red arrows indicate major Whi peaks. HA and Whi volume fractions are indicated as a ratio above each experimental diffractogram.

Figure 4.2 presents the FTIR spectrum of a typical sialolith along with spectra of an organic region obtained from a large sialolith, saliva and synthetic hydroxyapatite. The bands at 1653 cm^{-1} , 1551 cm^{-1} and 1239 cm^{-1} associated, respectively, with vibrations of amide I (stretching vibration of the carbonyl group), amide II (stretching of C-N and bending of H-N) and amide III (stretching of C-N and bending of N-H), indicate the presence of proteins [6], while the bands at 2927 cm^{-1} (stretching of C-H) and 1452 cm^{-1} (bending of alkyl groups CH_2 and CH_3) point to lipidic biomolecules [7]. The broadband at 3440 cm^{-1} is probably associated with water molecules remaining in the organic matter after the drying process [8]. These results show that the organic matter in sialoliths exhibits a FTIR signature remarkably similar to that of saliva, except for the absence of the bands at 960 cm^{-1} and 1406 cm^{-1} .

corresponding to, respectively phosphate and carbonate [9], which precipitate as carbonated calcium phosphate in mineralized regions. On the other hand, the mineral matter presents significant differences from synthetic hydroxyapatite as shown by the absence of the sharp hydroxyl bands at 631 cm^{-1} and 3572 cm^{-1} (present in synthetic HA) and presence of a carbonate band at 875 cm^{-1} (absent in synthetic HA) [8-10]. Direct substitution of hydroxyl groups by carbonate groups in the HA structure (type-A carbonation) is known to require high-temperature processing conditions [11, 12]. In biological apatites, the absence of hydroxyl groups is typically compensated by Ca^{2+} deficiency [5, 13], while CO_3^{2-} substitutes PO_4^{3-} groups (type-B carbonation) [11, 14, 15] according to $\text{Ca}_{10-x}(\text{PO}_4)_{6-x}(\text{CO}_3)_y(\text{HPO}_4)_{x-y}(\text{OH})_{2-x}$ [11].

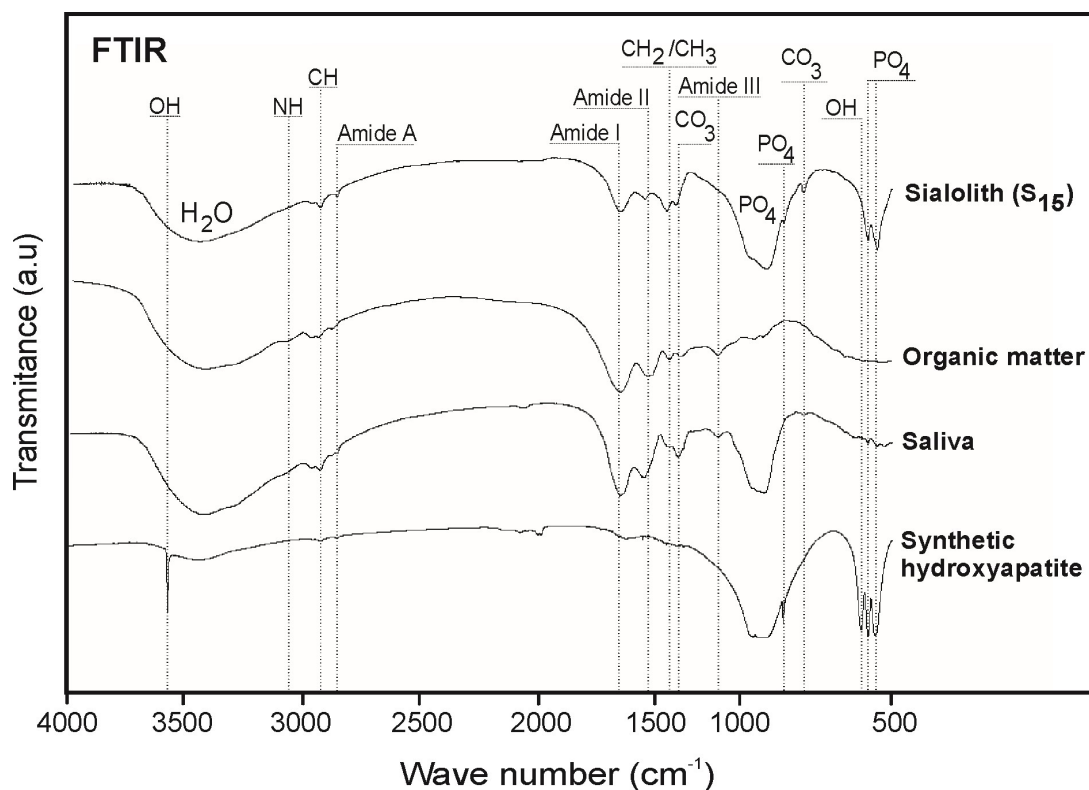


Figure 4.2 – FTIR spectra of a sialolith, a large organic region in a sialolith, saliva and hydroxyapatite. Characteristic bands [6-10] are indicated.

Additional information on the chemical substitutions was obtained from the Ca, Mg and P concentrations determined by AES for a set of specimens. Average concentrations are presented in Table 4.1 in terms of hydrated and dry sialolith masses. In Figure 4.3 (a), the volume fraction of Whi in the crystalline matter, $f_{whi}^{XRD} = \frac{V_{whi}^{XRD}}{V_{HA}^{XRD} + V_{whi}^{XRD}}$, is plotted against the Mg concentration for each sialolith. A reference line shows the expected Whi fraction in HA:Whi mixtures for increasing Mg concentration assuming stoichiometric compositions (i.e., $Ca_{10-x}(PO_4)_{6-x}(CO_3)_y(HPO_4)_{x-y}OH_{2-x}$ for HA [11] and $Ca_{18}Mg_2H_2(PO_4)_{14}$ for Whi [4]). These results support the hypothesis that Whi crystallizing in biologic environments is of the Mg-substituted type [16, 17]. However, the experimental deviations relative to the reference line show that the amount of Mg is sub-stoichiometric. In addition, since Mg is residual in the organic matter [18, 19], the presence of Mg in specimens with $f_{whi}^{XRD} = 0$ demonstrates that this element also substitutes Ca in HA. In consequence, the concentration of Mg in sialoliths is not a suitable proxy for Whi content.

Table 4.1 – Average concentrations determined by AES for 40 sialoliths in hydrated and dry states.

	Hydrated state ($\mu \pm \sigma$)	Dry state ($\mu \pm \sigma$)
Ca (wt. %)	19.2 \pm 5.0	25.8 \pm 6.2
Mg (wt. %)	0.2 \pm 0.1	0.3 \pm 0.1
P (wt. %)	10.0 \pm 2.7	13.4 \pm 3.2
Ca/P (wt. %)	1.9 \pm 0.2	

Figure 4.3 (b) shows the P vs Ca+Mg concentrations for each sialolith. Nominal points for HA and Whi are included (open circles) together with proportional guidelines (plotted assuming absence of Ca, Mg and P in the organic matter). The slightly excessive Ca+Mg concentration points to the presence of these elements in the organic matter, where up to ~2.5 at. % Ca was previously detected [19, 20].

The average density of sialoliths in hydrated state was $1.8 \pm 0.2 \text{ g/cm}^3$. The coloured points in Figure 4.3 (c) represent the density of each specimen ($\rho_{\text{sialolith}}$) as a function of the mineral volume fraction, $f_{\text{mineral}} = \frac{V_{\text{HA}} + V_{\text{Whi}}}{V_{\text{specimen}}}$, where V is volume and $V_{\text{specimen}} = V_{\text{Ha}} + V_{\text{Whi}} + V_{\text{organic}}$. The values of f_{mineral} were estimated from the Ca+Mg concentration assuming stoichiometry and absence of these elements in the organic fraction. Nominal density values for HA and Whi are included for comparison at $f_{\text{mineral}} = 1$. A rule of mixtures was fitted to the points, with a fixed node at $f_{\text{mineral}} = 1$ for which an average HA:Whi = 89:11 proportion was assumed. The fitting yielded $1.2 \pm 0.3 \text{ g/cm}^3$ for the density of the organic matter (Figure 4.3 (c)).

The lines in Figure 4.3 (d) represent the expected variations of f_{mineral} and mineral density, $\rho_{\text{mineral}} = \frac{m_{\text{HA}} + m_{\text{Whi}}}{V_{\text{specimen}}}$, where m is mass, as a function of Ca+Mg concentration.

These lines were determined assuming:

1. An average proportion of HA:Whi = 89:11 for the mineral component.
2. Absence of Mg in HA and stoichiometric Mg in Whi ($\text{Ca}_{18}\text{Mg}_2\text{H}_2(\text{PO}_4)_{14}$ [3, 4]) given the lack of a suitable model to describe the partition of Mg between the two mineral phases (see Figure 4.3 (a)).
3. HA substituted according to $\text{Ca}_{10-x}(\text{PO}_4)_{6-x}(\text{CO}_3)_y(\text{HPO}_4)_{x-y}\text{OH}_{2-x}$ [11], where the absence of hydroxyl groups (x) is balanced with Ca^{2+} deficiency and phosphate protonation, while hydrophosphate groups are partially substituted (y) by carbonate ones. A negligible

presence of hydroxyl groups was assumed as inferred from the FTIR data, i.e., $x \approx 2$, whereas the substitution of hydrophosphate by carbonate was presumed to represent 5 % of the total mass, i.e., $y = 0.7$, based on the mineralization behaviour of dentine, which also shows low concentration of OH^- and high fraction of organic matter (~20 wt. %) [21, 22].

4. Nominal densities for stoichiometric Whi ($\rho_{\text{Whi}} = 3.0 \text{ g/cm}^3$ [4]) and substituted HA ($\rho_{\text{HA}} = 2.7 \text{ g/cm}^3$ [3, 11]).
5. Organic matter density, ρ_{organic} , of $1.2 \pm 0.3 \text{ g/cm}^3$, as determined from the rule of mixtures fitted to the experimental points in Figure 4.3 (c).

The expected non-linear behaviour of f_{mineral} (and ρ_{mineral}) vs Ca+Mg concentration (Figure 4.3 (d)) results from a greater variation in mineral volume (and mass) compared to total sialolith volume (and mass) for increasing Ca+Mg concentration, as these elements integrate predominantly the denser mineral component rather than organic matter. The points in Figure 4.3 (d) represent experimental f_{mineral} values determined for each sialolith from: Ca+Mg concentration, specimen volume (μCT data), HA:Whi volume proportion and lattice parameters (XRD data). The fair agreement with the expected behaviour indicates that the reference line(s) can be used to estimate f_{mineral} (and ρ_{mineral}) from the experimental Ca+Mg concentration. Indeed, this reasoning was employed to plot the gray points in Figure 4.3 (c), which represent the experimental density for the subset of specimens not investigated by XRD and for which f_{mineral} was estimated solely from the Ca+Mg concentration using the reference line in Figure 4.3 (d).

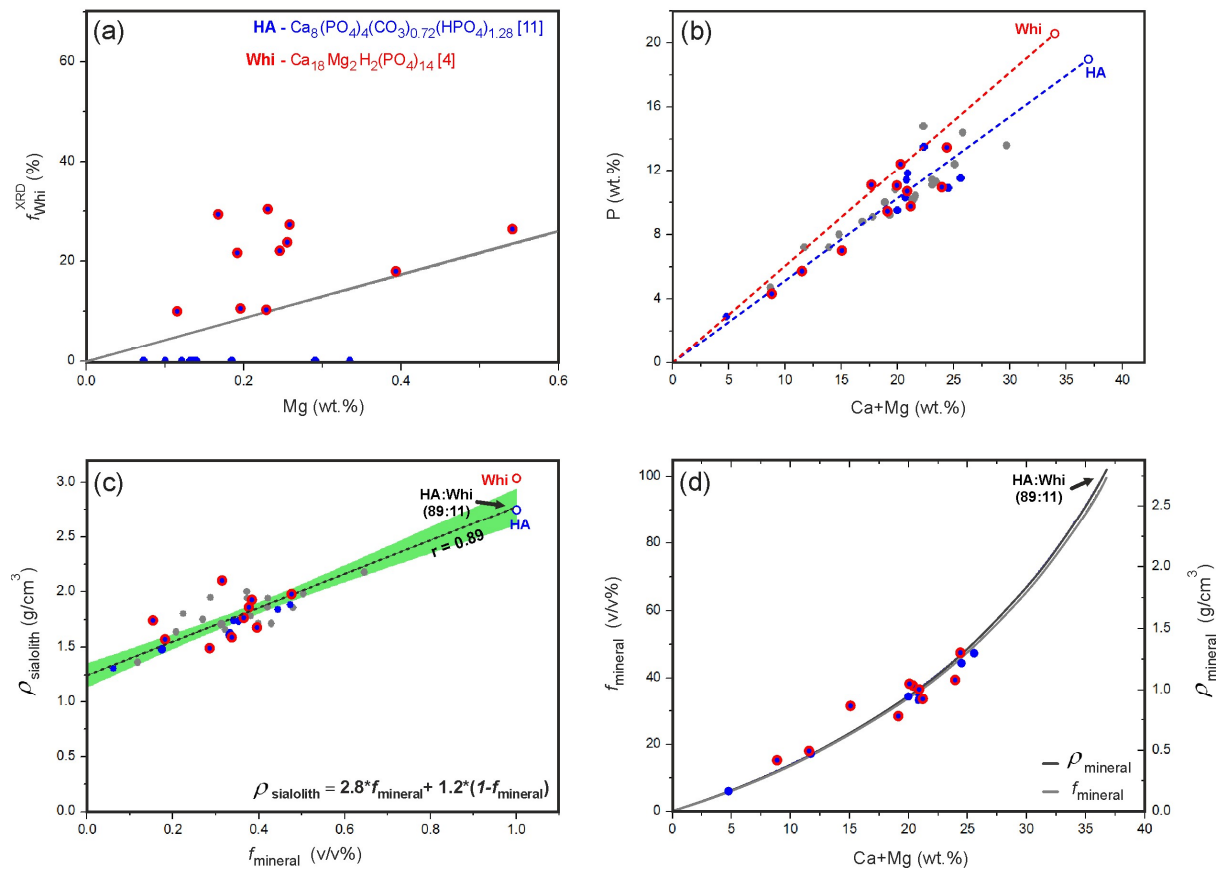


Figure 4.3 - (a) Volume fraction of Whi in HA+Whi mixtures, as determined by XRD, as a function of Mg concentration in hydrated specimens. The line represents the expected Mg variation for stoichiometric HA+Whi mixtures. HA: $\text{Ca}_{10-x}(\text{PO}_4)_6-x(\text{CO}_3)_y(\text{HPO}_4)_{x-y}\text{OH}_{2-2x}$, with $x = 2$ and $y = 0.72$ and Whi: $\text{Ca}_{18}\text{Mg}_2(\text{PO}_4)_{14}$. (b) P concentration vs Ca+Mg concentration with nominal positions for stoichiometric HA and Whi (open circles) and proportional guidelines. (c) Measured sialolith density vs mineral volume fraction estimated from the experimental Ca+Mg concentration (see (d)). The green region represents the 95 % confidence interval of the linear regression. (d) Mineral volume fraction (line and points) and mineral density (only line for clarity) estimated from the measured density and vs Ca+Mg concentration. Colour code for the solid points in all plots: blue – solely HA and blue/red – mixture of HA and Whi as inferred from XRD, gray – undetermined mineral HA vs Whi proportion. The lines in (a), (b) and (d) represent expected variations, while in (c) a rule of mixtures (equation in legend) was fitted to the blue/red points.

Table 4.2 lists the weight and volume fractions of the mineral and organic components in sialoliths estimated from the experimental mass, volume and Ca+Mg concentration (see Figure 4.3 (d)). The fraction of hydration water was inferred from the loss of mass during the drying process. Since dehydration occurs essentially in the organic matter [8], the hydration water was assumed to be fully integrated in the organic fraction. The mineral and organic weight fractions

in dry state were inferred from the hydrated values by subtraction of the water fraction. These results show that the organic volume fraction is predominant (65 vol. %), whereas the mineral mass accounts for most of the specimens' hydrated and dry weights (respectively, 53 and 72 wt. %).

Table 4.2 – Mineralized and organic fractions (in weight and volume) of 33 sialoliths in dry and hydrated states, calculated from Ca+Mg wt. %.

	Hydrated state ($\mu \pm \sigma$)	Dry state* ($\mu \pm \sigma$)
Mineralized fraction (m/m)	0.53 \pm 0.13	0.72 \pm 0.16
Organic fraction (m/m)	0.47 \pm 0.13	0.28 \pm 0.16
Hydration water (m/m)	0.27 \pm 0.10	-
Mineralized fraction (v/v)	0.35 \pm 0.10	-
Organic fraction (with water) (v/v)	0.65 \pm 0.10	-

* The specimens' dry volume was not measured, thus mineralized and organic volume fractions in dry conditions are not estimated.

4.1.2. Ultrastructure

The ultrastructure of the sialoliths was often threaded with globules of variable size and mineralization degree, surrounded by highly mineralized regions (Figure 4.4 (a) and (b) and [20]). The organic globules typically presented a high density of precipitate clusters at the center and a precipitate-free zone near the interface (Figure 4.4 (a) to (d)), while regions around the globules showed dense dispersions of filamentary crystals (Figure 4.4 (c) and (e)) that have been identified as HA.

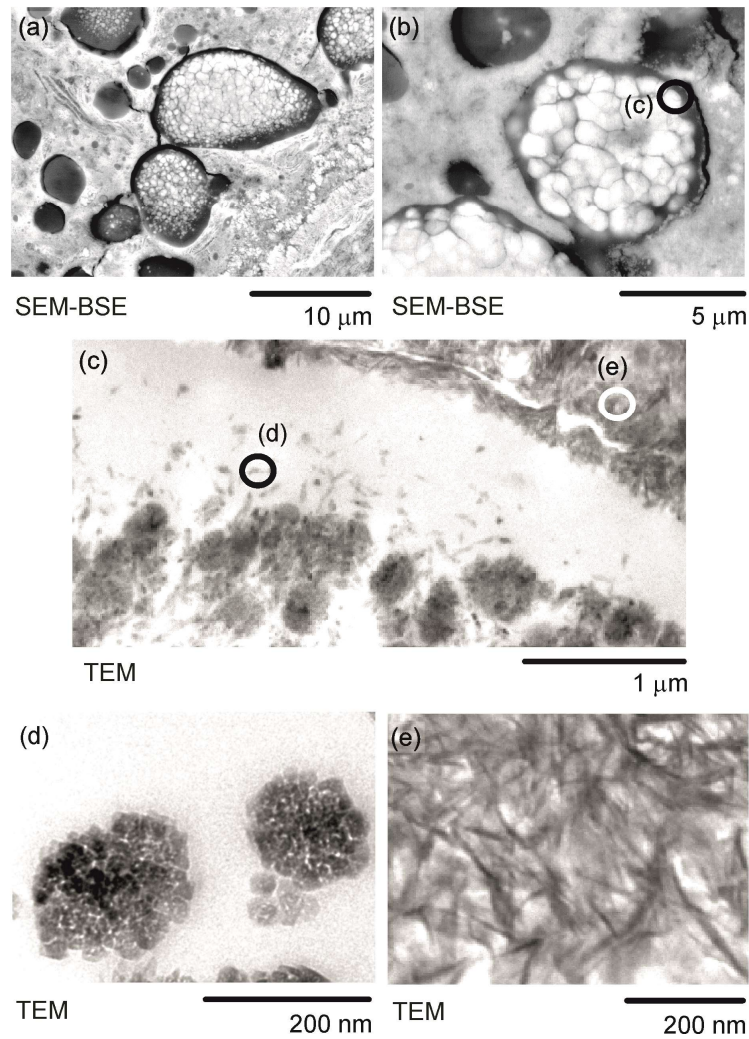


Figure 4.4 – Calcium phosphate clusters and typical hydroxyapatite crystals in sialolith ultrastructure. (a), (b) SEM (BSE) image of globules of organic matter partially mineralized. (c) TEM magnified view of interfacial region. (d) SEM (BSE) image of mineralization clusters inside a globule. (e) TEM image of hydroxyapatite crystals in a region around globules.

4.1.3. Computed microtomography

Figure 4.5 shows longitudinal μ CT sections of sialoliths. Most specimens presented a single well-defined nucleation center (e.g. S₂₈), one showed several (S₃₂) and two did not exhibit a clear nucleation center (S₃₀ and S₄₀).

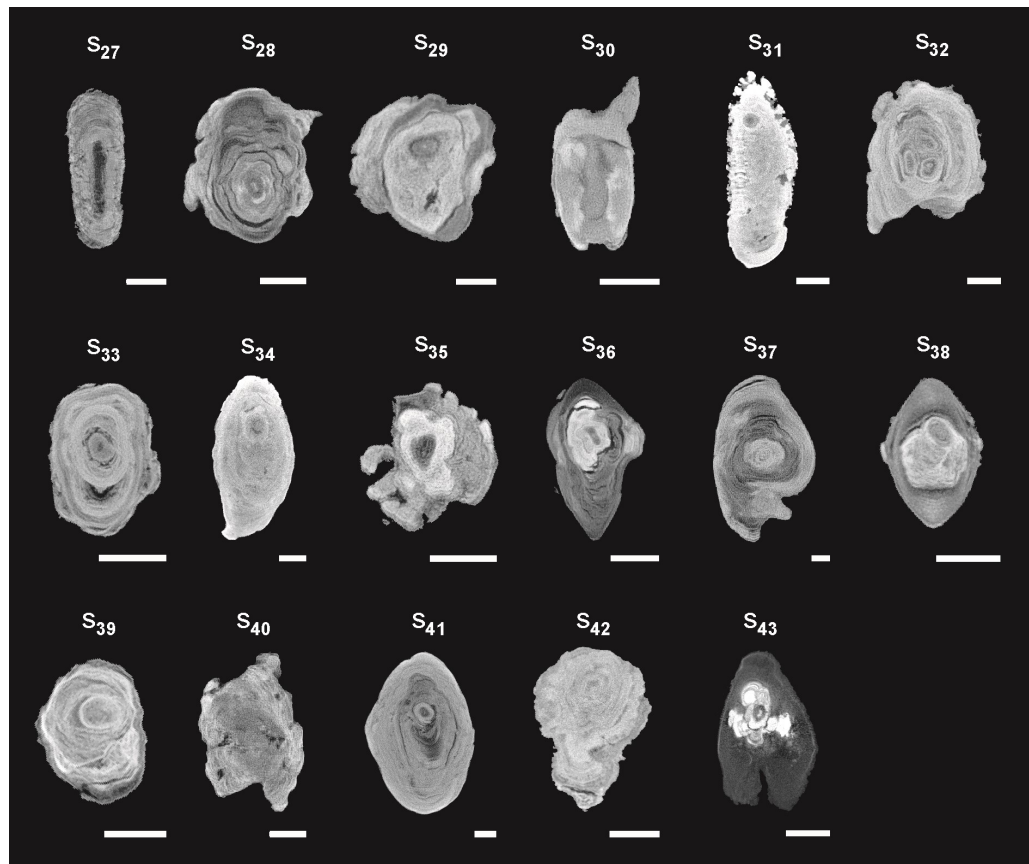


Figure 4.5 – Median longitudinal μ CT cross-sections of a subset of specimens. Brighter regions indicate higher mineralization and dark regions represent essentially organic matter. Scale bar is 2 mm

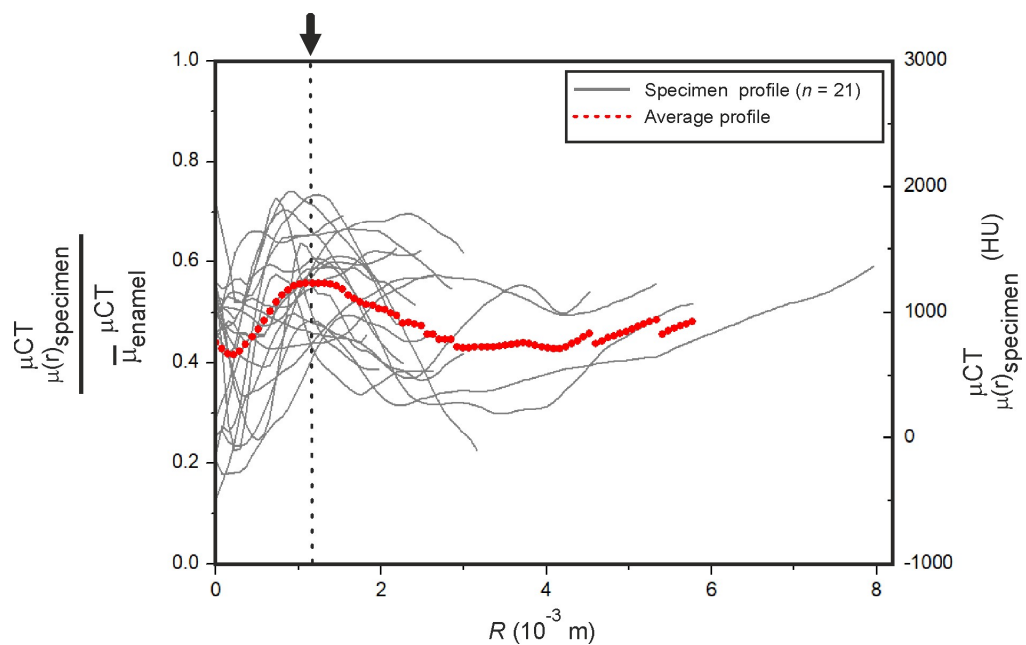


Figure 4.6 – Radial attenuation profiles of sialoliths normalized to enamel's attenuation, obtained from warped and radially integrated μ CT data. The red dotted curve represents the average profile of the studied population. The arrow indicates a maximum at $R = 1.2 \times 10^{-3}$ m.

These results demonstrate that sialoliths adopt nearly spherical (S_{41} in Figure 4.5), oval (S_{38} in Figure 4.5) or asymmetrical (S_{35} in Figure 4.5) shapes [23], while the internal structure shows growth patterns ranging from quite concentric (e.g., S_{33}) to rather irregular (e.g., S_{40}).

Figure 4.6 presents the radial attenuation profile for each sialolith (warped, 2π -integrated and normalized in terms of enamel attenuation), with dots representing the average profile for this population. The nucleation centers displayed either distinctively higher or lower mineralization (compare S_{28} with S_{33} in Figure 4.5): using an arbitrary threshold of 50 % of enamel's attenuation, 9 mineralized and 14 organic nucleation/central regions have been identified (see Figures 4.5 and 4.6). Despite the high variability in the evolution of mineralization, on average, an attenuation maximum occurs around $R \sim 1.2$ mm (arrow in Figure 4.6). These results suggest a growth law characterized by heavy mineralization around the nucleation region typically followed by less dramatic variation in mineralization at later stages (see Figures 4.5 and 4.6).

Table 4.3 presents geometrical parameters of the sialoliths. The eccentricity, i.e., the distance between the nucleation and geometrical centers (normalized to the radius), reflects the anisotropic growth from the initial nucleation center.

Table 4.3 – Geometrical parameters obtained from μ CT data from 23 sialoliths.

	Average \pm standard deviation
Volume (10^{-9} m³)	253.2 \pm 441.0
Aspect Ratio	2.4 \pm 0.7
Eccentricity	0.4 \pm 0.3
Diameter* (10^{-3} m)	5.7 \pm 2.6

*Determined from the radial profiles.

Figure 4.7 presents the average μ CT attenuation of each specimen, normalized to enamel, $\frac{\bar{\mu}^{\mu CT}_{specimen}}{\bar{\mu}^{\mu CT}_{enamel}}$, as a function of density, $\rho_{sialolith}$, and of mineral density, $\rho_{mineral}$, estimated from the Ca+Mg concentration (Figure 4.3 (d)). For comparison, the nominal density of enamel (~ 2.96 g/cm³ [24]), renal calculi [25], living tissues [24], water and air have been added to Figure 4.7 (a).

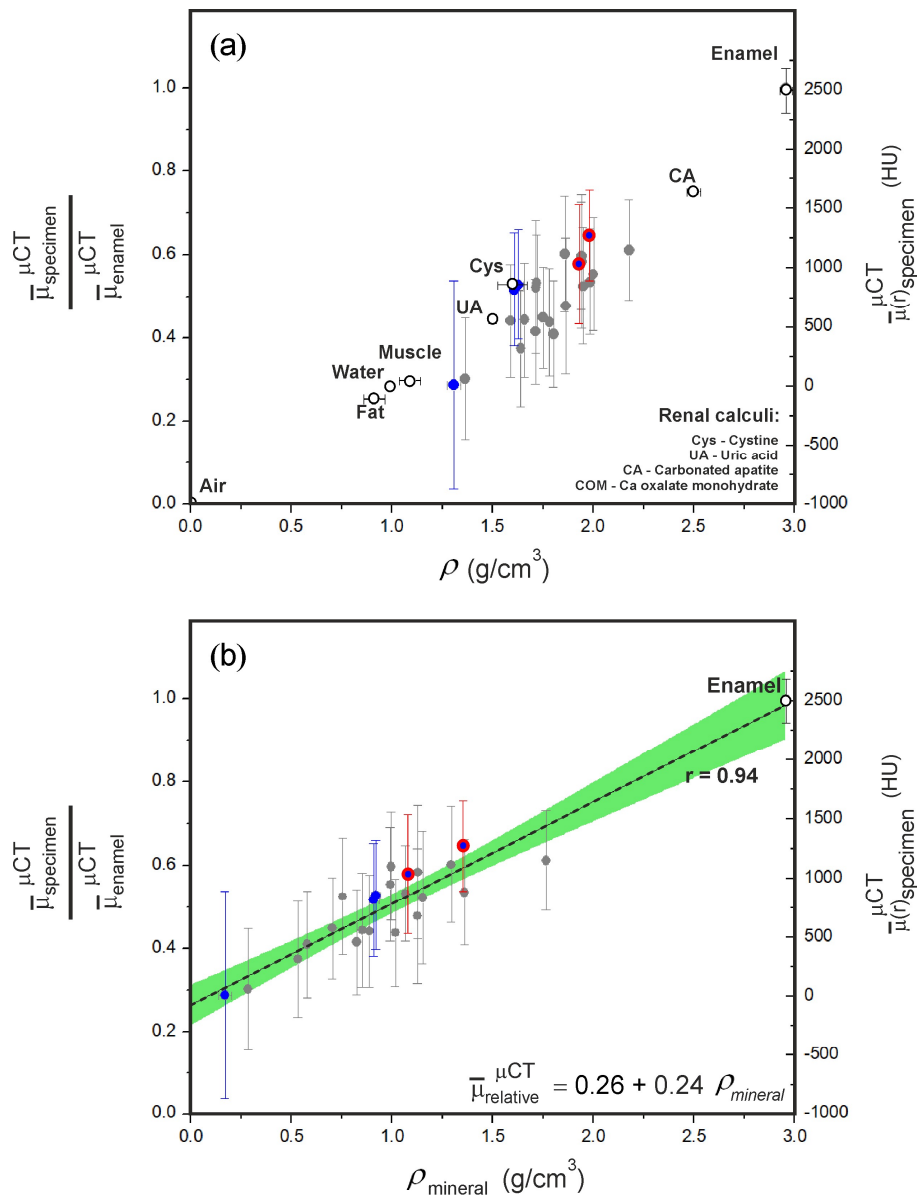


Figure 4.7 – (a) Attenuation as a function of density. (b) Attenuation as a function of mineral density. Blue – solely HA and blue/red – mixture of HA and Whi as inferred from XRD, gray – undetermined mineral proportion, open circles – literature values [26-28]. The error bars correspond to the standard deviation of the attenuation distribution in each specimen and the green region corresponds to the 95 % confidence interval of the linear regression.

The dashed line in Figure 4.7 (b) is a linear fitting to the experimental points, with the intercept at ~ 0.25 representing the attenuation of the organic matter ($\rho_{\text{mineral}} = 0$). The error bars correspond to the standard deviation of the attenuation distribution, which was largest for the most organic specimen (S₄₃ in Figure 4.5).

4.1.4. Helical computed tomography

Differences in volume and relative attenuation between HCT (Light Speed GE VCT) and μ CT (SkyScan 1172) data from the same specimens are plotted as a function of specimen average radius in Figure 4.8 (a). Relative differences in attenuation between HCT and μ CT measurements are also shown in Figure 4.8 (b) as a function of the ratios between (i) specimen radius and HCT in-plane resolution, and (ii) specimen radius and HCT z-axis resolution. Orthodontic wax and tooth enamel were employed as phantoms to calibrate the offset and gain of the HCT datasets in Figure 4.8 (a), whereas orthodontic wax and a specimen, S_{44a}, were employed to calibrate the data in Figure 4.8 (b). The larger dimensions of S_{44a}, with $\bar{R} = 6.8 \times 10^{-3}$ m, compared to enamel, with $\bar{R} = 2.1 \times 10^{-3}$ m, make S_{44a} phantom less affected by volume averaging [29]. The phantoms' attenuation was adjusted to, respectively, 0 % and 40 % of the bit resolution. In Figure 4.8, circles represent *ex vivo* and stars represent *in vivo* data. *In vivo* data were processed using the gain and offset established for *ex vivo* HCT data using the same instrument. The background attenuation in *in vivo* and *ex vivo* was $\frac{\bar{\mu}_{\text{agar}}^{\text{HCT}}}{\bar{\mu}_{\text{enamel}}^{\mu\text{CT}}} = 0.04 \pm 0.004$ and $\frac{\bar{\mu}_{\text{tissue}}^{\text{HCT}}}{\bar{\mu}_{\text{enamel}}^{\mu\text{CT}}} = 0.09 \pm 0.01$, respectively. Figure 4.9 shows cross-sections of the same specimens obtained by *in vivo* HCT, *ex vivo* HCT and *ex vivo* μ CT.

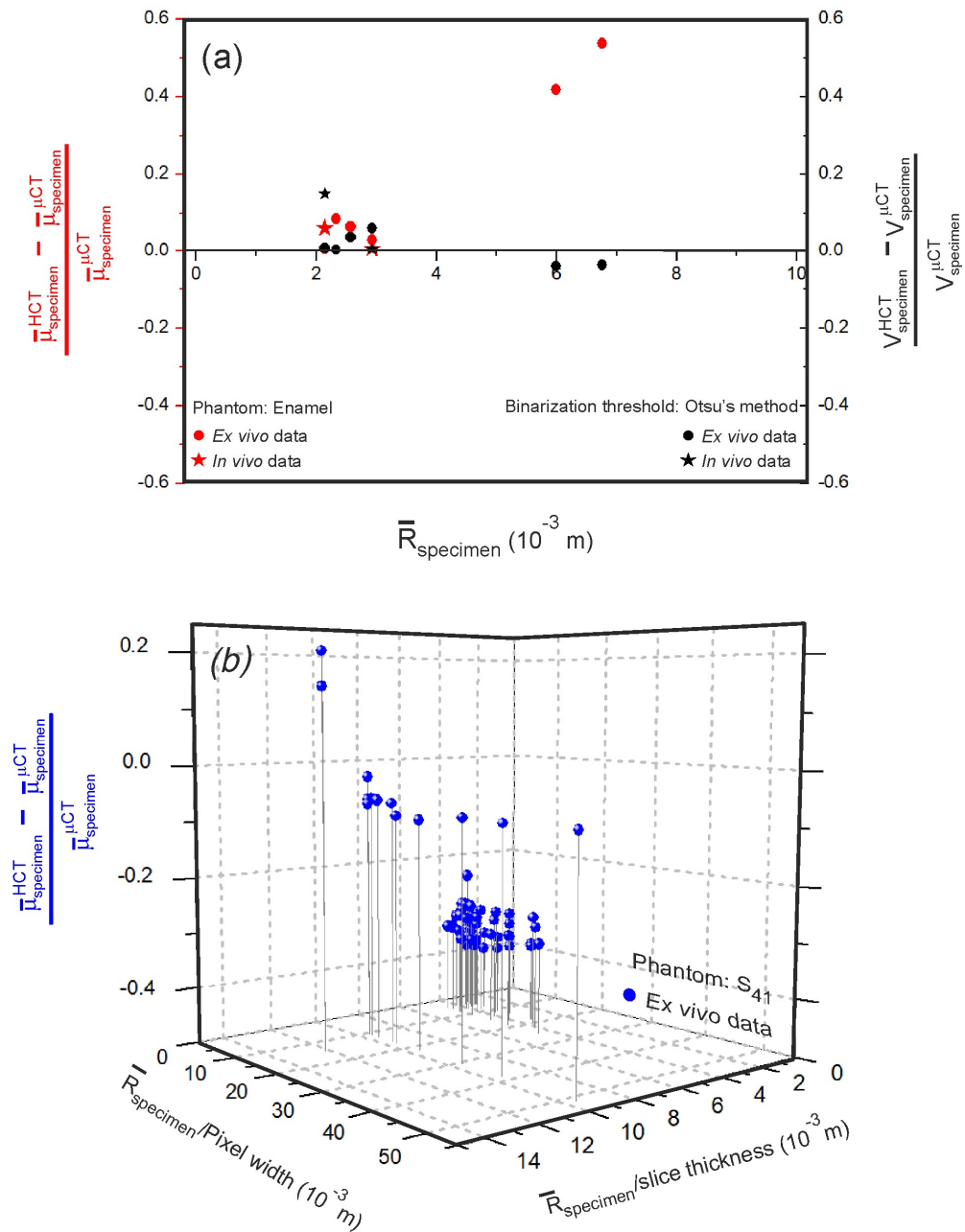


Figure 4.8 – (a) Deviations of volume and attenuation between HCT and μ CT data as a function of specimen average radius. The \bullet and \star data points correspond, respectively, to *ex vivo* and *in vivo* acquisitions performed using the Light Speed GE VCT instrument. (b) Deviation of HCT attenuation relative to the μ CT data as a function of the ratio between specimen radius and in-plane HCT resolution (0.19-0.76) and of the ratio between specimen radius and HCT collimation width (0.63).

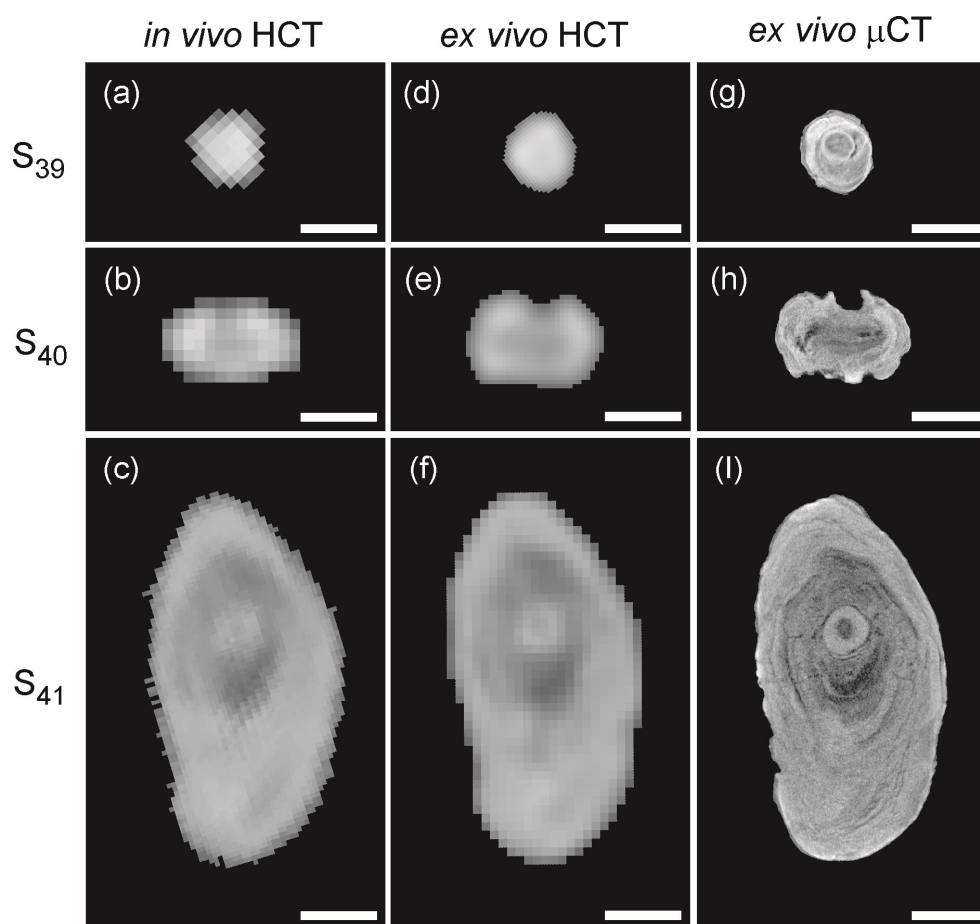


Figure 4.9 - Comparison between μ CT and HCT sections of three specimens obtained *in vivo* and *ex vivo*: (a), (b), (d), (e), (f) Light Speed GE VCT, (c) Philips Brilliance 16 and (g), (h), (i) SkyScan 1172. Spatial resolution of (a) in plane: 0.56 mm and z-axis: 0.63 mm, (b) in-plane: 0.54 mm and z-axis: 0.63 mm. (c) in-plane: 0.28 mm and z-axis: 0.75 mm. (d) and (e) in-plane: 0.19 mm and z-axis: 0.19 mm. (f) in-plane: 0.51 mm and z-axis: 0.51 mm. (g) and (h) voxel size: 0.01 mm. (i) voxel size: 0.02 mm. Scale bar is 4 mm

4.2. Discussion

The major mineral component in the sialoliths is Mg-substituted, Ca-deficient, type-B carbonated hydroxyapatite, often mixed with sub-stoichiometric Mg-whitlockite (Figure 4.1 and Figure 4.3). The chemical substitutions found are common and have been shown to be synergistic in apatites [15, 16].

The organic fraction in sialoliths is composed by protein and lipidic biomolecules as shown by the characteristic FTIR bands of amide and alkyl functional groups [7],

respectively (Figure 4.2). Mucins [10], collagen [8], glycolipids and several phospholipids [30-32] have been previously identified in sialoliths, as well as calcium-binding glycoproteins [33-35], that may be responsible for the presence of calcium in the organic matter of sialoliths (Figure 4.3 (b)). The similarity between the FTIR signatures demonstrates that the organic matter originates from saliva (Figure 4.2) [36, 37]. Nevertheless, contributions from the oral mucosa tissue and bacterial debris have been also reported [30, 38, 39].

A precipitation mechanism involving a transient phase of amorphous calcium phosphate (ACP) has been proposed for biological calcifications [40] and *in vitro* synthesis of HA from supersaturated aqueous solutions [41]. Clusters which may initially have been ACP [42] were present in the ultrastructure of sialoliths, predominantly inside organic globules (Figure 4.4 (a) and (b)) (see Chapter 3). However, given the transformation of ACP into HA in the course of mineralization, only a residual presence ACP would be expected in sialoliths. Whi may have resulted from conversion of HA [1]. Nevertheless, this hypothesis remains to be proven, since maturation of HA into Whi occurs *in vitro* only at high temperature (~ 700 °C) [43]. Mg concentration, saliva pH and concentration of crystallization inhibitors/enhancers are known to play important roles in the precipitation mechanisms of calcium phosphates [16, 17, 44], and may critically catalyse or inhibit specific crystallization paths. In any case, the present results show that the mineralization mechanisms in sialoliths are complex and require further investigation.

The specimens studied presented a major organic fraction corresponding to ~ 65 % of the hydrated volume (Table 4.2). Although the μ CT cross-sections in Figure 4.5 suggest prevalent mineralized regions, it should be noted that these consist of nanometric crystals dispersed in a water-based gel matrix (see Figure 4.4 (d) and (e) and Table 4.2) [37]. The dry density reported in the literature for sialoliths ($1.1 - 1.4$ g/cm³ [45, 46]) is lower than the values measured in the present study for hydrated sialoliths (1.8 ± 0.2 g/cm³). This difference

is justified by the fact that the loss of water from the organic matter is not proportionally reflected in volume reduction, and emphasizes the need to investigate the specimens in hydrated state.

The sialoliths' geometry: spherical, oval or asymmetrical [23] (Figure 4.5), is associated with the anatomical location [47, 48]. Most of the specimens investigated in the present study had relatively high aspect ratios ($Ar > 2$) (Table 4.3) consistent with the geometric constraints in the ducts of salivary glands [47]. In addition, the mineralization process of sialoliths is conditioned by the flow dynamics of saliva at their surface [23]. Regardless of the calculi morphology, low-velocity regions are formed near the calculi anterior and posterior surface [23]. This effect enhances the local precipitation of Ca^{2+} , PO_4^{3-} and Mg^{2+} and results in an anisotropic elongation of the calculi in the saliva flow direction [23]. The high dispersion of the volume, eccentricity and mean diameter values can be partly justified by the variable time between nucleation and surgical extraction.

The variable mineralization of the sialoliths' nuclei reflects different nucleation processes [33, 49-51]: heavily mineralization compatible with nucleation based on accretion of calcified sialomicroliths [36], whereas weakly mineralization at the initial stages points to condensation of stagnant secretory material and cellular components poor in calcium [36]. These two nucleation mechanisms present similar rates of occurrence as evaluated using an arbitrary threshold (50 % of enamel's attenuation, see Figure 4.5 and Figure 4.6). Calculi with multiple cores (see S₃₂ in Figure 4.5) or without any core (see S₃₀ and S₄₀ in Figure 4.5) are atypical. Additional statistical analysis of the mineralization level at the nucleation region may be able to provide a deeper understanding of the initial stages of sialolith formation.

The internal structure revealed growth patterns ranging between concentric (e.g., S₃₃ in Figure 4.5) and irregular (e.g., S₄₀ in Figure 4.5) which have been proposed to be associated, respectively, with (quasi) steady-state growth and recurrent inflammation/infection episodes

that induce growth perturbations (see Chapter 3). Nevertheless, specific features suggest common mechanisms (Figures 4.5 and 4.6):

- Heavy mineralization around the nucleation region (with maxima at $R \approx 1.2$ mm);
- Cyclic mineralization with variable periodicity that may be associated with temporary depletion of the mineralization species below the precipitation threshold.
- Reduced variation of the local mineralization at later stages [23].

The X-ray attenuation values obtained by μ CT are similar to the ones reported in a previous study [45]. The relation between X-ray attenuation and the mineralization level of sialoliths is established in (Figure 4.7). These results show that orthodontic wax and human enamel are reliable phantoms for μ CT of sialoliths. The dispersion of the attenuation values for each specimen was rather independent of the average mineral density, in agreement with the variation in mineralization degree observed by electron microscopy.

The sialolith volumes determined from *in vivo* and *ex vivo* HCT using Otsu's thresholding show deviations below 15 % relative to the μ CT data (black data Figure 4.8 (a)). Therefore, the relatively large differences in attenuation between the calculi and the background enabled correct segmentations. However, the fine internal structure of the specimens was poorly resolved in HCT and volume averaging at the specimens' periphery increased the uncertainty in estimating the average attenuation. In fact, values obtained by HCT show differences up to 55 % in relation to μ CT for larger sialoliths data in Figure 4.8 (a). This indicates that tooth enamel ($\bar{R} = 2$ mm) is not a suitable phantom for HCT gain calibration: the reduced size in relation to the spatial resolution resulted in strong averaging with the less opaque surrounding voxels, which lowered significantly the average HCT attenuation of the phantom compared to μ CT data. Similar averaging occurred for small sialoliths producing lower differences between HCT and μ CT data for these specimens, while

for larger sialoliths, the average contribution from external voxels was weaker, which resulted in higher attenuation compared to enamel and, therefore, in greater deviations between HCT and μ CT values. These problems can be mitigated with larger phantoms, as shown in Figure 4.8 (b), where attenuation differences of $\sim 35\%$ were obtained for small specimens and the poorest HCT resolution. The deviations in relative attenuation between HCT and μ CT data showed stronger dependence on the slice thickness (along the z direction and governed by the collimation width) than on the in-plane pixel size (Figure 4.8 (b)). The deviations in attenuation are below 10% for specimens with $\bar{R} > 10 \times \text{slice thickness}$, demonstrating that the relative attenuation of sialoliths can be accurately determined with HCT when high z-axis spatial resolution is employed (Figure 4.8 (b)).

The present work shows that the mineralization degree of sialoliths can be determined from the *in vivo* X-ray attenuation through the calibration relations present in Figure 4.7. Several experimental models have been developed to predict the outcome of shock wave lithotripsy in renal calculi [26, 52, 53], while clinical trials have already established correlations between the outcome of shock wave lithotripsy and the size and attenuation of salivary calculi [54]. Therefore, the proposed methodology can assist physicians in selecting the most suitable lithotripsy technique(s) for each patient [55].

4.3. Summary

The major mineral component of the sialoliths is magnesium-substituted, calcium-deficient, type-B carbonated hydroxyapatite (89 vol. %), often mixed with substoichiometric Mg-whitlockite (11 vol. %). The similarity between their FTIR signatures demonstrates that the organic matter originates from saliva. The organic fraction in the sialoliths investigated corresponds to 65% of the calculi hydrated volume.

Information on the morphology and degree of mineralization of sialoliths is relevant for a correct selection of lithotripsy procedures. The method proposed here for calibration of *ex vivo* and *in vivo* X-ray computed tomography data offers a first approach for in-depth characterization of sialoliths in pre-therapeutic context.

4.4. References

1. Sakae T, *et al.*, Mode of occurrence of brushite and whitlockite in a sialolith, *J Dent Res*, 60:842-844, 1981
2. Teymoortash A, *et al.*, Sialolith crystals localized intraglandularly and in the Wharton's duct of the human submandibular gland: an X-ray diffraction analysis, *Arch Oral Biol*, 48:233-236, 2003
3. Gomes S, *et al.*, Thorough analysis of silicon substitution in biphasic calcium phosphate bioceramics: a multi-technique study, *Acta Biomater*, 6:3264-3274, 2010
4. Gopal R, *et al.*, Crystal Structure of Synthetic Mg-Whitlockite, $\text{Ca}_{18}\text{Mg}_2\text{H}_2(\text{PO}_4)_{14}$, *Can J Chem*, 52:1155-1164, 1974
5. Blumenthal NC, *et al.*, Formation and structure of Ca-deficient hydroxyapatite, *Calcif Tissue Int*, 33:111-117, 1981
6. Kong J, Yu S, Fourier transform infrared spectroscopic analysis of protein secondary structures, *Acta Biochim Biophys Sin (Shanghai)*, 39:549-559, 2007
7. Movasaghi Z, *et al.*, Fourier Transform Infrared (FTIR) Spectroscopy of Biological Tissues, *Appl Spectrosc Rev*, 43:134-179, 2008
8. Jayasree RS, *et al.*, Spectroscopic and thermal analysis of a submandibular sialolith of Wharton's duct resected using Nd:YAG laser, *Lasers Med Sci*, 23:125-131, 2008
9. Rehman I, Bonfield W, Characterization of hydroxyapatite and carbonated apatite by photo acoustic FTIR spectroscopy, *J Mater Sci Mater Med*, 8:1-4, 1997

10. Sabot JF, *et al.*, Analytical investigation of salivary calculi, by mid-infrared spectroscopy, *Analyst*, 137:2095-2100, 2012
11. Wopenka B, Pasteris J, A mineralogical perspective on the apatite in bone, *Mater Sci Eng*, 25:131-143, 2005
12. LeGeros RZ, Calcium phosphates in oral biology and medicine, *Monogr Oral Sci*, 15:1-201, 1991
13. Winand L, Physico-chemical study of some apatitic calcium phosphates, In *Tooth Enamel*, Stack MV, Fearnhead RS (eds), Bristol, England, John Wright and Sons, 1965
14. LeGeros RZ, Properties of osteoconductive biomaterials: calcium phosphates, *Clin Orthop Relat Res*, 81-98, 2002
15. Legeros RZ, Formation and stability of synthetic apatites: effect of some elements, *Calcium Phosphates in Oral Biology*, 15:82-107, 1982
16. LeGeros RZ, *et al.*, Magnesium and carbonate in enamel and synthetic apatites, *Adv Dent Res*, 10:225-231, 1996
17. Russel G, *et al.*, Inhibitors of mineralization, In *Biological Mineralization*, New York, USA, John Wiley and Sons, pp.807-825, 1973
18. Nolasco P, *et al.*, Structure and growth of sialoliths: computed microtomography and electron microscopy investigation of 30 specimens, *Microsc Microanal*, 19:1190-1203, 2013
19. Nolasco P, *et al.*, Local Response of Sialoliths to Lithotripsy: Cues on Fragmentation Outcome, *Microsc Microanal*, 23:584-598, 2017
20. Alves de Matos AP, *et al.*, On the structural diversity of sialoliths, *Microsc Microanal*, 13:390-396, 2007
21. Skinner HCW, Biominerals, *Mineral Mag*, 69:621-641, 2005
22. LeGeros RZ, LeGeros JP, Phosphate minerals in human tissue, In *Phosphate Minerals*, Nriagu JO, Moore PB (eds), New York, USA, Springer-Verlag, pp.351-395, 1984

23. Zhu P, *et al.*, Computational fluid dynamics analysis of salivary flow and its effect on sialolithogenesis, *Oral Dis*, 20:624-630, 2014
24. Hasgall PA, *et al.*, IT'IS Database for thermal and electromagnetic parameters of biological tissues, Version 3.0, www.itis.ethz.ch/database, (09 of Septembe of 2017)
25. Heimbach D, *et al.*, Acoustic and mechanical properties of artificial stones in comparison to natural kidney stones, *J Urol*, 164:537-544, 2000
26. Saw KC, *et al.*, Helical CT of urinary calculi: effect of stone composition, stone size, and scan collimation, *AJR Am J Roentgenol*, 175:329-332, 2000
27. Lambda R, *et al.*, CT hounsfield of soft tissues on unenhanced abdominal CT scans: variability between two different manufacturers MDCT scanners, *Genitourinary Imaging*, 203:1013-1020, 2014
28. Patrick S, *et al.*, Comparison of gray values of cone-beam computed tomography with hounsfield units of multislice computed tomography: An in vitro study, *Indian J Dent Res*, 28:66-70, 2017
29. Prionas ND, *et al.*, Volume assessment accuracy in computed tomography: a phantom study, *J Appl Clin Med Phys*, 11:3037, 2010
30. Slomiany BL, *et al.*, Lipid composition of the matrix of human submandibular salivary gland stones, *Arch Oral Biol*, 27:673-677, 1982
31. Boskey AL, *et al.*, Lipids associated with mineralization of human submandibular gland sialoliths, *Arch Oral Biol*, 26:779-785, 1981
32. Anneroth G, *et al.*, The relation of lipids to the mineral components in salivary calculi, *J Oral Pathol*, 6:373-381, 1977
33. Szalma J, *et al.*, Proteomic and scanning electron microscopic analysis of submandibular sialoliths, *Clin Oral Investig*, 17:1709-1717, 2013
34. Bennick A, *et al.*, The location and nature of calcium-binding sites in salivary acidic proline-rich phosphoproteins, *J Biol Chem*, 256:4741-4746, 1981

35. Vitorino R, *et al.*, Identification of human whole saliva protein components using proteomics, *Proteomics*, 4:1109-1115, 2004
36. Harrison JD, Causes, natural history, and incidence of salivary stones and obstructions, *Otolaryngol Clin North Am*, 42:927-947, 2009
37. Harrison JD, Natural history of chronic sialadenitis and sialolithiasis, In *Modern Management Preserving the Salivary Glands*, Nahlieli O, McGurk M, Iro H, Zenk J (eds), Herzeliya, Isradon Publishing House, pp.93–135, 2007
38. Teymoortash A, *et al.*, Bacteria and pathogenesis of human salivary calculus, *Acta Otolaryngol*, 122:210-214, 2002
39. Fábíán KT, *et al.*, Saliva in Health and Disease, Chemical Biology of, In *Wiley Encyclopedia of Chemical Biology*, John Wiley and Sons, Inc, pp.1-9, 2008
40. Mahamid J, *et al.*, Mapping amorphous calcium phosphate transformation into crystalline mineral from the cell to the bone in zebrafish fin rays, *Proc Natl Acad Sci U S A*, 107:6316-6321, 2010
41. Dorozhkin SV, Calcium orthophosphates: applications in nature, biology, and medicine, Singapore, Pan Stanford, 2012
42. Habraken WJ, *et al.*, Ion-association complexes unite classical and non-classical theories for the biomimetic nucleation of calcium phosphate, *Nat Commun*, 4:1507, 2013
43. Dorozhkin SV, Mechanism of solid-state conversion of non-stoichiometric hydroxyapatite to diphase calcium phosphate, *Russ Chem Bull*, 52:2639-2375, 2003
44. Grases F, *et al.*, Sialolithiasis: mechanism of calculi formation and etiologic factors, *Clin Chim Acta*, 334:131-136, 2003
45. Schrotzlmair F, *et al.*, Laser lithotripsy of salivary stones: Correlation with physical and radiological parameters, *Lasers Surg Med*, 47:342-349, 2015
46. Ho SP, *et al.*, Kidney stones compared to Dental calculi and Salivary stones: Comparative analyses of mineral density and ultrastructure, *J Urol*, 195:e778-e779, 2016

47. Seldin HM, *et al.*, Conservative surgery for the removal of salivary calculi, *Oral Surg Oral Med Oral Pathol*, 6:579-587, 1953
48. Williams MF, Sialolithiasis, *Otolaryngol Clin North Am*, 32:819-834, 1999
49. Giray CB, *et al.*, Sialolith characterization by scanning electron microscopy and X-ray photoelectron spectroscopy, *Scanning*, 29:206-210, 2007
50. Kasaboğlu O, *et al.*, Micromorphology of sialoliths in submandibular salivary gland: A scanning electron microscope and X-ray diffraction analysis, *J Oral Maxillofac Surg*, 62:1253-1258, 2004
51. Kinoshita H, *et al.*, Phosphate and amide III mapping in sialoliths with Raman microspectroscopy, *J Raman Spectrosc*, 39:349-353, 2008
52. Zarse CA, *et al.*, Helical computed tomography accurately reports urinary stone composition using attenuation values: in vitro verification using high-resolution micro-computed tomography calibrated to fourier transform infrared microspectroscopy, *Urology*, 63:828-833, 2004
53. Nakada SY, *et al.*, Determination of stone composition by noncontrast spiral computed tomography in the clinical setting, *Urology*, 55:816-819, 2000
54. Escudier MP, *et al.*, Factors influencing the outcome of extracorporeal shock wave lithotripsy in the management of salivary calculi, *Laryngoscope*, 120:1545-1549, 2010
55. Koch M, *et al.*, Multimodal treatment in difficult sialolithiasis: Role of extracorporeal shock-wave lithotripsy and intraductal pneumatic lithotripsy, *Laryngoscope*, 2017

Chapter 5. Local response of sialoliths to lithotripsy

Overview

In this chapter, the hardness (H) and the Young's modulus (E) of sialoliths is determined at different scales by indentation techniques. Specific damage induced in the structure of sialoliths by ultrasonic vibrations, pneumoballistic impacts, shock waves and laser ablation is investigated by scanning electron microscopy (SEM) coupled with X-ray energy dispersive spectroscopy (EDS) and X-ray computed microtomography (μ CT). Fundamental aspects of the response of sialoliths to mechanical fragmentation and laser ablation are discussed.

5.1. Results

5.1.1. Local and average mechanical behaviour

Nanoindentation experiments were performed taking into account the local diversity of the sialoliths' ultrastructure in terms of mineralization degree and morphology: (a) homogeneous organic matrix with low mineralization, (b) highly mineralized regions and (c) composite material presenting organic globules with surrounding (and internal) mineralized regions (Figure 5.1). Since the nanoindentations were smaller than the composite's morphological features, the properties of the organic and mineralized regions were measured independently (see Figure 5.1 (c)). EDS point analyses attested for the similarity of each type of matter in the different configurations (see spectra in Figure 5.1 and their quantification in Table 5.1 where relevant differences are highlighted in shaded blue). Figure 5.1 (d) to (f) presents 2D distributions of Young's modulus *vs.* hardness obtained from nanoindentation experiments performed on the different structural typologies. The organic matrix presented a soft and uniform mechanical behaviour (Figure 5.1 (d)), while the mineralized matter exhibited significantly higher H and E values (Figure 5.1 (e)) and larger dispersions that point to higher

structural heterogeneity (see Figure 5.1 (b)). The composite material (Figure 5.1 (c)) shows a bimodal distribution with in-between H and E values in relation to the "purely" organic and mineralized regions due to the variable mineralization (Figure 5.1 (f)). Table 5.2 lists the mean values and standard deviations of estimated 2D Gaussian models ($\mu \pm \sigma$).

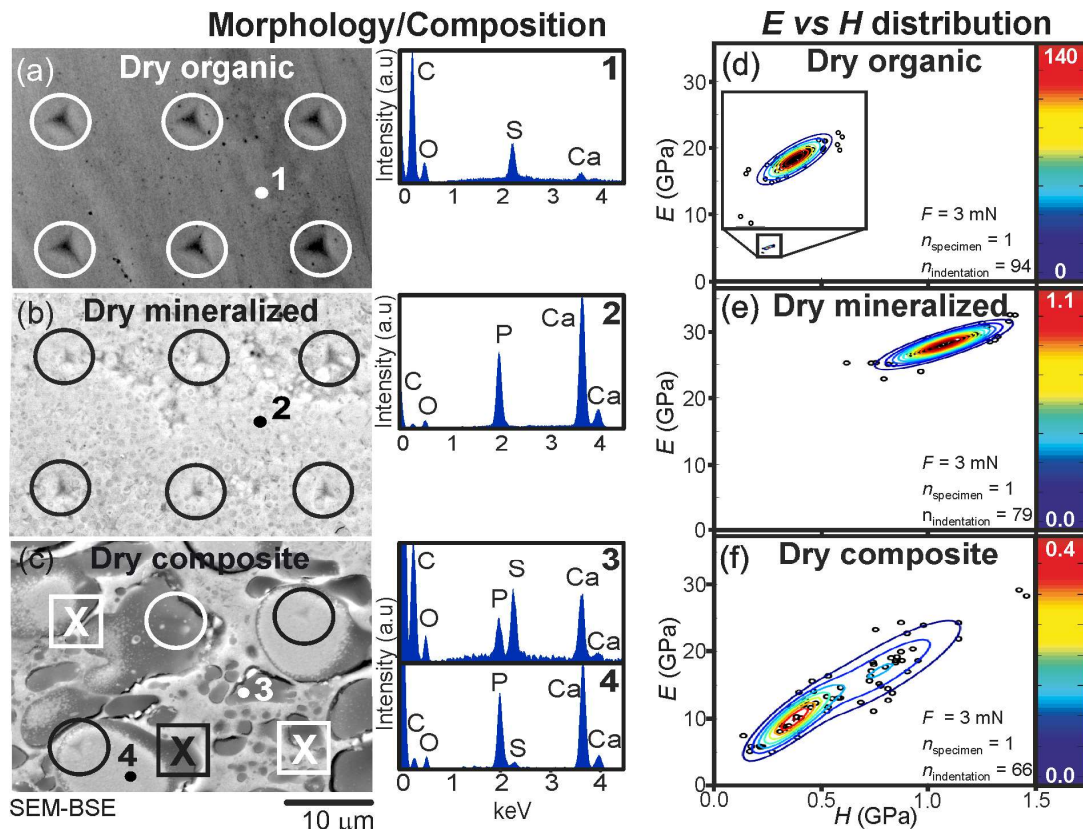


Figure 5.1 – (a) to (c) SEM (BSE) images showing the sialolith typologies in terms of morphology and local mineralization with corresponding EDS spectra. Berkovich nanoindentations are marked: ● - accepted, ☒ - excluded. (d) to (f) Young's modulus vs hardness distributions obtained from nanoindentations where the lines represent constant values of the fitted Gaussian models. In (f) the fitted model was a summation of two 2D Gaussians.

Table 5.1 - Standardless quantification of the spectra shown in Figure 5.1.

	C (wt. %)	O (wt. %)	P (wt. %)	S (wt. %)	Ca (wt. %)
1 Organic region in Figure 5.1 (a)	70 ± 1	24 ± 1	1 ± 1	5 ± 1	2 ± 1
3 Organic region in Figure 5.1 (c)	56 ± 3	18 ± 2	4 ± 1	8 ± 1	14 ± 1
2 Mineralized region in Figure 5.1 (b)	7 ± 1	25 ± 1	19 ± 1	1 ± 1	49 ± 1
4 Mineralized region in Figure 5.1 (c)	11 ± 2	17 ± 2	20 ± 1	1 ± 1	51 ± 1.5

N.B. Elements with atomic number lower than boron ($Z = 5$) cannot be detected by EDS, namely, hydrogen ($Z = 1$).

Figure 5.2 shows a microindentation performed on a dry sialolith with composite structure together with (H, E) distributions determined from microindentations performed on dry and hydrated sialoliths with composite structure. Table 5.2 lists the mean values and standard deviations ($\mu \pm \sigma$) of estimated 2D Gaussian models. Since the indentations were larger than the ultrastructural features, the properties measured at this scale are intrinsically averaged (see Figure 5.2 (a)). Indeed, the distributions obtained from dry and hydrated sialoliths present essentially a single mode (respectively, Figure 5.2 (b) and (c)). However, the distribution obtained from hydrated specimens presents a much softer average behaviour and larger value dispersion. The evolution of the mechanical properties along time was used to monitor the influence of dehydration during the microindentation experiments (Figure 5.3). The estimated low correlation value attests for a minor effect. Radial cracks emanating from Vickers microindentations have not been observed [1].

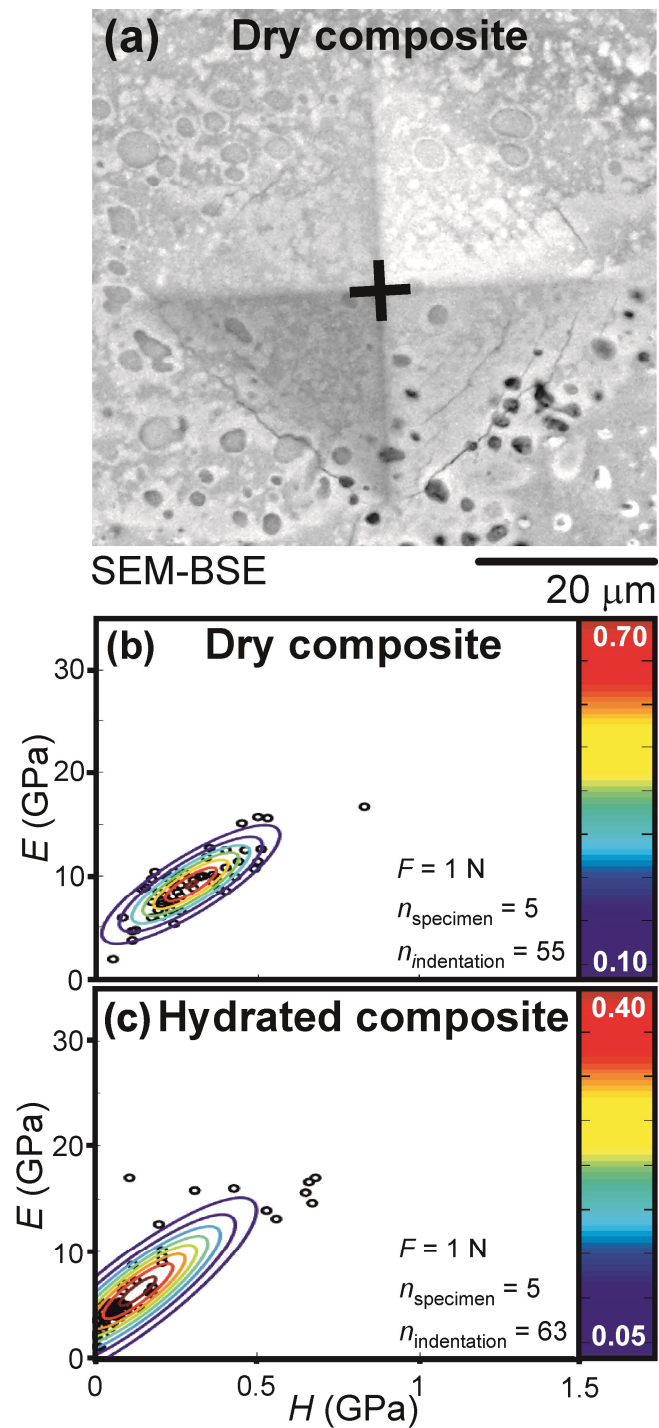


Figure 5.2 - (a) SEM (BSE) image of a Vickers microindentation (1 N) performed on a dry sialolith. Microindentations in hydrated specimens could not be clearly discerned by SEM. (b) and (c) Young's modulus vs hardness distributions obtained from, respectively, dry and hydrated sialoliths, where the lines represent constant values of the fitted 2D Gaussian models.

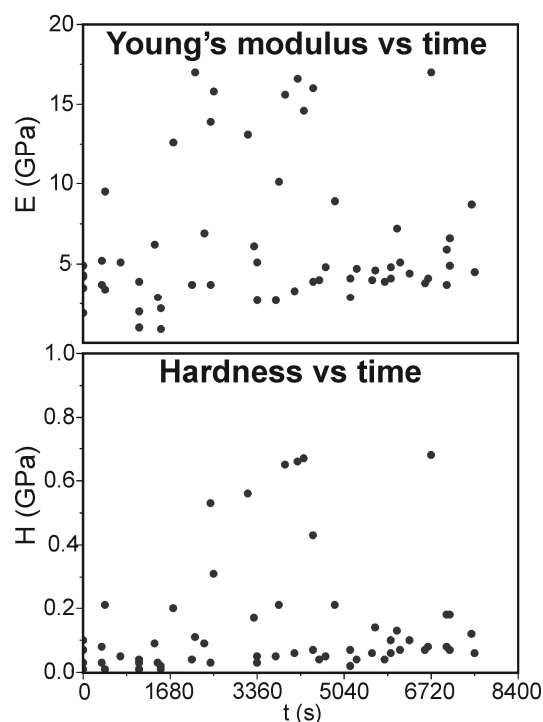


Figure 5.3 - Effect of loss of hydration water during microindentation experiments. Each set of experiments was carried out for about 2 h with a relative humidity of 70 %. The linear correlation factor with time (r) was 0.10 for E and 0.16 for H .

Table 5.2 – Young's modulus and hardness estimated from nano, micro and macroindentation.

Indentation characteristics	Calculi typology ($n_{\text{specimen}}, n_{\text{indentation}}$)	Hardness (GPa) ($\mu \pm \sigma$)	Young's modulus (GPa) ($\mu \pm \sigma$)
Nanoindentation $F = 3 \text{ mN}$ Berkovich indenter	Dry organic (1,94)	0.25 ± 0.01	5.0 ± 0.16
	Dry mineralized (1,79)	1.1 ± 0.15	28.1 ± 1.70
	Dry composite (organic regions) (1,30)	0.37 ± 0.11	9.72 ± 2.94
	Dry composite (mineralized regions) (1,36)	0.78 ± 0.24	17.30 ± 4.90
Microindentation $F = 1 \text{ N}$ Vickers indenter	Dry composite (5,55)	0.29 ± 0.14	9.15 ± 2.92
	Hydrated composite (5,63)	0.14 ± 0.18	6.20 ± 4.32
Macroindentation $F = 300 \text{ N}$ Vickers indenter	Hydrated composite (5,6)	0.15 ± 0.04	-
Macroindentation $F = 500 \text{ N}^*$ Vickers indenter	Hydrated composite (1,1)	0.23	-

* Only one specimen was sufficiently large to withstand this high load.

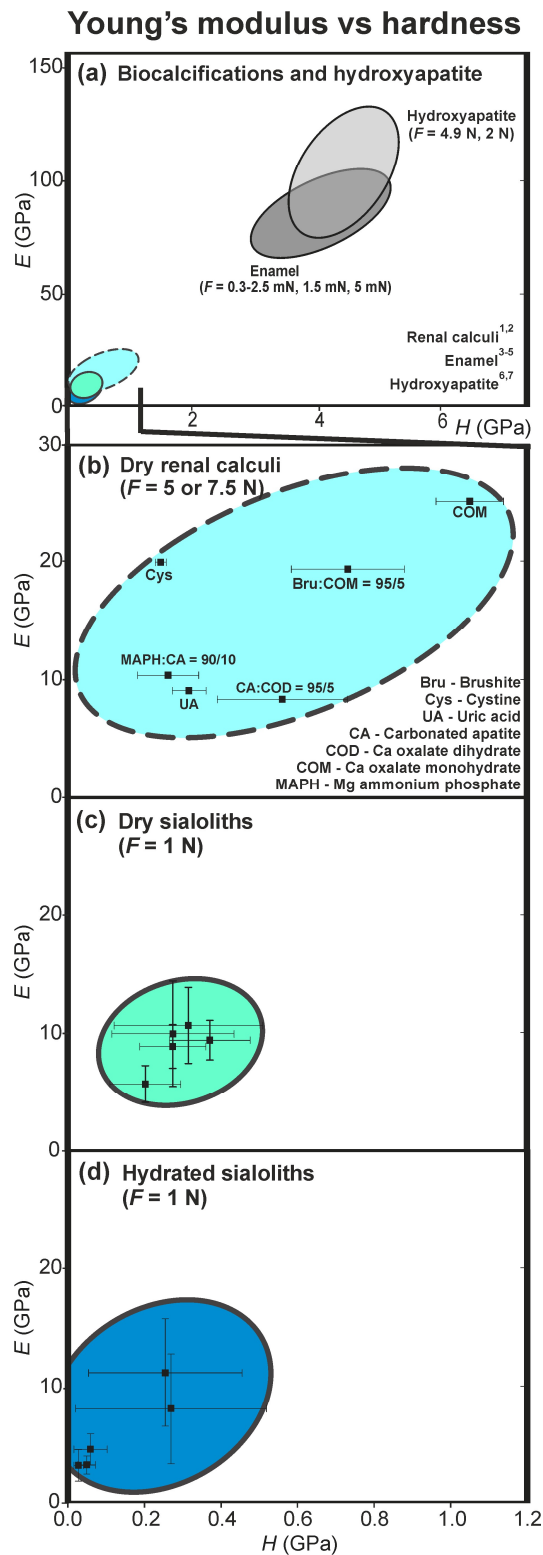


Figure 5.4 - (a) Young's modulus vs hardness where the domains enclose mean \pm standard deviation ($\mu \pm \sigma$). Data: [1, 2] for renal calculi, [3, 4, 5] for enamel, [6, 7] for hydroxyapatite, and present work for sialoliths. (b) Magnified detail for renal calculi with $\mu \pm \sigma$ values from literature. As standard deviations for E were not reported, the domain encloses $\mu \pm \sigma$ for H but only μ for E and is represented by a dashed line. (c) Magnified detail for dry composite sialoliths for the 5 specimens tested. (d) Magnified detail for hydrated composite sialoliths for the 5 specimens tested.

The H and E data determined from the microindentation experiments is presented in Figure 5.4 together with literature values for renal calculi [1, 2], enamel [3-5] and sintered hydroxyapatite [6, 7]. Figure 5.4 (c) and (d) shows the same data as Figure 5.2 (b) and (c), respectively, but instead of global value distributions, here the mean \pm standard deviation ($\mu \pm \sigma$) is represented for each of the 5 specimens investigated. Enamel, which is composed of 94-96 % hydroxyapatite [8], presents hardness and Young's modulus values that are approximately one order of magnitude above those of renal and salivary calculi (Figure 5.4 (a)). On average, renal calculi present higher (H, E) values than sialoliths (Figure 5.4 (b) versus (c)), although their mechanical properties depend strongly on the specific composition. In the case of sialoliths, the compositions of mineralized and organic regions were consistent across the set of specimens studied and the differences in mean value and dispersion are essentially related to the global and local mineralization degree as well as hydration degree (Figure 5.4 (c) and (d)).

Hardness values determined from hydrated sialoliths using forces of 300 and 500 N are also listed in Table 5.2. These macroscale values are within the range defined at the microscale for hydrated sialoliths (see Table 5.2 and Figure 5.4 (d)).

5.1.2. Local and extended damage patterns

Figure 5.5 illustrates the diversity observed in the fracture behaviour of sialoliths. Microindentation induced circumferential crack lines (Figure 5.5 (a)) and the patterns of crack propagation indicate that the mineralized matter confers structural strength, while organic regions and/or interfaces tend to deflect cracks or cease their progression (see Figure 5.5 (b)). In other instances, the fracture surfaces exhibited dimples characteristic of ductile fracture [9] with particles/inclusions lying at the center of larger dimples (Figure 5.5 (c)).

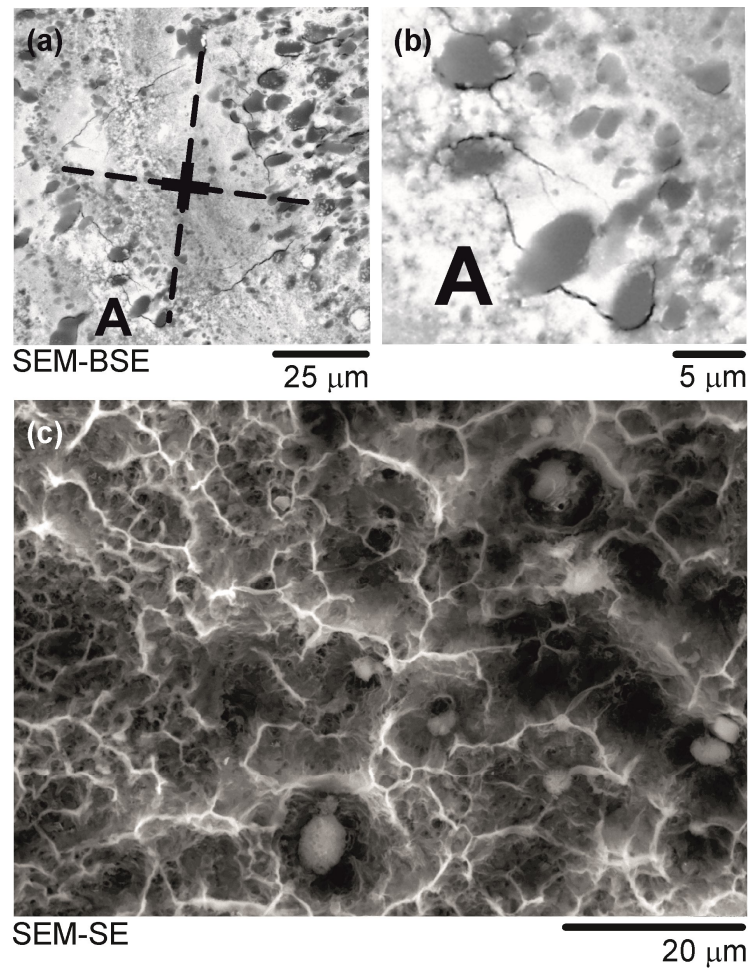


Figure 5.5 - (a) Crack pattern resulting from microindentation. (b) Magnified detail of (a) showing debonding at globule interfaces, crack deflection, branching and meandering. (c) Dimple fracture surface exhibiting textbook features of a ductile material containing rigid inclusions

Figure 5.6 shows the local damage induced in hydrated sialoliths by ultrasonic vibrations ((a) and (b)) and pneumoballistic impacts ((c) and (d)). Local damage produced by shock waves and laser ablation is illustrated in Figures 5.7 and 5.8, respectively. Ultrasonic vibrations and pneumoballistic impacts resulted in preferential fracture/spalling of heavily mineralized material, while organic matter was relatively unaffected (Figure 5.6 (b) and (d)).

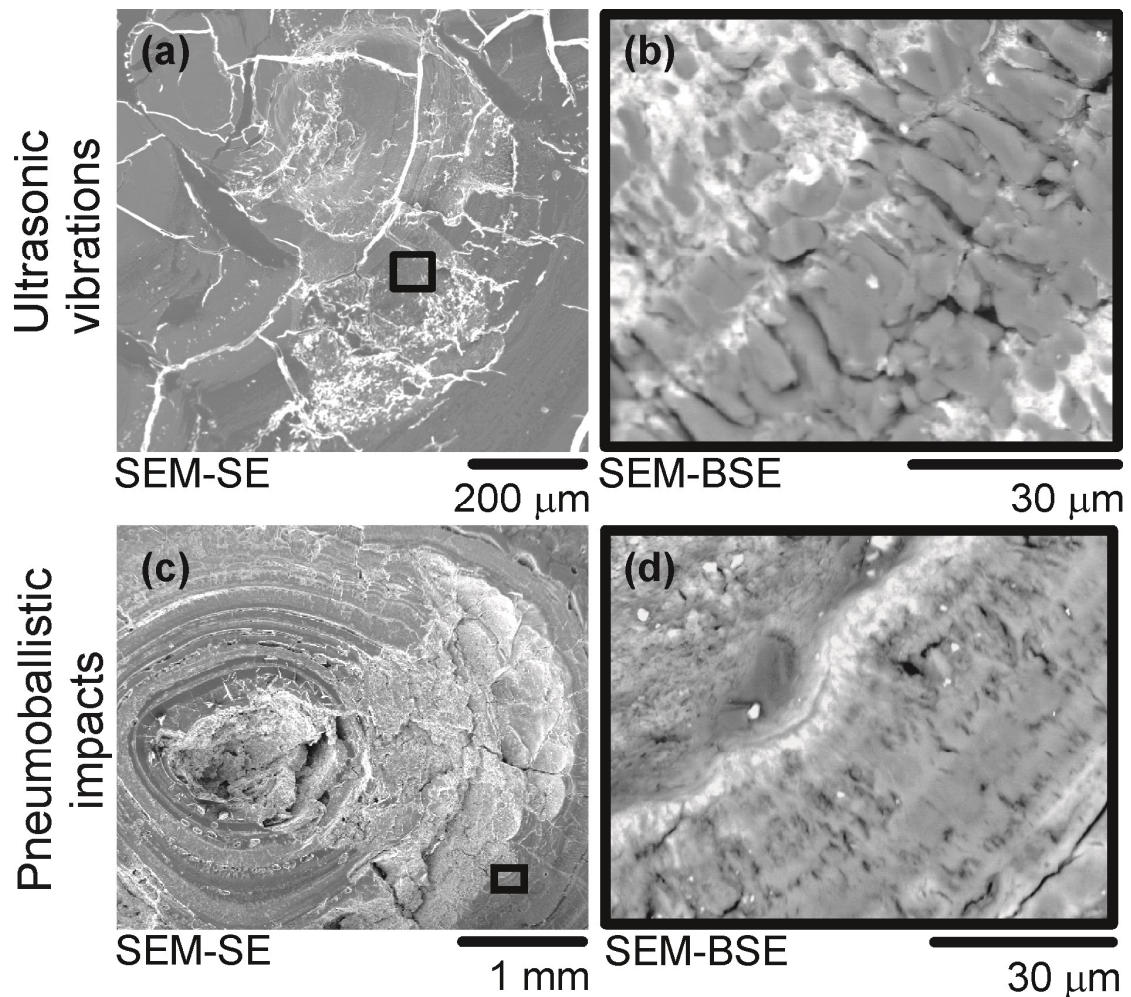


Figure 5.6 - (a) Damage caused by ultrasonic vibrations. (b) Magnified detail of (a) showing preferential extraction of mineralized matter (bright regions). (c) Damage caused by pneumoballistic impacts. (d) Magnified detail of (c) showing preferential removal of mineralized material.

In contrast, shock waves leached the organic components and left relatively unchanged the mineral components (compare Figures 5.7 (b) with 5.7 (e) and 5.6 (b) with 5.7 (c)). Leaching of the organic matrix resulted in alveolar morphologies (Figure 5.7 (d)) and was associated with flow of mineralized matter (which consists of hydroxyapatite nanocrystals dispersed in an organic gel) (Figure 5.7 (e)).

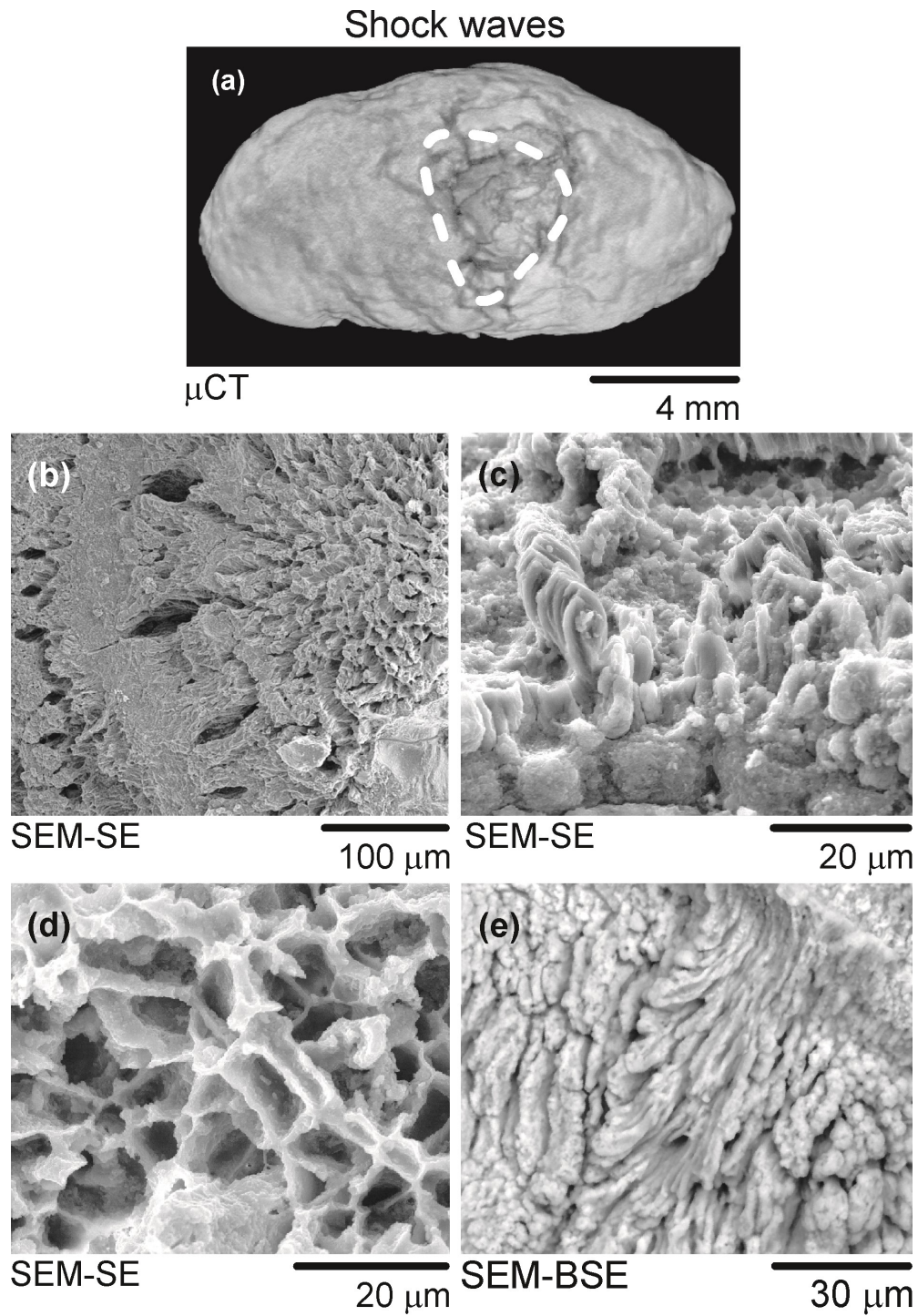


Figure 5.7 - Damage caused by shock waves. (a) Damaged sialolith's rendered volume. (b) to (d) Structures resulting from preferential removal of organic matter. (e) Flow of highly mineralized matter.

The damage induced by the Ho:YAG laser to the sialoliths' structure was rather confined (Figure 5.8 (a)). Laser ablation occurred mostly by melting and vaporization of the sialoliths' components (Figure 5.8 (b)), while cracking indicates that the surrounding areas were damaged by mechanical phenomena (Figure 5.8 (a)). Both molten mineralized matter (Figure 5.8 (b)) and stand-alone globules (Figure 5.8 (c)) have been found at the walls of the irradiated regions suggesting similar ablation rates. Further systematic studies are required to establish differences in the response of the two components.

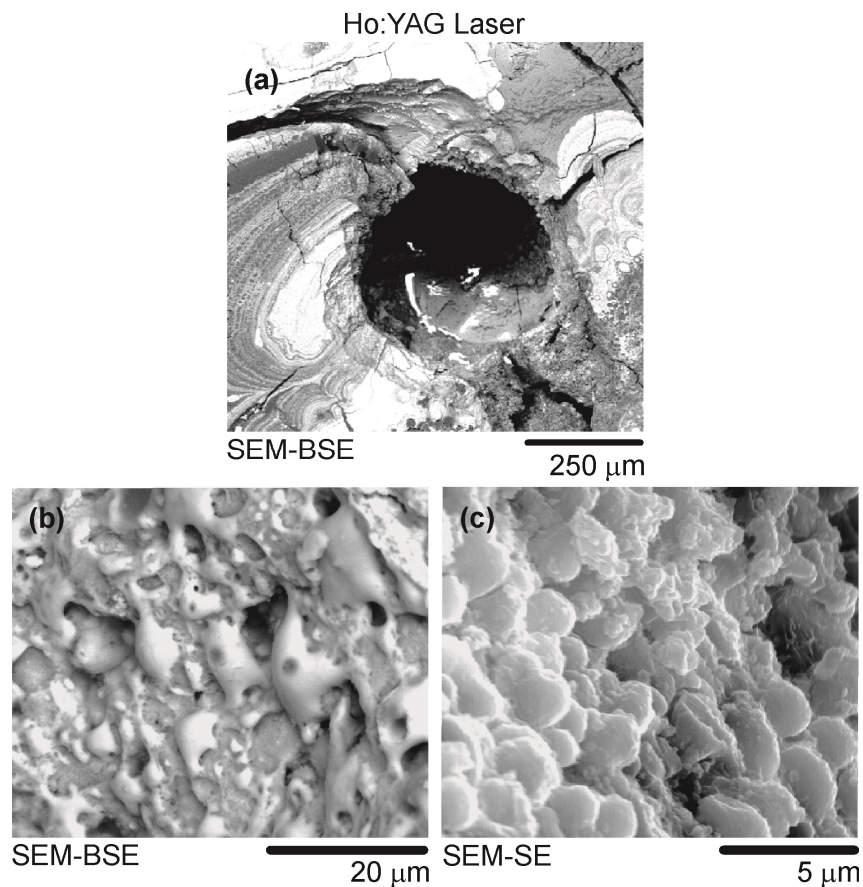


Figure 5.8 - (a) Damage caused by the Ho:YAG laser. (b) Detail of the wall around the irradiated area evidencing melting. (c) Detail of the wall around the irradiated area showing globules.

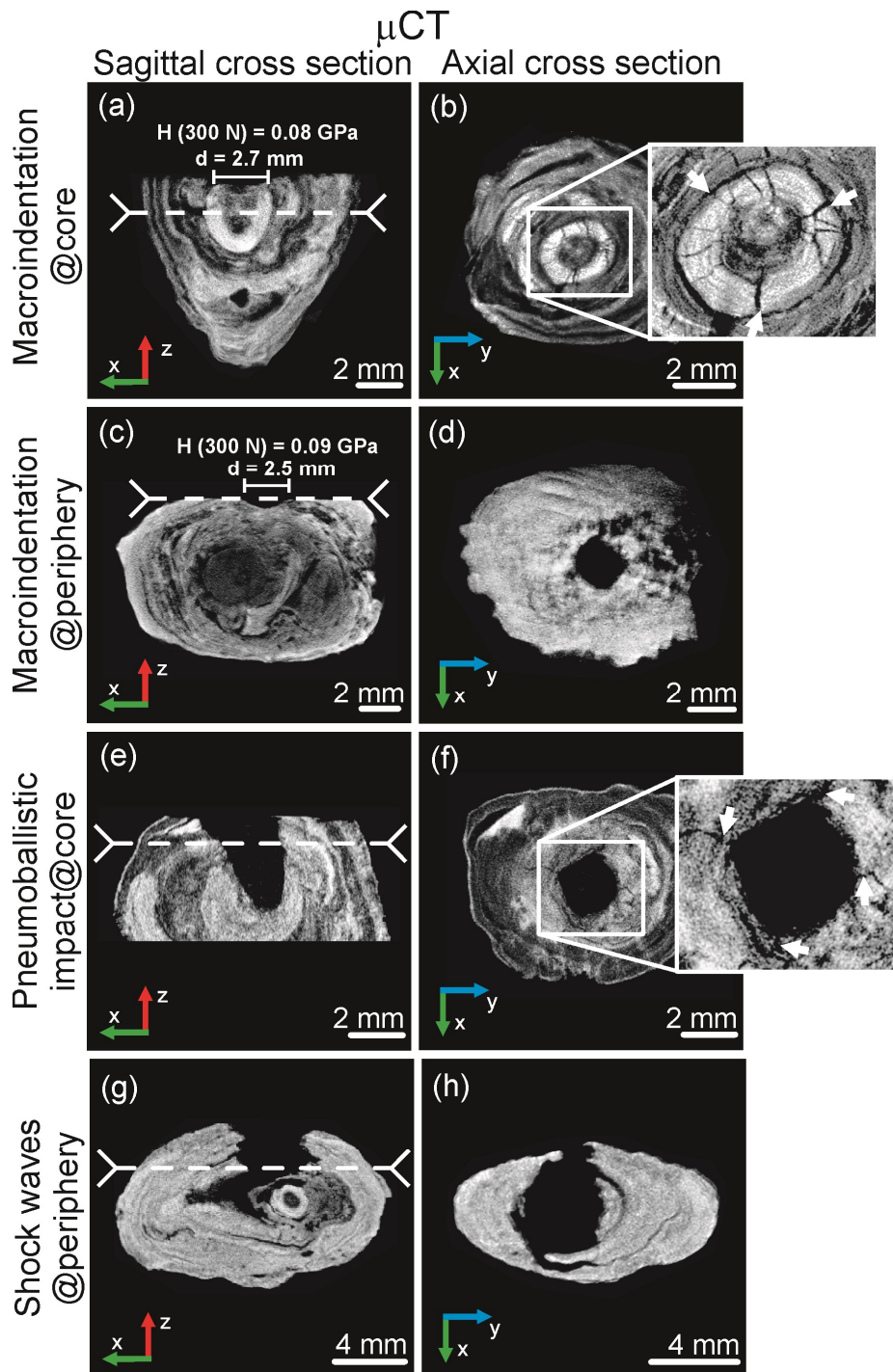


Figure 5.9 - μ CT sagittal and axial sections showing extended damage resulting from (a) to (d) macroindentation, (e) and (f) pneumoballistic impacts, and (g) and (h) shock waves. Indentation data is given in the corresponding legends. The dashed line on the sagittal section indicates the position of the axial section.

Figure 5.9 presents μ CT sections showing the extended damage induced in hydrated sialoliths by macroindentations ((a) to (d)), pneumoballistic impacts ((e) and (f)) and shock waves ((g) and (h)). As the volumes affected by ultrasonic vibrations and laser ablation were small, extended damage was not observed for these techniques. The damage caused by macroindentations was strongly dependent on the underlying ultrastructure and mineralization degree. For instance, crack patterns typical of brittle materials were generated in highly mineralized regions around the indentation (Figure 5.9 (a) and (b)), while less severe damage was induced in more homogeneous but less mineralized regions for the same indentation parameters (see Figure 5.9 (c) and (d)). A similar behaviour has been observed for pneumoballistic impacts (Figure 5.9 (e) and (f)). Shock waves produced delamination of the (roughly) concentric layers but not extended cracking (Figure 5.9 (g) and (h)).

5.2. Discussion

5.2.1. Local and average mechanical behaviour

In general, sialoliths can be described as biocomposites consisting of a soft component (weakly mineralized organic matrix), dispersed in a hard component (heavily mineralized organic matrix). The average H and E at the micro- and macro- scales fall between the values measured for the individual organic and mineral components (Table 5.2), suggesting a behaviour roughly compatible with a 'rule of mixtures' employed in the field of composite materials [10].

The extremely high hardness and Young's modulus of enamel are a reflection of the high degree of mineralization and of the spatial organization of the hydroxyapatite crystals in this biocomposite [8, 11]. Poorer mineralization and structural disorder contribute to lower H and E both in sialoliths and calciferous renal calculi (Figure 5.4 (a)). Yet, dry sialoliths tend to

present even lower values than those of dry Ca-based phosphate renal calculi (Figure 5.4 (b) and (c)). This can be justified by the higher fraction of organic matrix in sialoliths (e.g. 18 % of dry weight [12]) compared to calciferous renal calculi (about 2 % of the total dry weight [13]). In fact, dry sialoliths can even be softer than acid uric and cystine calculi, which are essentially organic [14]. This is likely due to the different structural organization; acid uric and cystine present crystallized structures in renal calculi [15, 16], while the degenerated secretory materials that compose the organic matter in sialoliths are (hydrated) gels.

Mechanical characterization is often performed on dry calculi [1, 17, 18]. However, sialoliths are significantly harder in dry conditions than *in vivo* (compare Figure 5.4 (c) and (d)) and therefore relevant mechanical evaluation requires hydrated conditions. A similar trend has been reported for renal calculi, although the average H and E values obtained for hydrated sialoliths (Table 5.2) are significantly lower than the ones reported for hydrated renal calculi [14]. Remarkably, hydration lowers the low- H /low- E region of the (H,E) domain without significantly affecting the high- H /high- E region. This indicates that drying strengthens sialoliths by changing the behaviour of the organic matter, while mineralized regions retain their properties. Therefore, in hydrated states, the mechanical behaviour of sialoliths depends strongly on the fraction of organic matter. Thermal calorimetric studies showed that the loss of hydration water occurs essentially in the organic component [19], supporting the present observations.

Since the ultrastructure of sialoliths is sufficiently fine, the experiments carried out at the microscale seem to conveniently describe the mechanical behaviour of the whole structure (compare the micro and macroindentation results in Table 5.2).

5.2.2. Local and extended damage

Generally, sialoliths exhibit the fracture behaviour of composite materials consisting of a brittle medium with ductile inclusions (Figure 5.6 (b)). However, in some instances, the fracture surfaces are representative of composites consisting of a ductile medium with rigid inclusions (Figure 5.6 (c)). The diversity of morphologies and variable mineralization observed in the ultrastructure of sialoliths point to fracture behaviour of mixed characteristics.

Figure 5.10 (a) illustrates the toughening mechanisms typically associated with a brittle medium with ductile inclusions. In these systems, weak interfaces play a key role in toughening by debonding, which diverts the excess energy required by the new surfaces from the crack propagation process.

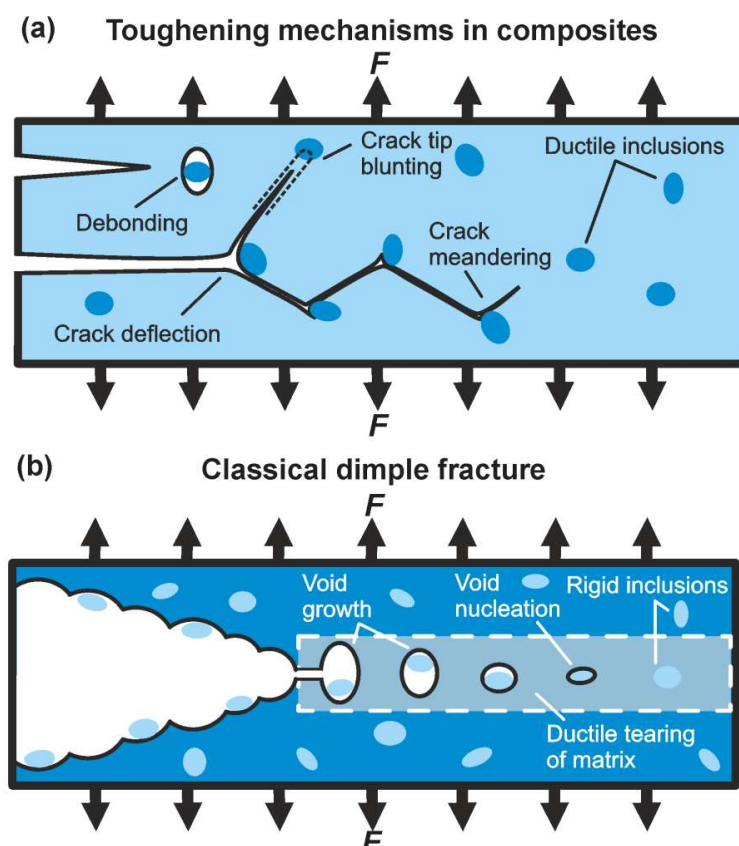


Figure 5.10 - (a) Toughening mechanisms in a brittle matrix containing dispersions of ductile inclusions. (b) Classical dimple fracture in a ductile material containing rigid inclusions. Adapted from [22]

Crack deflection, meandering and branching increase the total fracture surface and are also effective means of dissipating energy [20]. Blunting of the crack tip consumes energy during the plastic deformation of the ductile component, a process that delays crack progression and lessens the stress concentration at the tip. These mechanisms have been identified in highly mineralized regions with dispersions of organic globules (see Figure 5.5 (b)). Microindentation of calciferous renal calculi with over 95 wt. % of mineral content results in circumferential and radial crack lines [1, 21]. However, radial cracks emanating from microindentations were not observed in hydrated sialoliths. This indicates that these calcifications do not present a typical brittle behaviour, attesting for the role of the organic component in hindering crack propagation.

Dimple fracture surfaces, shown schematically in Figure 5.10 (b), represent the classical failure mechanism in the case of a ductile medium with rigid inclusions. The process is associated with large plastic deformation and ductile tearing in a so-called active layer (dashed rectangle in Figure 5.10 (b)); as a result, microscopic voids form, grow and eventually coalesce, which lead to the distinctive dimple structure. The presence of rigid inclusions, which do not deform at the same rate, favours dimple nucleation [9] leading to fracture surfaces where particles sit at the center of larger dimples (Figure 5.5 (c)). This type of behaviour can be expected for weakly mineralized regions.

The crack propagation patterns and fracture surfaces could only be clearly observed in dry sialoliths. However, assuming that mineralized regions have similar mechanical properties in hydrated and dry conditions, while organic regions are softer in hydrated states (see Figure 5.4 (c) and (d)), the mechanisms described above can also be anticipated for hydrated settings, such as *in vivo* ones.

The local damage caused by ultrasonic vibrations and pneumoballistic impacts is consistent with flakes breaking off (spalling) from mineralized regions and being

subsequently washed away, while the organic regions remained relatively unaffected (Figure 5.6 (a) and (b)). Conversely, shock waves caused preferential removal of the organic matter by a leaching process (Fig 5.7 (b) to (d)), and induced flow of the unsupported mineralized material (Figure 5.7 (e)). The comparison of Figure 5.6 (b) with Figure 5.7 (c) illustrates the opposite effects of the respective lithotripsy techniques.

Shock waves did not induce crack propagation in highly mineralized regions. This behaviour is probably related with a relatively high fraction of organic matrix in the mineralized regions themselves and with the presence of neighbouring compliant organic regions. Cavitation induced by shock waves is most likely the phenomenon responsible for dissolving and leaching the organic gel(s) [23]. The fractal patterns in the sialoliths' ultrastructure already indicate a flowing predisposition (see fractal patterns in Figure 3.8). Dissolution and flowing are less efficient in comminution than crack propagation, which justifies the relatively lower success rates achieved in the fragmentation of sialoliths compared to renal calculi [24-28].

The low strength of sialoliths (Figure 5.4 (d)) and the fact that they often collapse during surgical extraction (and ensuing handling) suggest that these structures are, in fact, less tough than renal calculi. Thus, the key to understand the lower efficiency of shock wave lithotripsy lies on the rheological behaviour of sialoliths rather than on their mechanical toughness. The cohesive-zone model is typically employed to describe the shock wave-induced failure of renal calculi, considered brittle materials for this purpose [29]. However, the viscous fingering detected in the ultrastructure of the sialoliths (see Chapter 3), the leaching of organic matter and the flowing patterns induced by shock waves demonstrate that fluid mechanics must be included in the description of the mechanical damage inflicted to sialoliths.

The Ho:YAG laser produced wells resulting from melting/ejection of the underlying components (Figure 5.8 (a) and (b)). Similar damage has been found in dentine, enamel and

renal calculi, in which laser ablation occurred by photothermal phenomena, while photomechanical effects were secondary and evident only around the irradiated zone [30, 31].

Although the parameters used in the ballistic, shock wave and laser ablation experiments are similar to parameters currently employed for renal calculi lithotripsy, a larger number of specimens would be required to reach definite and generalized conclusions regarding the comminution behaviour of sialoliths. Nevertheless, in the present case, extended damage was achieved with shock waves and pneumoballistic impacts (Figure 5.9 (e) to (h)), while laser ablation induced rather confined destruction (Figure 5.8 (a)). This suggests that mechanical methods are better suited for comminution of large sialoliths, whereas laser ablation can be useful for precise drilling/dusting of small sialoliths or fragments generated by other lithotripsy techniques. Nevertheless, the high fraction and fine dispersion of organic matter in sialoliths reduces the local damage induced by mechanical means, which justifies the poorer performance of lithotripsy methods employed in sialolithiasis compared to nephrolithiasis management [24-27].

Multimodal approaches have been proposed to further optimize the lithotripsy outcome, in which the best-suited method available is chosen according to the calculi features inferred from *in-situ* characterization [32] (see Chapter 4). Nevertheless, by understanding the specific damage caused by each of the lithotripsy methods, the operational parameters can be fine-tuned to further optimize the fragmentation outcome of sialoliths [32-34].

5.3. Summary

Sialoliths can be generally described as biocomposites consisting of soft organic globules dispersed in a mineralized hard matrix. Organic globules finely dispersed in the ultrastructure of sialoliths condition the response to mechanical lithotripsy, especially in

hydrated conditions, due to the apparent low viscosity of the organic gel in globular morphologies.

The mechanical behaviour of sialoliths depends strongly on the fraction of organic matter, due to the apparent low viscosity and ductile nature of the organic gel. Sialoliths fracture surfaces are compatible with fracture behaviour of mixed characteristics, however, evidence was found for typical fracture behaviour of a brittle medium with ductile inclusions and ductile medium with rigid inclusions

Fragmentation induced by ultrasonic waves and pneumoballistic impacts target preferentially the mineralized material leaving the organic matter largely unaffected, whereas shock waves promote dissolution and leaching of the organic fraction. Laser ablation destroys homogeneously the irradiated zones regardless of the mineralized/organic nature of the underlying ultrastructure; however, damage is less extensive than with mechanical methods. The present results suggest that mechanical methods are best suited for comminution of large sialoliths, whereas laser ablation can be useful for precise drilling/dusting of small sialoliths or fragments generated by other lithotripsy techniques.

Correlations between lithotripsy efficiency with sialolith dimensions and X-ray attenuation were previously identified in clinical studies [35]. In this sense, the characterization method proposed in this work (see Chapter 4) could be implemented in a pre-therapeutic context to improve the *in situ* characterization of sialoliths in a multimodal therapeutic approach.

5.4. References

1. Zhong P, *et al.*, Characterization of fracture toughness of renal calculi using a microindentation technique, *J Mater Sci Lett*, 12:1460-1462, 1993
2. Heimbach D, *et al.*, Acoustic and mechanical properties of artificial stones in comparison to natural kidney stones, *J Urol*, 164:537-544, 2000
3. Fong H, *et al.*, Nano-mechanical properties profiles across dentin–enamel junction of human incisor teeth, *Mater Sci Eng C*, 7:119-128, 1999
4. Habelitz S, *et al.*, Mechanical properties of human dental enamel on the nanometre scale, *Arch Oral Biol*, 46:173-183, 2001
5. Park S, *et al.*, Mechanical properties of human enamel as a function of age and location in the tooth, *J Mater Sci Mater Med*, 19:2317-2324, 2008
6. Gross KA, Bhadang KA, Sintered hydroxyfluorapatites. Part III: sintering and resultant mechanical properties of sintered blends of hydroxyapatite and fluorapatite, *Biomater*, 25:1395-1405, 2004
7. Gross KA, Rodriguez-Lorenzo LM, Sintered hydroxyfluorapatites. Part II: mechanical properties of solid solutions determined by microindentation, *Biomater*, 25:1385-1394, 2004
8. He LH, Swain MV, Influence of environment on the mechanical behaviour of mature human enamel, *Biomater*, 28:4512-4520, 2007
9. Argon AS, *et al.*, Cavity formation from inclusions in ductile fracture, *Metall Trans A*, 6:825-837, 1975
10. Kim HS, *et al.*, On the rule of mixtures for predicting the mechanical properties of composites with homogeneously distributed soft and hard particles, *J Mater Process Technol*, 112:109-113, 2001
11. White SN, *et al.*, Biological organization of hydroxyapatite crystallites into a fibrous continuum toughens and controls anisotropy in human enamel, *J Dent Res*, 80:321-326, 2001

12. Harrill JA, *et al.*, Structure and composition of salivary calculi, *Laryngoscope*, 69:481-492, 1959
13. Pittomvils G, *et al.*, The influence of internal stone structure upon the fracture behaviour of urinary calculi, *Ultrasound Med Biol*, 20:803-810, 1994
14. Cohen NP, Whitfield HN, Mechanical testing of urinary calculi, *World J Urol*, 11:13-18, 1993
15. Ahmed K, *et al.*, Cystine calculi: challenging group of stones, *Postgrad Med J*, 82:799-801, 2006
16. Prien EL, Prien EL, Jr., Composition and structure of urinary stone, *Am J Med*, 45:654-672, 1968
17. Chuong CJ, *et al.*, Acoustic and mechanical properties of renal calculi: implications in shock wave lithotripsy, *J Endourol*, 7:437-444, 1993
18. Nolasco P, *et al.*, Structural characterization of salivary calculi In *2012 IEEE 2nd Portuguese Meeting in Bioengineering (ENBENG)*, Coimbra, Portugal, IEEE, pp. 1-5, 2012
19. Jayasree RS, *et al.*, Spectroscopic and thermal analysis of a submandibular sialolith of Wharton's duct resected using Nd:YAG laser, *Lasers Med Sci*, 23:125-131, 2008
20. Toughening Mechanisms in Composite Materials, (ed. 1st), Woodhead Publishing, 2015
21. Zhong P, *et al.*, Microhardness measurements of renal calculi: regional differences and effects of microstructure, *J Biomed Mater Res*, 26:1117-1130, 1992
22. Gullerud AS, *et al.*, Simulation of ductile crack growth using computational cells: numerical aspects, *Eng Fract Mech*, 66:65-92, 2000
23. Swamy KM, *et al.*, Application of Ultrasound in Leaching, *Miner Process Extr Metall Rev*, 14:179-192, 1995
24. Escudier MP, *et al.*, Extracorporeal shockwave lithotripsy in the management of salivary calculi, *Br J Surg*, 90:482-485, 2003

25. Capaccio P, *et al.*, Extracorporeal lithotripsy for salivary calculi: a long-term clinical experience, *Laryngoscope*, 114:1069-1073, 2004
26. Zenk J, *et al.*, Extracorporeal shock wave lithotripsy of submandibular stones: evaluation after 10 years, *Ann Otol Rhinol Laryngol*, 113:378-383, 2004
27. Schmitz S, *et al.*, Long-term evaluation of extracorporeal shock wave lithotripsy in the treatment of salivary stones, *J Laryngol Otol*, 122:65-71, 2008
28. Abe T, *et al.*, Outcomes of shockwave lithotripsy for upper urinary-tract stones: a large-scale study at a single institution, *J Endourol*, 19:768-773, 2005
29. Lokhandwalla M, Sturtevant B, Fracture mechanics model of stone comminution in ESWL and implications for tissue damage, *Phys Med Biol*, 45:1923-1940, 2000
30. Cernavin I, A comparison of the effects of Nd:YAG and Ho:YAG laser irradiation on dentine and enamel, *Aust Dent J*, 40:79-84, 1995
31. Ganesamoni R, *et al.*, Prospective randomized controlled trial comparing laser lithotripsy with pneumatic lithotripsy in miniperc for renal calculi, *J Endourol*, 27:1444-1449, 2013
32. Capaccio P, *et al.*, Modern management of obstructive salivary diseases, *Acta Otorhinolaryngol Ital*, 27:161-172, 2007
33. Phillips J, Withrow K, Outcomes of Holmium Laser-Assisted Lithotripsy with Sialendoscopy in Treatment of Sialolithiasis, *Otolaryngol Head Neck Surg*, 150:962-967, 2014
34. McClain PD, *et al.*, Optimizing shock wave lithotripsy: a comprehensive review, *Rev Urol*, 15:49-60, 2013
35. Escudier MP, *et al.*, Factors influencing the outcome of extracorporeal shock wave lithotripsy in the management of salivary calculi, *Laryngoscope*, 120:1545-1549, 2010

Chapter 6. Concluding remarks and future work

The structure, composition and mechanical behaviour of sialoliths have been characterized in detail to better understand the response of sialoliths to lithotripsy methods.

Typically, sialoliths present one major core, with either higher or lower mineralization than the surrounding regions. Specimens with multiple or without any core are not prevalent but their existence demonstrates diversity in the nucleation processes. Four different growth patterns have been identified in relation to the calculi organization and mineralization degree. Nonetheless, heavy mineralization around the nucleation region (with average maximum at $R = 1.2$ mm) and low variation in local mineralization at later stages, suggest common growth mechanisms.

At fine scales, sialoliths showed alternating mineralized/organic bands and soft organic globules dispersed in a mineralized hard matrix. The precipitation patterns observed in banded structures are compatible with a Liesegang–Ostwald phenomenon, whereas the globular structures are compatible with a surface tension effect.

Sialoliths can be considered biocomposites with a major organic fraction (~65 vol. %), having density of ~ 1.2 g/cm³. The mineral fraction presents a density of ~ 2.8 g/cm³, and is composed of a mixture of finely dispersed mineral crystals of magnesium-substituted, calcium-deficient, type-B carbonated hydroxyapatite (89 vol. %) and sub-stoichiometric Mg-whitlockite (11 vol. %).

The mineral density and distribution of organic matter in sialoliths was inferred from μ CT data and it has been proposed that X-ray computed tomography can be used to evaluate the degree of mineralization of sialoliths in a pre-therapeutic context for larger specimens.

The mechanical behaviour of sialoliths depends strongly on the fraction of organic matter, due to the apparent low viscosity and ductile nature of the organic gel. Fragmentation induced by ultrasonic waves and pneumoballistic impacts target preferentially the mineralized material leaving the organic matter largely unaffected, whereas shock waves

promote dissolution of the organic fraction and flow of the unsupported mineralized material. The flow patterns observed suggests that fluid mechanics is required for a correct evaluation of shock wave lithotripsy efficiency. Laser ablation destroys homogeneously the irradiated zones regardless of the mineralized/organic nature of the underlying ultrastructure but causes less extensive damage. Therefore, mechanical methods are best suited for comminution of large sialoliths, whereas laser ablation can be useful for precise drilling/dusting of small sialoliths or fragments generated by other lithotripsy techniques.

Future work can be expected to focus on establishing quantitative correlations between the calculi structure/composition with the calculi mechanical and rheological behaviour, to identify the key features behind the damage extension for each of the mechanical lithotripsy methods. Moreover, the detailed evaluation of the rheological behaviour of the mineralized and organic gels, by atomic force microscopy and fractal analysis, offers a deeper insight into the mechanisms governing the external shock wave lithotripsy damage.

The comprehensive information gathered by advanced characterization techniques can then be employed to model the fracture behaviour and determine specimen-tailored operational lithotripsy parameters that would increase the efficiency of sialolith comminution.